Impact of solid-liquid interfacial thermodynamics on the phase change memory RESET process

Matthew J Lewis

A dissertation submitted in partial fulfillment
of the requirements for the degree of

Doctor of Philosophy

University of Washington

2024

Reading Committee:
Lucien Brush, Chair
Anant Anantram
Guozhong Cao
Alberto Aliseda

Program authorized to offer degree:
Materials Science and Engineering

University of Washington

Abstract

Impact of solid-liquid interfacial thermodynamics on the phase change memory RESET process

Matthew J Lewis

Chair of the Supervisory Committee:

Lucien Brush

Department of Materials Science and Engineering

A model of the RESET melting process in conventional phase-change memory (PCM) devices is constructed in which the Gibbs-Thomson effect, representing local equilibrium at the solid-liquid interface, is included as an interfacial condition for the electro-thermal model of the PCM device. A comparison is made between the Gibbs-Thomson model and a commonly used model in which the interfacial temperature is fixed at the bulk melting temperature of the PCM material. The model is applied to conventional PCM designs in which a dome-shaped liquid/amorphous region is formed. Two families of solutions are computed representing steady state liquid regions, distinguished by their thermodynamic aspects. There is a family of solutions representing a liquid nucleation process, and a family of larger steady-state liquid solutions representing the limit of the melting process. A linear stability analysis is performed on the steady states, showing that the nucleus state is the threshold for further growth of the liquid phase which proceeds towards the melting limit state, which is the final stable state in the system. A comparison with a spherical symmetric model shows that in the isothermal limit the system is identical with the case of classical nucleation theory. The melting limits enable calculation of minima in voltage and corresponding current required for the RESET process. In this PCM configuration, the Gibbs-

Thomson effect constrains the equilibrium solid-liquid interface temperature to remain above the bulk melting temperature during melting. The magnitude of this temperature difference increases with decreasing device size scale, thus requiring an increase in the required voltage and current needed for RESET compared to the case in which the interface temperature is approximated by the bulk melting temperature. This increase becomes substantial for active device dimensions in the $<$20nm range. The impact of this phenomena on PCM device design is discussed, emphasizing the increased motivation to explore alternative designs that avoid or reverse the cost penalty due to solid-liquid interfacial thermodynamics. By reducing the required RESET power, such design decisions have the potential to improve the performance of PCM for a multitude of applications, including storage class memory, neuromorphic computing, and in-memory computing for machine learning applications.

Contents

List of Figures

Acknowledgments

First, I would like to acknowledge and thank my research advisor Professor Lucien Brush. Professor Brush has a particular way of being constructive in his advice, critical when necessary but always seeing the positive side of things in situations and research opportunities. His optimism

has been a useful counterbalance to my somewhat pessimistic tendencies. He has also been an extremely kind individual at a personal level, being very generous with his time over many years. The fact that he supported me through multiple stops and starts was indispensable for me being able to complete this Ph.D..

I would also like to thank my other committee members, Professors Guozhong Cao, Alberto Aliseda, and Anant Anantram, for their valuable feedback and support. I would like to thank Professor Anantram specifically, for giving me helpful background knowledge and advice on phase change memory early on in my research process.

Finally, I would like to thank my family. My parents, grandparents (some of whom are now deceased), and siblings have done so much to support and encourage me throughout the years of working on my Ph.D., even giving me feedback on how to make my dissertation and presentation slides more comprehensible.

Chapter 1

Introduction

1.1 Introduction to phase change memory

Phase change memory (PCM) is a form of computer memory in which information is stored by switching a region of electrically conductive material between different phases, usually a higher-conductivity crystalline phase and a lower-conductivity amorphous phase [1][2]. The most commonly used phase change material is $Ge_2Sb_2Te_5$ (GST), an example of a type of material known as a chalcogenide glass. Phases are switched by applying a voltage/current causing crystallization of the amorphous phase (during the SET process), or melt-quenching of the crystalline phase into amorphous phase (during the RESET process). The phase is measured (read) via the conductivity (or resistivity) difference between the phases.

The reversible switching effect used in phase-change memory was first discovered by S. Ovshinsky of Energy Conversion Devices in 1968 [3]. During the next three decades progress on developing this phenomena into a viable commercial memory was relatively slow due to challenges related to degradation of memory cells and instability of operation [4]. However, as the technology improved, interest in PCM once again increased in the early 2000s, with multiple companies (Intel, Samsung, STMicroelectronics, SKHynix) investing in research [4]. This renewed interest in phase-change memory continues to this day due to its promising characteristics as a next-generation memory type. Two recent reviews [1][2] (Kim et. al. 2020, Fong et.al. 2017) describe how PCM is currently promising as a potential storage-class memory, a term referring to specific market segment for memory which has cost and performance trade-offs between that of other memory types DRAM and NAND (flash). NAND memory has the advantage of being non-volatile, i.e. the memory remains when the power is switched off, which is why it is used, for example, in flash drives. However, NAND is relatively slow compared to DRAM which is used for random access memory in computer applications. DRAM, however, is volatile meaning it is erased when the power is switched off, so it cannot be used for storage. Phase change memory has the potential to bridge the advantages of these two types of memory by being both non-volatile and thus usable for storage, while also having faster speeds than NAND, speeds closer to being competitive

with DRAM. As a storage class memory PCM could be positioned to be a faster but more expensive replacement for NAND or a more cost-effective and non-volatile replacement for DRAM [2]. In general, the effectiveness of PCM is a result of a combination of nonvolatility, long endurance, fast write and access times and low cost per unit of memory. PCM has also attracted interest in the field of neuromorphic computing hardware, in which individual neurons are implemented using PCM devices [5] [6]. Another emerging area of application for PCM is in-memory computing, [7] [8] in which computational operations are performed directly in the memory unit rather than the CPU, with potential uses in improving machine learning and deep learning, including reducing energy consumption.

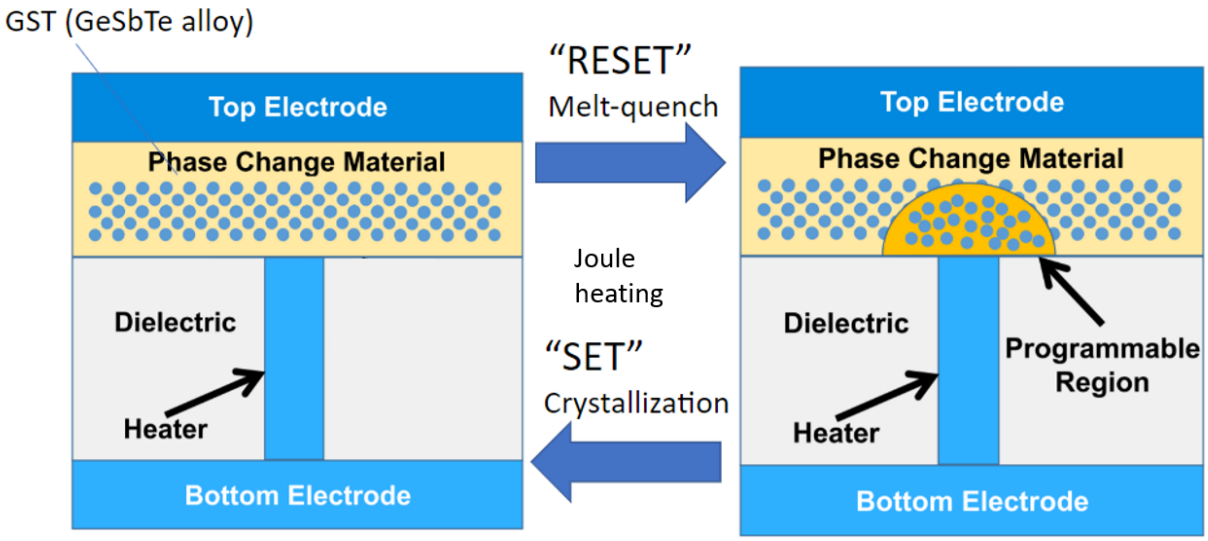

Figure 1.1: Schematic of a conventional "mushroom" PCM design in SET and RESET states, with arrows denoting the SET and RESET processes. Device visuals are taken from [2], ©2017 IEEE.

A schematic diagram of the two different states of a conventional phase change memory device, also called a "mushroom" or "thin film" design, [1][2] is shown in Figure 1.1. The device is structured as follows. The phase change material cell, most commonly GST, is positioned on top of a "heater" element electrode, and these two elements are sandwiched between two conventional electrodes. (Figure 1.1) This setup is then surrounded by a thermally and electrically insulating cladding material (dielectric). The heater element is typically made of a doped form of the material

used for the conventional electrodes, increasing its resistivity and therefore increasing the Joule heating occurring when current is run through it. The ”SET-RESET” cycle, i.e. the process of switching a memory bit within the device, is performed as follows: The device begins in the ”SET”

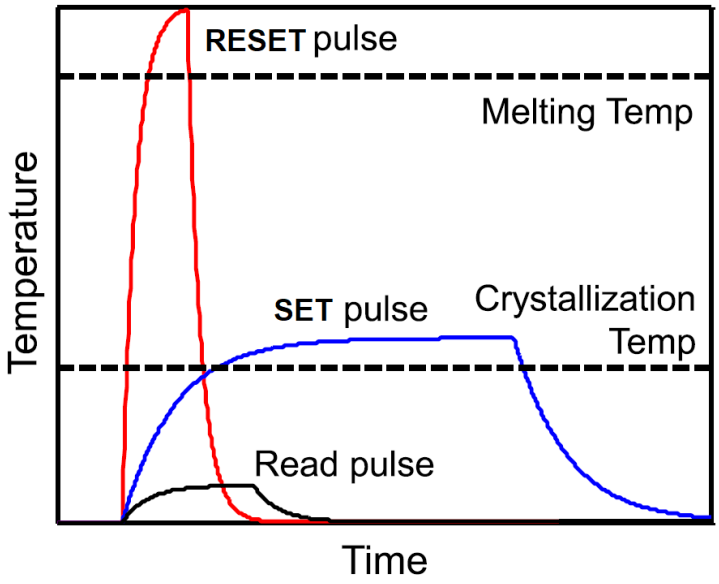

Figure 1.2: Schematic diagram of applied current pulses during the phase change memory SET-RESET cycle, taken from [2].

state in which the GST cell is entirely in a crystalline phase. A large current pulse (Figure 1.2) is then run through the device, concentrating heating at the junction between the heater element and the GST cell. With sufficient Joule heating, the GST melting temperature (873K) is exceeded and a dome-shaped region of the GST cell adjacent to the heater melts into the liquid phase. Then, the current pulse is switched off and the device rapidly cools down to room temperature as conductive heat flows out the electrodes. The cooling is rapid enough that the dome-shaped liquid region is quenched into an amorphous region of approximately the same size and shape as the melted liquid region. This amorphous GST phase has orders of magnitude higher electrical resistance than the crystalline phase, resulting in a difference in total device resistance which can be read as the memory bit. The bit is read by applying a much lower voltage and measuring the current difference due to the resistivity difference, and no phase change activity occurs as a result of the voltage being much lower. An important condition is that the amorphous region must completely cover the

heater-GST junction in order to ensure that all current paths must travel through the amorphous region, in order to obtain the desired jump in total device resistance. The step of applying the current pulse which forms the amorphous region is called the RESET step or RESET process. The state of the device with the amorphous region included is referred to as the RESET state. After the RESET step is applied, the next time the memory bit is switched the SET process is applied which returns the device to a pure crystalline state. During the SET process, a smaller current pulse is applied which is enough the heat the amorphous dome to the crystallization temperature of GST (around 400K). The amorphous dome recrystallizes completely, returning the device to a lower resistance SET state due to the lower resistivity of the crystalline GST phase.

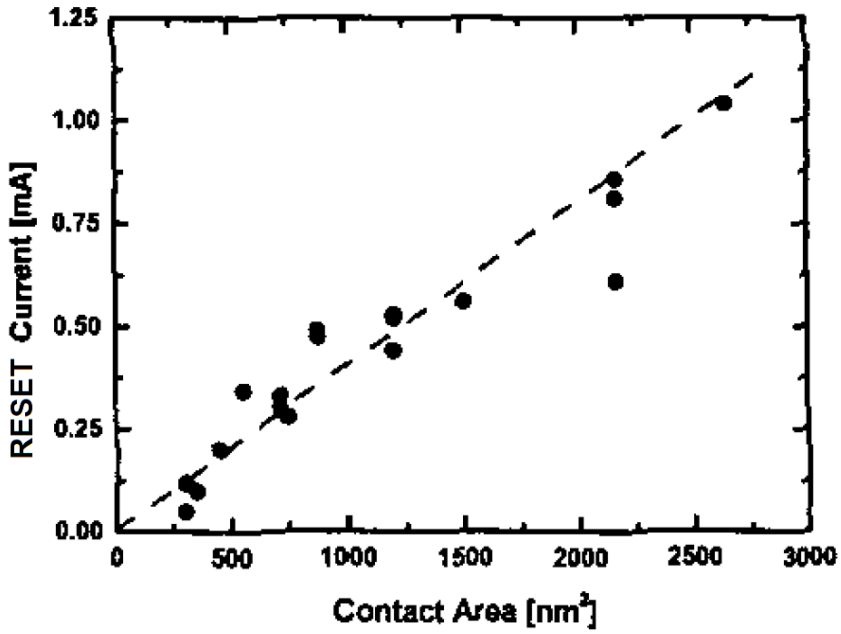

Figure 1.3: RESET current as a function of contact area (heater-GST junction) in conventional phase change memory devices, taken from [9].

One of the inherent challenges of PCM is that the high GST melting temperature must be exceeded every time the RESET step occurs, resulting in high required Joule heating and therefore high power costs for operation [2] [10]. However, offsetting this disadvantage is the fact that one of the most enticing aspects of PCM is its extreme scalability. A landmark study in 2003 (Pirovano et. al.) [9] showed a significant decrease in required RESET current as contact area (heater-

GST junction) is downscaled, due to the decreasing volume of the amorphized region resulting in less heating required for the melting process. Further research over the past two decades has

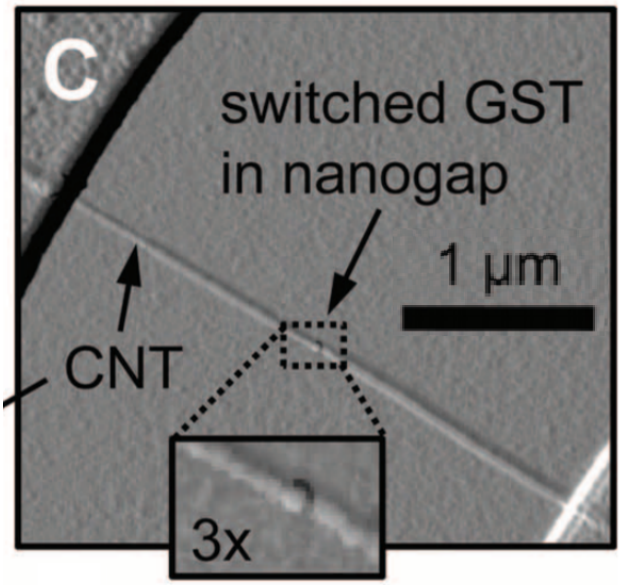

Figure 1.4: Partially crystallized SET state in a CNT-based PCM, from [11], ©2011 AAAS. The crystallized GST region between the CNT tips is shown in the 3x magnification. The surrounding material is amorphous GST.

shown that the active (phase-switching) region in PCM can be scaled to sizes of single nanometer dimensions [11][12], using carbon nanotubes (CNTs) as electrodes, where the active region is located between two carbon nanotube tips. (Figure 1.4) Given the success of the carbon nanotube-based experiments, it is natural to consider whether or not the same sub-10nm scaling can be achieved using conventional PCM designs, which are more manufacturable due to their geometry and material suitability. Simulations by Hayat et al.[13] of conventional PCM devices at sub-10nm scales indicate that with design improvement in thermal efficiency, usage at such small scales would be feasible, based on favorable scaling trends for RESET current/voltage. If this modeling is correct, downscaling would be greatly advantageous for reducing the power consumption of the devices.

1.2 Phase change mechanisms and interfacial effects during RESET process

However, the assumptions of favorable scaling for PCM devices at sub-10nm scales have used RESET models that are incomplete. In addition to heat transfer throughout the device, phase change mechanisms and material interfaces also play a role in the success of the device operation. For the RESET melting process, understanding of many of these details is lacking. Here we give an overview of the state of knowledge of various of these mechanisms. This overview is split into two sections, one about the state of knowledge of phase change mechanisms and interfacial effects that impact the initial appearance of liquid phase, followed by a section about solid-liquid interfacial thermodynamics as expressed in the Gibbs-Thomson condition. The latter of the two sections introduces the main focus of the research in this dissertation, but the first section is necessary as background to explain why models in this research are constructed the way they are, due to limitations in knowledge about the initial formation of the liquid phase.

1.2.1 Initial appearance of the liquid phase

Often, in general systems melting initiates via the mechanism of interfacial premelting, [14][15] in which the solid begins to exhibit a thin film of liquid at a heterogeneous or exposed interface at a temperature below the bulk melting temperature. However, it has not been previously investigated whether premelting is exhibited in the case of PCM devices. Interfacial premelting can be modeled by considering the total energetic contribution due to nonretarded Van der Waals forces. A derivation given in [15] leads to the result that the energetic favorability of premelting is determined by the sign of the three-part Hamaker constant corresponding to the total interaction of the three part system of the thin premelted liquid layer surrounded by whatever two media are surrounding it. For conventional PCM devices, it is assumed that the premelted liquid layer would be favored to form near the heater where the temperature is greatest, so this 3-part system would by the configuration of the solid GST, the heater electrode, and the liquid GST layer in between. (Figure 1.5)

This Hamaker constant can be estimated by Lifshitz theory, an approximation scheme in which computations of Van der Waals forces between particles incorporate the effects of macroscopic properties of the continuous media, in this case the dielectric properties.

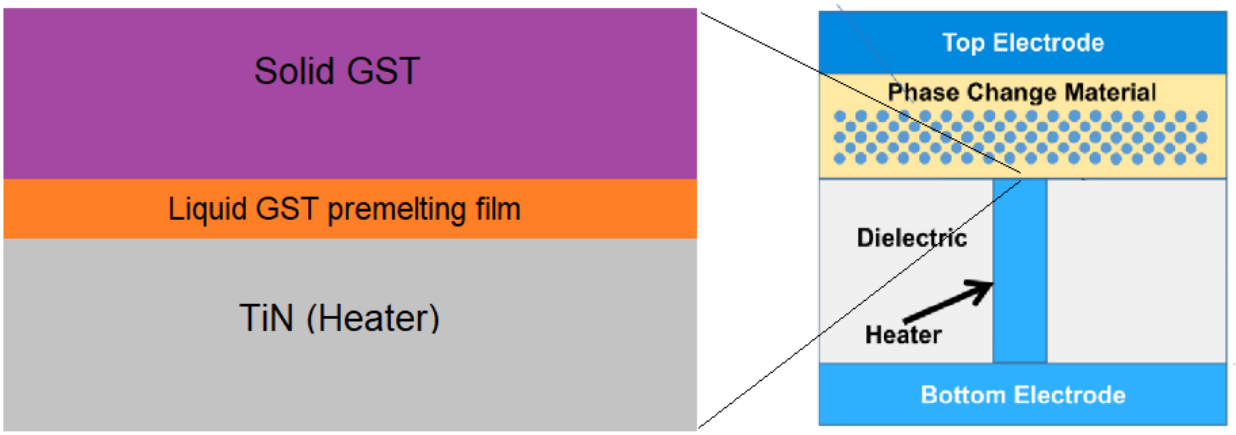

Figure 1.5: Zoomed-in section of a PCM device in which a thin premelted layer of liquid GST exists between the TiN heater element and solid GST regions. The three part Hamaker constant is computed based on this arrangement, and it is found that premelting is not favored for this system.

Lifshitz theory can be used [16] to estimate the Hamaker constant as depending on the dielectric functions of each of the three layers: 1. The TiN heater (TiN as the material for the heater is detailed in chapter 2) and 2. The solid GST region 3. The liquid GST layer:

$$A \approx \frac{3}{4} k_B T \left(\frac{\epsilon_1 - \epsilon_3}{\epsilon_1 + \epsilon_3}\right)\left(\frac{\epsilon_2 - \epsilon_3}{\epsilon_2 + \epsilon_3}\right) + \frac{3h}{4\pi} \int_{\nu_1}^{\infty} \left(\frac{\epsilon_1(i\nu) - \epsilon_3(i\nu)}{\epsilon_1(i\nu) + \epsilon_3(i\nu)}\right)\left(\frac{\epsilon_2(i\nu) - \epsilon_3(i\nu)}{\epsilon_2(i\nu) + \epsilon_3(i\nu)}\right) d\nu \tag{1.1}$$

Where k_B is Boltzmann's constant, T is the bulk melting temperature of GST, $873K$, h is Planck's constant, $\epsilon_i(i\nu)$ in the integral are the complex dielectric functions of layers i = 1,2,3 calculated at imaginary frequencies, and ϵ_i in the left term are the dielectric functions evaluated at $\nu = 0$.

Data for the complex dielectric functions of crystalline GST, amorphous GST (amorphous GST is use to approximate the liquid phase for which data is not available) and TiN have been measured [17] [18] in the form of real and imaginary dielectric functions $\epsilon(\nu) = \epsilon'(\nu) + i\epsilon''(\nu)$, each a function of frequency. The dielectric function at imaginary frequencies is computed by first fitting

the ϵ' and ϵ'' functions to a parametrized model, and then substituting an imaginary frequency, resulting in real functions that can be integrated in (1.1). Using a freely available Matlab script [19], dielectric functions $\epsilon'(\nu)$ and $\epsilon''(\nu)$ of GST and TiN were fitted to models of the form

$$\epsilon(\omega) = \epsilon_0 + \sum_p \frac{\Delta\varepsilon}{1 - 2i\omega\gamma_p} + \sum_p \frac{\Delta\varepsilon\omega_p^2}{-2i\omega\gamma_p - \omega^2} + \sum_p \frac{\Delta\varepsilon\omega_p^2}{\omega_p^2 - 2i\omega\gamma_p - \omega^2} + \sum_p \frac{\Delta\varepsilon(\omega_p^2 - i\omega\gamma_p')}{\omega_p^2 - 2i\omega\gamma_p - \omega^2} \tag{1.2}$$

where $\omega = 2\pi\nu$ and ϵ_0, $\Delta\varepsilon$, γ_p, and ω_p are fitting constants. From left ot right, the terms in the sums are known as Debye, Drude, Lorentz, and "modified Lorentz" terms. An appropriate number of each of these terms is chosen for each material in order to fit the data reasonably well to the degree that any remaining error does not make a difference to the integral for the Hamaker constant.

Before computing the Hamaker constant integral, $i\omega$ is plugged in in place of ω, resulting in $\epsilon(i\omega)$ which are real, positive, monotonically decreasing functions of the form

$$\epsilon(i\omega) = \epsilon_0 + \sum_p \frac{\Delta\varepsilon}{1 + 2\omega\gamma_p} + \sum_p \frac{\Delta\varepsilon\omega_p^2}{2\omega\gamma_p + \omega^2} + \sum_p \frac{\Delta\varepsilon\omega_p^2}{\omega_p^2 + 2\omega\gamma_p + \omega^2} + \sum_p \frac{\Delta\varepsilon(\omega_p^2 + \omega\gamma_p')}{\omega_p^2 + 2\omega\gamma_p + \omega^2} \tag{1.3}$$

and so the integral converges. (Also, a factor of 2π is included in the integral to convert from ω to ν). The result of numerically integrating (1.1) gives a value of $A = +1.5 \cdot 10^{-20} J$. The positive sign therefore implies that interfacial premelting is not energetically favored at this interface. (Both the first and second term in (1.1) are well on the positive side.)

Since interfacial premelting has been ruled out as a likely mechanism for the initial formation of the liquid phase, we may also look at a variety of other interior solid-state heterogeneities and defects to see how they may influence the initial appearance of the liquid in the melting process. One experimental study [20] found that in GST, near the melting temperature, vacancies arrange in planar configurations. Molecular dynamics simulations[20] show that during melting at 1300K the crystal first becomes disordered (liquid) around these planes. Further work would be needed to confirm if vacancies reduce or eliminate the barrier for initial formation of the liquid phase. An experimental study, in which GST vacancies are "filled" with gold atoms, shows a large increase

in the threshold voltage for melting/amorphization[21], although it is unclear what is the effect of the gold in this case. Another experimental study[22] of GST melting suggests that dislocations can cluster and initiate amorphization, although the interpretation of the result was not compared to a traditional thermodynamic model. Recent simulation research [23] has modeled barrier-free heterogeneous melting at grain boundaries which may be applicable to the PCM device provided that a small grain size is maintained over multiple switching cycles, but this is not certain especially for smaller scaled devices. The conclusion drawn from these studies is that the influence of pre-existing defects may lower but does not necessarily remove the energy barrier to the formation of the liquid, implying a nucleation and growth mechanism from metastable superheated solid may also be considered. In a comprehensive 2006 review of the superheating of solids by Mei and Lucite[24], many examples are provided of experiments in which metastable superheating occurs. Various metal nanoparticles coated with a different, higher-melting point metal have sustained metastable superheating on the order of 10-100K above the bulk melting temperature. This is notable because the GST region in a scaled-down PCM device is similar to a nanoparticle "coated" by a higher-melting point surrounding. Time-dependent discrete cellular PCM models [13] [2] [25] [26] [27] [28] [29] that include nucleation assign an ad-hoc probability for phase change to occur in each cell based on bulk parameters and classical nucleation theory. However, these models assume perfectly spherical, classical nuclei small enough to fit inside each model cell (a very small fraction of the total device size), which is not an appropriate assumption at small scales as shown in results below. Instead, nuclei would be large on the scale of the temperature variations in the range of several hundred degrees K.

In summary, the information presented in this section has shown that significant additional research would be required to understand the time-dependent initial formation of the liquid phase via the assistance of defects and/or a time-dependent nucleation process.

1.2.2 Solid-liquid interfacial thermodynamics

Another aspect of the RESET melting process which merits further investigation, and is the main focus of this dissertation, is the effect of solid-liquid surface energy in which the equilibrium melting point of any solid is shifted from its bulk value by an amount proportional to interface curvature and can be significant at very small scales. The effect is manifest in the Gibbs-Thomson condition:

$$T_{eq} = T_m(1 + \frac{\gamma}{L}H), \tag{1.4}$$

where T_{eq} is the equilibrium solid melting temperature, T_m is the bulk or planar interfacial melting temperature, L is the latent heat of fusion per unit volume of solid, H is the mean curvature of the solid-liquid interface and γ is the interfacial energy of the solid-liquid interface, assumed isotropic. The mean curvature is a signed quantity, defined in this research with positive value $H = +2/R$ for a spherical melt of radius R surrounded by solid, and a negative value $H = -2/R$ for a solid sphere of radius R surrounded by liquid. For conventional PCM designs, a liquid dome is formed during RESET and H is positive, implying $T_{eq} > T_m$. As devices are scaled down, the magnitude of H, and thus $T_{eq} - T_m$, increases, possibly impacting the device performance. Compared to the above description, some previous PCM models have included surface energy effects only in ad-hoc treatments of the nucleation process [13] [25] [26] [27] [28] [29], without also including the general condition (1.4) with interface curvature. Other RESET models have not included surface energy effects at all because they assume that the material automatically melts for $T > T_m$. [30] [31] [32][33] [34] [35] [36].

In this research a new numerical model for the formation of the liquid phase during the melt-quench RESET process in GST PCM devices is presented in which the solid-liquid interface temperature is equal to the Gibbs-Thomson temperature (1.4). A complete time-dependent RESET model which includes the defect and/or stochastic nucleation assisted initial formation of the liquid is not informative at this time, because of the many ambiguities in the mechanism of the initial formation of the liquid phase, as listed above. Therefore, in this research the melting system is

modeled as a deterministic, time-dependent, moving boundary problem in which liquid evolution takes place in a regime beyond the initial formation of the liquid phase. The numerical model allows for arbitrarily shaped (albeit axisymmetric) GST solid-liquid interfaces. In addition to basic coupled electrical and thermal field simulation, thermoelectric effects [37] and thermal boundary resistance (TBR) [38][39] have a substantial impact in PCM devices and are therefore included in this model.

In this work, *steady states* of the time-dependent model are computed which illuminate the dynamics of the melting system. From these steady states *minimum* required voltage and corresponding current values in the RESET process are derived. Computation of these data across a wide range of scales illustrates for the first time the impact of solid-liquid interfacial thermodynamics on device efficiency in conventional PCM designs as a function of device size. A scaling law for this impact is derived illustrating how a conventional design may have deleterious effects on the device efficiency.

The remainder of this dissertation is structured as follows: In Chapter 2 the deterministic time-dependent RESET melting model for a conventional PCM device is presented and the methods for computing steady states from this model are described. The results of the steady state computations are introduced and general descriptions of the states are given. Models with and without the Gibbs-Thomson effect are compared and methods for computing the required voltage for RESET are shown. It is shown that these results depend heavily on assumptions made about the time-dependent properties of the steady states. A comparison is made with classical nucleation theory, showing how that theory is insufficient to model or understand the phenomenon in PCM devices. In order to have a more thorough understanding of the time-dependent properties of steady states and their significance, in Chapter 3 a linear stability analysis is performed on the steady states. It is shown that the time-dependent properties of the states justify the descriptions of the states given in Chapter 2. A comparison is also made with a spherically symmetric model device to further show the connection between classical nucleation theory and the steady states given here. An analysis of RESET melting in a cylindrically symmetric PCM model device is also presented for further com-

parison. With the time-dependent aspects of the steady states more fully understood, in Chapter 4, information about PCM device performance is computed as a function of device size/scale. These results show the influence of solid-liquid interfacial thermodynamics on the RESET process in terms of impact on device performance. Implications for device design are discussed, emphasizing the increased motivation to explore alternative designs that avoid or reverse the cost penalty due to solid-liquid interfacial thermodynamics. In Chapter 5 a conclusion is given summarizing all of the results from chapters 2-4.

Chapter 2

RESET melting models and steady states

2.1 Methods for computing steady states of the RESET process

As stated in the Introduction, in this research information about the impact of solid-liquid interfacial thermodynamics on the phase change memory RESET process is gleaned from computing steady states of a model which includes the Gibbs-Thomson effect. In this chapter, it is shown how steady states are computed in a model with the Gibbs-Thomson effect as well as model without it for comparison. Here it is also shown what information can be gathered from the steady state computations, and what limitations exist in analyzing the steady states alone without further time-dependent analysis.

2.1.1 The models

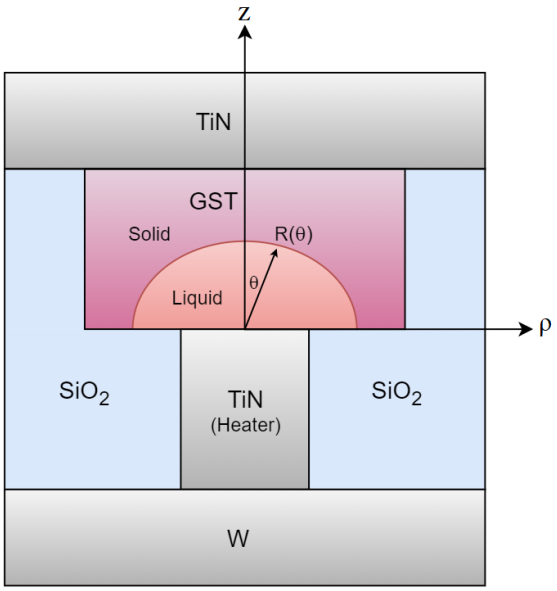

Figure 2.1: Proportionately accurate cross-sectional diagram of the axially symmetric 3D device geometry used for numerical simulations in this research. Also depicted are cylindrical coordinate ρ and z axes. The z axis is the axis of rotation.

Numerical simulations of full phase change memory devices presented in this research use a PCM device design emulating the one used in the work of Hayat et al.[13]. A cross-section of the device is shown in Figure (2.1). The device is axially symmetric about a vertical axis and is encased within a cylindrical volume. Denoting the radius of the GST cell by CR, the device

domains have the following proportions: total radius = 1.5 · CR, total height = 3.0 · CR, heater radius = 0.4 · CR, heater height = CR, GST cell height = CR, height of top and bottom electrodes = 0.5 · CR. The remainder of the cylindrical volume is SiO_2. It is noted that the axisymmetric shape is not necessarily realistic for mass manufactured PCM devices, but greatly simplifies the modeling process while offering a good approximation of non-axisymmetric conventional PCM device designs.

Using spherical coordinates centered about the GST-heater interface, at any fixed time t the liquid region shape is defined by a function $r = R(\theta, t)$ in the range $0 \leq \theta \leq \pi/2$ as shown in Figure (2.1), where r and θ are radial distance and polar angle, respectively. The solid-liquid interface is constructed by fully rotating $R(\theta, t)$ about the longitudinal axis of the cylinder. The mean curvature of the crystal-liquid interface is $H = \nabla \cdot \hat{n}$, where $\hat{n}$ is the unit normal vector to the interface. The unit normal vector is computed using the gradient of a contour function corresponding to the solid-liquid interface:

$$F \equiv r - R(\theta) \tag{2.1}$$

$$\nabla F = \hat{e}_r - \frac{1}{r} R_\theta \hat{e}_\theta \tag{2.2}$$

$$|\nabla F| = \sqrt{1 + \frac{1}{r^2} R_\theta^2} \tag{2.3}$$

$$\hat{n} = \frac{\nabla F}{|\nabla F|} \tag{2.4}$$

$$= \left[\hat{e}_r - \left(\frac{R_\theta}{r} \right) \hat{e}_\theta \right] \left(1 + (R_\theta)^2/(r)^2\right)^{-1/2} \tag{2.5}$$

where $\hat{e}_r$ and $\hat{e}_\theta$ are orthogonal unit vectors for the r and θ spherical coordinates and subscripts refer to partial derivatives. $H = \nabla \cdot \hat{n}$ is computed using the formula for the divergence in spherical coordinates:

$$H = \nabla \cdot \hat{n} = \frac{1}{r^2} \frac{\partial}{\partial r} (r^2 \hat{n}_r) + \frac{1}{r \sin(\theta)} \frac{\partial}{\partial \theta} (\sin(\theta) \hat{n}_\theta) \tag{2.6}$$

Evaluation at $r = R(\theta, t)$ gives $H(\theta, t) = (R^2 + R_\theta^2)^{-1/2}(2 - \frac{R_\theta}{R}\cot(\theta)) + (-RR_{\theta\theta} + R_\theta^2)(R^2 + R_\theta^2)^{-3/2}$. The local normal growth speed is given by $v_n = R_t/(1+R_\theta^2/R^2)^{1/2}$. Boundary conditions for the solid-liquid interface shape function are as follows: At $\theta = 0$, $R_\theta = 0$, meaning there is no cusp (which would be a point with infinite curvature). At $\theta = \pi/2$ (GST cell-bottom face contact location), R_θ is also set to zero, meaning that the solid-wall and liquid-wall interfacial energies have been set equal resulting in a 90 degree contact angle.

Electrical potential $\phi_i(\vec{x}, t)$ and temperature $T_i(\vec{x}, t)$ in the $'i'$th material/phase obey coupled charge and energy balance equations which include thermoelectric effects and Joule heating. Charge conservation gives

$$\nabla \cdot (\sigma_i(-\nabla\phi_i - S_i\nabla T_i)) = 0 \tag{2.7}$$

where σ_i and S_i are the spatially varying electrical conductivity and Seebeck coefficients of the $'i'$th material and the electric current density is $\vec{J_i} = \sigma_i(-\nabla\phi_i - S_i\nabla T_i)$. Simulating a constant voltage pulse, $\phi = V$ at the top device face and 0 at the bottom face. The device walls are insulating, $\vec{J_i} \cdot \hat{n} = 0$, with $\hat{n}$ being the outward pointing unit normal vector.

The temperature obeys the heat equation with Joule and Thomson heating:

$$\nabla \cdot (k_i\nabla T_i) + \frac{\vec{J_i} \cdot \vec{J_i}}{\sigma_i} = \rho_i c_{p,i}\frac{\partial T_i}{\partial t} - T_i\vec{J_i} \cdot \nabla S_i \tag{2.8}$$

k_i is the thermal conductivity, ρ_i is the density, $c_{p,i}$ is the specific heat capacity. At all the device outer boundaries T = 273K, simulating near-room temperature conditions maintained during device operation. Internal interfaces between materials/phases i and j obey charge and energy conservation, with Peltier heat $T\vec{J} \cdot \hat{n}(S_i - S_j)$ included, $\hat{n}$ pointing from i to j. In addition to obeying (1.4), the mobile solid liquid interface evolves heat Lv_n. At interfaces which have thermal boundary resistance (TBR), $(k_i\nabla T_i) \cdot \hat{n} = (T_j - T_i)/\alpha$, where α is the TBR coefficient. At interfaces $T_{avg} = \frac{1}{2}(T_i + T_j)$ is used for Peltier heat and α temperature dependence (detailed below) calculations.

The model described above is defined as the Gibbs-Thomson (GT) model. Throughout this

research the GT model is compared to a model with the solid-liquid interface position coinciding with the bulk melting $T = T_m$ isotherm, rather than the GT condition. Additionally, with the interface given by the T_m isotherm, there is no contact angle condition at the lower GST interface. This model is denoted as the bulk melting (BM) model.

The impact of TBR increases in importance with downscaling, shown in past literature [40] (as well as in results below), so it is useful to isolate its impact when comparing with the GT and BM models. Therefore we present two variations of the models, one with $\alpha = 0$ for all interfaces, denoted "TBR-absent", and one with non-zero α values denoted "TBR-present".

2.1.2 Numerical procedures and material properties

In this chapter steady state solutions are sought satisfying $\partial T/\partial t = 0$ and $R_t = 0$ everywhere. (Subscripts have been omitted.) The model is vertically axisymmetric, so ϕ, T, and R are solved in the right half of the cross-section shown in Figure 2.1. The shape function $R(\theta)$ is discretized evenly over $0 \leq \theta \leq \pi/2$ with $n = 30$ points, defining the GST solid and liquid regions. Second order differencing in θ is used to compute H at each node.

In cylindrical coordinates (ρ, z, Φ), steady state solutions $\phi(\rho, z)$ and $T(\rho, z)$ of (2.7) and (3.21) are found using the software package FiPy[41], which implements a finite volume method (FVM). The 2D domain is discretized into a grid of $3n \times 6n$ square cells (n being the number of discretized points of $R(\theta)$). TBR is implemented by decreasing volume thermal conductivity in a region of a thickness of 2 nodes at the boundary by an amount causing the equivalent thermal resistance. Peltier heat at the top and bottom GST-TiN interfaces is applied through volume heating in the thin region causing an equivalent amount of boundary heating. The values of k and σ in liquid GST, TiN, TiN (doped, heater), W and SiO_2, are 5.0, 19, 17, 175, and 1.4 W/(m·K),[13] and 2.5×10^5, [42] 5.0×10^5, 5.0×10^4, 1.8×10^6,[43] and 0.01 $\Omega^{-1}\text{m}^{-1}$, respectively. (The Wiedmann-Franz law for metals [43] is used to estimate liquid GST k.) Crystalline GST is assumed to be in the fcc crystal structure as this phase forms during SET [44]. Temperature dependence of fcc electrical conductivity [42] is fit as $\sigma = \sigma_0 e^{-T_0/T}$, σ_0 = 1.81·10^6 $\Omega^{-1}\text{m}^{-1}$, T_0 = 2.77 ·10^3K, using

$\sigma = \sigma_0 e^{-T_0/T_m}$ for $T > T_m$. Fitting data [45] for variation of fcc GST thermal conductivity, k = 0.45 W/(m·K) for T $<$ 403K, k = 0.95 W/(m·K) for T $>$ 583K, and varies linearly between. In the multiphase GST region, σ and k are interpolated smoothly through the interfacial region across a length of 1-2 cells.

Values of the TBR coefficient α have been measured for the GST-TiN interfaces for temperatures 298-598K [46] and the GST-SiO_2 interface for 463-533K [47] (fcc phase). No measurements yet exist for the *liquid*-GST TiN α value. The study [46] suggests a $1/T$ temperature dependence model to extrapolate to higher temperatures, which we use here. Using GST-TiN data from [46] and the GST-SiO2 data from [47], the resulting temperature dependence gives for GST-TiN α = 36.6 $m^2 \cdot K$ / GW at T = 300K, α = 12.6 $m^2 \cdot K$ / GW at T_m = 873K and for GST-SiO_2 α = 16.4 $m^2 \cdot K$ / GW at T = 300K, α = 5.6 $m^2 \cdot K$ / GW at T_m = 873K. Solid-GST-TiN values are used for the liquid-GST-TiN case.

Seebeck coefficient data for GST and TiN in the range 300K $<$ T $<$ 1000K are taken from [37], and for W in the range 300K $<$ T $<$ 550K taken from [48]. Data is extrapolated outside of these ranges using endpoint values. Current direction is chosen to produce positive Peltier heating at the GST-TiN heater boundary and negative Peltier (cooling) heating at the upper GST-TiN boundary.

The latent heat L is 4.19 $\times$ 10^8 J/m^3[49]. Obtaining a precise experimental measurement of the solid-liquid interfacial energy γ is difficult, however theoretical estimates may be used. Previous ab initio simulations of nucleation during the SET process[50] calculated the GeTe solid-amorphous/liquid interfacial energy, the main component of the GST alloy (GeTe-Sb_2Te_3), over the temperature range 300-800K. Extrapolation to the melting temperature gives γ = 25 meV/A^2 = 0.4 J/m^2, the value used here. A study by Orava and Greer[51] provides a temperature-dependent theoretical formula for γ based on bulk properties of GST. For the temperature ranges under consideration here, their γ value is approximately 1.5-2 times smaller than the value used here. Scaling analysis later in Chapter 4 shows how variance in γ factors into the interpretation of the results.

An iterative method is used to find the steady state shapes $R(\theta)$, using the nonlinear solver function scipy.root() from the SciPy python package which implements a modified Powell's method.

Each iteration, $R(\theta)$ is specified, then coupled equations (2.7) and (3.21) are solved to find ϕ and T. A residual (error) vector is computed as the difference between the solid-liquid interface temperature and the GT or BM equilibrium temperature. The solid-liquid interfacial temperature is computed for each of the $n = 30$ solid-liquid interface discretized nodes by linearly interpolating the spatial temperature function, sampling the temperature values in each of the four adjacent discretized volume cells. Iterations are repeated until $R(\theta)$ is modified such that the magnitude of the residual is below a tolerance of $0.001K$.

Overall device current I is computed by integrating current density $\vec{J}$ numerically over the bottom face of the device $I = \int \vec{J} \cdot \hat{n} dA = \int \sigma(\nabla\phi + S\nabla T) \cdot \hat{n} dA$, where $\hat{n}$ is the outward-pointing unit normal vector. The quenched (RESET state) device resistance Σ is calculated as follows. Ohmic, near-room temperature conditions are assumed. Crystalline and amorphous electrical conductivities are set to their room temperature values 177 and 0.830 $\Omega^{-1}\text{m}^{-1}$[42]. Σ is calculated by applying 1.0 V, solving (2.7) (with $\nabla T = 0$) for $\phi(\rho, z)$, computing device current I_r then dividing 1.0 V by I_r.

2.2 Results of steady state computations

2.2.1 Steady state solutions: Melting limit and nucleus

In Figure (2.2), steady state solutions for a device with a GST cell radius = 10 nm and subject to an applied voltage of 1.10V are shown for the BM model (left hand graph) and the GT model (center and right hand graphs) in the TBR-absent case.

The labels ”melting limit” and ”nucleus” in Figure (2.2) provide physical interpretation of the states. These physical interpretations are elaborated upon much more thoroughly in Chapter 3. For now, the following descriptions are given: The melting limit contains the maximum-sized liquid region reachable under the given voltage, and is the state approached as the voltage is held for an arbitrarily long time. This example shows that for a given voltage the size of melting limit liquid pool is smaller in the GT model than in the BM model, as the higher equilibrium temperature

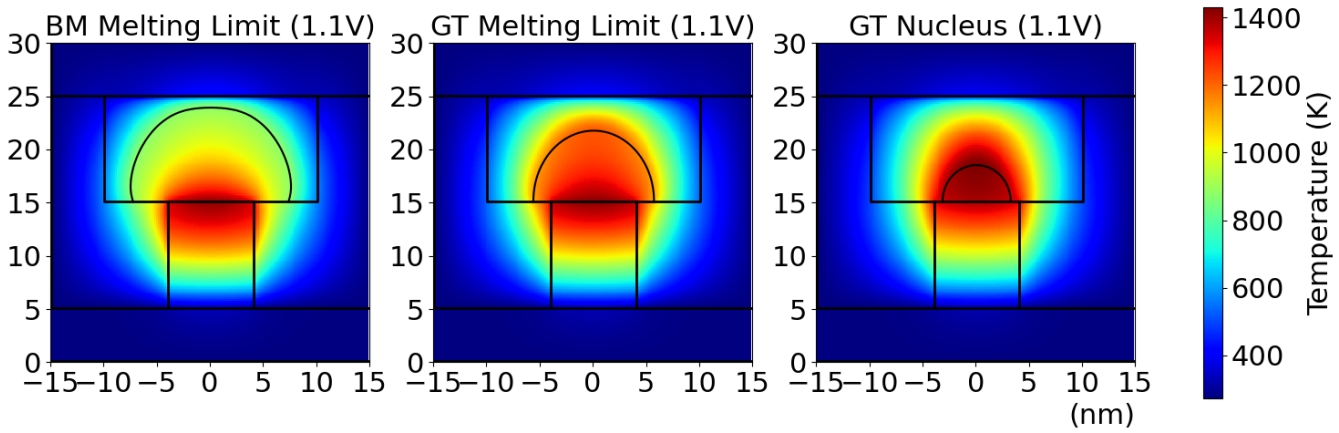

Figure 2.2: Steady states computed by the bulk model (BM) and the Gibbs-Thomson model (GT) for an applied voltage of 1.10V and a cell radius of 10nm for the TBR-absent case. Black lines are boundaries between materials/phase identified in Figure 2.1. The curved line is the GST solid-liquid interface with liquid GST inside the dome and solid GST surrounding. x and y axes denote ρ and z coordinates with origin at the center of the bottom device face.

of the GT effect is satisfied by an interface closer to the hotter center. The GT model also gives rise to a second steady state with a smaller liquid region, defined as the nucleus. An approximate thermodynamic description of the nucleus solution is that it contains the minimum volume that must be achieved for the local driving force of superheating to overcome the interfacial energy cost at each point on the surface and sustain a stable and growing liquid pool. Once the liquid region grows beyond the nucleus solution, melting is favored to continue towards the melting limit, at which point temperature is low enough (due to distance away from center) that heat flux balances cause a steady state and further growth is not favored. The liquid region sizes between the nucleus and melting limit therefore define a space for which melting is favored.

2.2.2 RESET behavior as a function of voltage

For a conventional PCM device, the goal of the RESET process is for the amorphous region to completely cover the heater electrode such that after the RESET current pulse is over and quenching due to cooling has occurred, the total device resistance increases by multiple orders of magnitude due to all the current paths having to travel through the high-resistance amorphous dome.

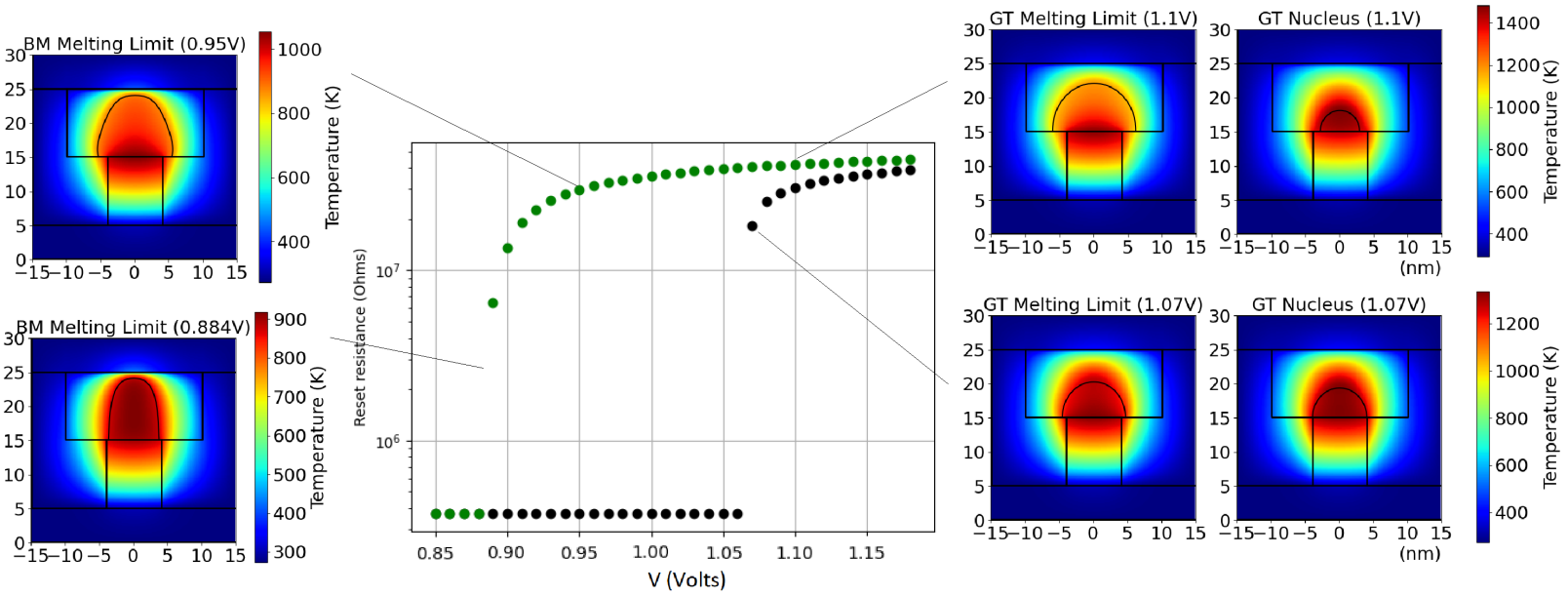

Figure 2.3: (Center) RESET state resistance of the quenched device at the melting limit plotted logarithmically as a function of applied voltage for a 10 nm cell radius. The bulk model is in green and the Gibbs-Thomson model is in black. Examples of steady states computed by the GT model at 1.1V and 1.07V and the bulk model at 0.95V and 0.884V are also shown.

If we assume that the melting limit is the final state of the RESET process as described above, then the quenched resistance of the device with an amorphous dome identical to the melting limit liquid dome is of interest for device performance considerations. The RESET (quenched) resistance of melting limit liquid shapes over the range 0.85V - 1.18V for a 10 nm GST cell radius in the TBR-absent case are shown in Figure 2.3. In both the BM and GT models, melting limit size increases with voltage resulting in greater amorphized volume and greater RESET resistance as voltage increases. In the BM model, at $\sim$0.887V the melting limit liquid width just begins to completely cover the heater, forcing all current paths in the RESET state to cross through the high-resistance amorphous region and causing a sharp transition of approximately two orders of magnitude change in resistance. In the GT model, the voltage at which the BM model's melting limit RESET resistance values are achieved is $\sim$0.18V greater than the corresponding voltage in the BM model at the transition values and decreases to $\sim$0.13V at larger voltages. This difference is due to the smaller melting limit liquid pool in the GT model.

In the GT model, no steady state solutions (melting limit or nucleus) are found below $\sim$1.0695V, where the melting limit still has a substantial sized liquid pool. This voltage, referred to as the cutoff voltage, appears to be primarily defined by solid-liquid interfacial thermodynamics. This is evidenced by the fact that the cutoff voltage coincides with the GT *nucleus* liquid region matching the exact size of the melting limit liquid region. An example of similar-sized melting limit and nucleus states for a voltage of 1.07V, just above $\sim$1.0695V, is shown in Figure 2.3. A thermodynamic description of this situation would be as follows. The nucleus liquid pool size increases with decreasing voltage due to superheating decreasing, leading to greater liquid volume needed to overcome the interfacial energy cost. Since the melting limit and nucleus approach each other in size at the cutoff, the above-described melting-favored space between the nucleus and melting limit reaches zero size at the cutoff. We may conclude that melting becomes less and less thermodynamically favored as the cutoff is approached, and melting is not favored at all for voltages below the cutoff in the GT model, justifying the use of the SET-resistance (completely crystalline GST) on the V-R curve for these voltages. We note that because the PCM system is non-equilibrium and non-isothermal, thermodynamic descriptions of hypothetical time-dependent system behavior and properties given in this chapter are incomplete and not necessarily accurate, as described in more detail below. However, as approximations they are useful for introducing the properties of the melting limit and nucleus states.

A non-physical (i.e., numerical artifact) discontinuous cutoff also occurs in the BM VR-curve at $\sim$0.884V due to solutions no longer being attached to the bottom surface and therefore unreachable in the $0 < \theta < \pi/2$ $R(\theta)$ parametrization. Simulations vertically raising the origin position and using $0 < \theta < \pi$ (not shown) show the BM melting limits continuing to shrink for voltages $<\sim$0.884V. This cutoff is smaller than the heater size for all simulations in this research and therefore does not impact the calculation of required voltage for creating an amorphous dome which covers the heater.

The qualitative patterns of melting limit increasing in size with increasing voltage, nucleus decreasing in size, and GT model cutoff described above for the TBR-absent model are also found

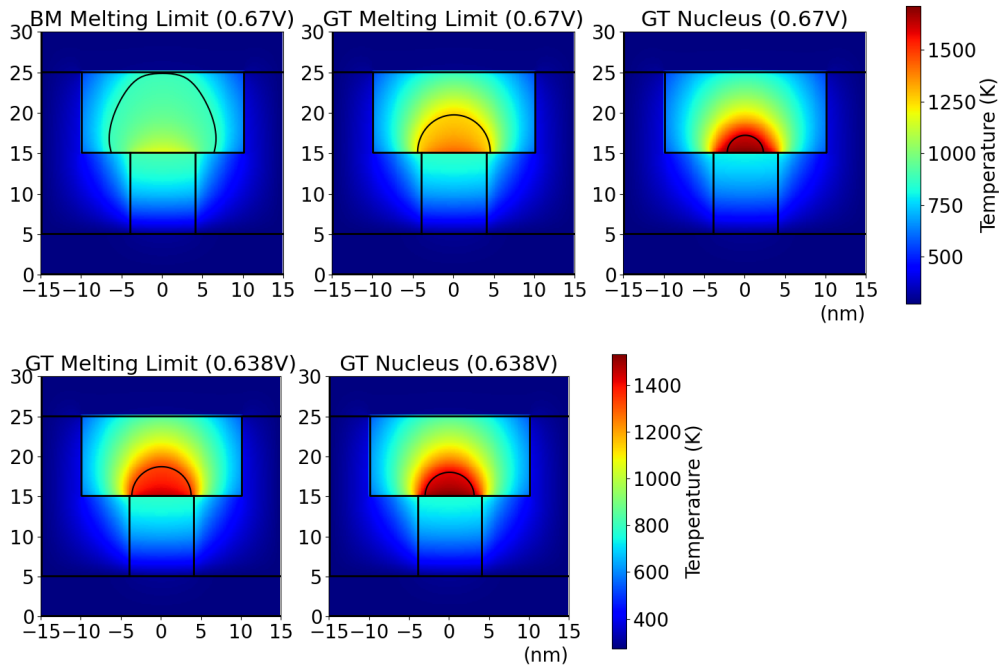

Figure 2.4: Steady states computed in the TBR-present case at 0.67V for the bulk melting model (BM) and Gibbs-Thomson model (GT), and for the GT model at V = 0.638V, at a scale of GST cell radius = 10nm.

in the TBR-present model. BM and GT steady states at 0.67V and GT steady states for 0.638V near the cutoff of $\sim$0.6349V are shown in Figure 2.4. Due to increased thermal resistance from TBR, lower voltage/heating is needed to reach equivalent points in the TBR-absent model. For example, the TBR-present GT cutoff voltage of $\sim$0.6349V is substantially lower than the TBR-absent GT cutoff of $\sim$1.0695V.

Results of steady state computations for the 10nm cell radius sized PCM device given in this chapter demonstrate how performance-relevant information can be derived from the melting limit and nucleus steady states. This example has shown substantial differences between the BM and GT models in terms of required voltage for RESET, as well as between the TBR-absent and TBR-present models, and also the voltage at which the above-described cutoff effect occurs. However, this chapter has also shown that these conclusions depend on the description of the time-dependent properties of the steady states being correct. Specifically, the claims that the melting limit is the final state of the melting process and that the nucleus state is a threshold for further growth of the

liquid to occur together justify the use of the melting limit for plotting V-R curves and deriving the required voltage for RESET, and also the cutoff being interpreted as a cutoff for melting to occur. As described above, the lack of rigorous thermodynamic arguments available to describe the time-dependent nature of the steady states means that more investigation is needed to fully confirm these properties of the steady states. We begin this process of investigation by first reviewing the comparisons between nucleation and growth in classical nucleation theory with the above RESET model.

2.3 Comparison of RESET model with classical thermodynamics

As stated in the Introduction section, the RESET model presented in this chapter does not include any assumptions about the potential stochastic or random nucleation of the initial liquid phase. This raises the question of how it is that a nucleus-like solution is appearing in the collection of steady states in the GT model, and how this state can be interpreted. This question is linked to a host of other issues related to this RESET model which make it unique in comparison with conventional thermodynamic models. In order to address all of these issues, we begin by reviewing classical nucleation theory and comparing with case of this RESET model.

Classical nucleation theory studies phase transformations occurring in a uniform background which is at equilibrium. Given the specific equilibrium conditions, an appropriate thermodynamic potential is identified which governs the phase transitions occurring in the system. For example, if the transformation is occurring at constant temperature and pressure, then the Gibbs free energy is the relevant thermodynamic potential. Processes which decrease the Gibbs free energy of the system are thermodynamically favored to occur, and processes which increase the Gibbs free energy are not favored. Take the case of a solid melting at a uniform temperature $T > T_m$, using the approximation of isotropic material properties. The Gibbs free energy of formation ΔG for a liquid sphere of radius r has two components, one negative contribution from the volume/bulk

phase transformation and one positive contribution from the cost of formation of the solid-liquid interfacial surface:

$$\Delta G = L\frac{T_m - T}{T_m}V(r) + \gamma A(r) \tag{2.9}$$

where L is the latent heat of transformation, and $V(r)$ and $A(r)$ are the volume and area of the sphere respectively. As a function of r, starting from $r = 0$, ΔG first increases then reaches a maximum before decreasing with further increase in r. The maximum point in ΔG occurs at:

$$\frac{d}{dr}\Delta G = 0 \tag{2.10}$$

$$L\frac{T_m - T}{T_m}\frac{d}{dr}V(r) + \gamma\frac{d}{dr}A(r) = 0 \tag{2.11}$$

This radius at which ΔG is maximized is called the classical nucleus radius. It is the barrier in free energy which must be overcome for the formation of the liquid to occur, before further increase in r will decrease the free energy and further growth will be favored. Rearranging (2.11) we obtain

$$1 = \frac{\gamma}{L}\frac{T_m}{T_m - T}\frac{dA/dr}{dV/dr} = \frac{\gamma}{L}\frac{T_m}{T_m - T}\frac{dA}{dV} \tag{2.12}$$

The expression $\frac{dA}{dV}$, which represents how much the area of the solid-liquid interface surface is incremented (dA) when the liquid volume is locally increased by dV, is actually identical with the negative of the mean curvature H (using the sign convention in this research) of the solid-liquid interface, giving:

$$1 = \frac{\gamma}{L}\frac{T_m}{T - T_m}H \tag{2.13}$$

$$T = T_m(1 + \frac{\gamma}{L}H) \tag{2.14}$$

This is the Gibbs-Thomson equilibrium criterion for a solid-liquid interface. This result occurs because the classical critical nucleus is naturally a state of equilibrium with respect to variations in r, because it is at the maximum point in the Gibbs energy and is therefore neither favored to grow nor shrink. However, it is an unstable equilibrium because small fluctuations in r would lead

the sphere to be favored to shrink for negative fluctuations and grow for positive fluctuations. We see here the immediate connection to the case of the RESET model used in this chapter. In that model, we begin with the Gibbs-Thomson equilibrium criterion and end up with a solution that is identified as having nucleus-like properties. In classical nucleation theory, we begin with Gibbs free energy of the total system and end up with the same Gibbs-Thomson criterion for the classical critical nucleus. In both cases, the nucleus solution is a reflection of the influence of solid-liquid interfacial energy, as reflected in either the Gibbs-Thomson criterion or the term in the total Gibbs free energy.

However, when we attempt to interpret the "nucleus" state in the RESET model in terms that are similar to classical nucleation theory, a major point of conflict emerges. The system in the RESET model is highly nonuniform in temperature and not in a state of global equilibrium, being constantly driven out of equilibrium by the applied current and resulting Joule heating. Therefore, we cannot describe the RESET model nucleus as being in a state of "unstable equilibrium" or even just "equilibrium". For systems with inhomogeneous intensive variables, there have been treatments in which the critical nucleus is assumed to be an extremum of a global free energy functional [52][53] [54] [55] [56] [57] [58] [59]. In other treatments, gradients of inhomogeneous intensive variables are allowed to contribute to the free energy or thermodynamic potential of the system used to identify a critical nucleus [60][61]. However, these thermodynamic approaches may not be feasible for PCM systems in which multiple intensive variables are inhomogeneous, and in which the system is *evolving* so as not to be in a state of equilibrium, even though there is the appearance of new phase. Moreover, there will always remain questions about how to identify nucleation in a system of such complexity that is consistent with the tenets of equilibrium thermodynamics. It is also not clear whether there is justification for the use of a global thermodynamic potential in describing the thermodynamics of the system, again due to the system being out of equilibrium. Therefore, we cannot use a global thermodynamic potential to derive the property of unstable equilibrium.

Furthermore, another point of comparison is, in the RESET model, the existence of the melting

limit and its relationship with the nucleus. In the classical nucleation theory case of homogeneous nucleation, the melting limit would simply be the entire container/mold undergoing phase change as the limit of the growth process of the new phase. However, in the highly non-uniform temperature as seen in the RESET model, the melting limit occurs before the entire container (the GST cell) is transformed. Significantly, the melting limit still has the Gibbs-Thomson effect applied to its interface, implying a thermodynamic connection or interpretation would be appropriate for it. It would tempting to use the interpretation that the melting limit corresponds approximately to a *minimum* in the Gibbs free energy as a function of (approximate) radius, and therefore would correspond to a state of stable equilibrium, where small increases or decreases in size would die out and the liquid shape would return to the melting limit shape. This would also help explain the ”cutoff” phenomena where no steady state solutions are found below a certain voltage, as the minimum (melting limit) and maximum (nucleus) in the Gibbs free energy would approach each other in size and then both vanish below the cutoff voltage. However, as stated previously we cannot justify the use of a global thermodynamic potential for this system and the melting limit is clearly still not in a state of equilibrium either, being driven out of equilibrium by the applied current.

Fundamentally, these problems can be addressed by noting the fact that the RESET model used in this research is completely deterministic and does not involve any global thermodynamic variables governing the time dependent dynamics. Therefore, the desired information about the time-dependent dynamics of the system can be derived purely from the kinetic properties of the model and there does not need to be any ambiguity in the interpretations that arise when dealing with global thermodynamic potentials in a non-equilibrium system. In the next chapter, this fact is used to derive information about the time dependent properties of the RESET melting model system.

Chapter 3

Time-dependent analysis of RESET melting process

3.1 Introduction

The research in this chapter further explores the phase change memory RESET melting process via time-dependent analysis of the classes of steady states computed in chapter 2. As explained in chapter 2, descriptions there of the time dependent properties of the steady states were made in a non-rigorous thermodynamic context.

In this chapter it is shown for the first time in phase change memory applications that it is not necessary to employ global classical thermodynamic arguments to model the states of the initial formation of liquid phase GST from solid GST in the RESET process that exhibit characteristics similar to the classical models of nucleation (or to model the formation of new phases in other nonequilibrium systems subject to large external field gradients, such as [52][53] [54] [55] [56] [57] [58] [59]). Instead, a linear stability analysis of steady state solutions using the governing set of kinetic equations is used to provide an accurate description of the time-dependent features of the evolution of the liquid that exhibits characteristics similar to the classical models of nucleation. In this chapter techniques are developed for characterizing solution branch behavior in both a realistic device model and in an imaginary spherically symmetric PCM model that allows the confirmation of the analogy of the much more complex nucleus and melting limit solutions found here with classical nucleation theory. In addition, in the spherically symmetric model time-dependent modeling of the melting process is performed, showing liquid evolution between the nucleus and melting limit states and confirming the correspondence with the features indicated by the stability analysis.

A linear stability analysis, based on perturbation theory, is a useful tool for analyzing the dynamical (time-dependent) tendencies of a system from a known calculated solution. The features of the analysis are summarized as follows. In general, the known steady state solutions, for example in this work, the liquid shape, the temperature and the electrical potential fields are referred to as the base state solutions. These general functions are expanded in asymptotic series about the base state in terms of a small parameter ϵ. The expanded functions are substituted into the fully time-dependent governing equations of the system, in this case those given in Chapter 2. The expanded

governing system of equations forms an ordered set of linear systems of equations proportional to increasing powers of the expansion parameter ϵ and denoted as the order 1 ($O(1)$) system (i.e. no factors of ϵ present), the $O(\epsilon)$ system, and on to the $O(\epsilon^n)$ systems, for n = 2, 3,... corresponding to increasingly higher powers of ϵ. A general procedure is to solve these sequence of systems in order of increasing power of ϵ, since the solutions at $O(\epsilon^n)$ will depend on the solutions at lower orders $O(\epsilon^p)$, p = n-1, n-2, ... The steady state solutions found with the $O(1)$ equations are the base state solutions. The $O(\epsilon)$ system is called the linear problem and is a homogeneous system of equations which takes the form of an eigenvalue problem. The eigenvalues are the growth rates of infinitesimal perturbations. Note, however, the homogeneous $O(\epsilon)$ system will not provide an estimate of the magnitude of the eigenfunctions and so the size of the perturbations is not uniquely determined as a solution to the $O(\epsilon)$ problem. Finite amplitude solutions may be found by proceeding to higher orders in ϵ. Here we are only interested in the stability of the base state solutions to infinitesimal perturbations that are always present in the system. Although the perturbations are infinitesimal, so that the magnitudes are indeterminant as part of the problem $O(\epsilon)$ solution, estimated, ad-hoc initial perturbations can be tracked in time using the growth rates (eigenvalues) found at $O(\epsilon)$, thereby approximating the time-dependent shape behavior. The linear approximation is reasonably accurate for systems sufficiently close to the base state and may provide a fairly robust prediction of time-dependent behavior for a limited range of system evolution away from the base state until nonlinear effects become important. The work required to solve higher order systems will not provide helpful information at this point.

The goal of the linear stability analysis is to obtain the growth rate of any perturbation mode to which the steady state shapes may be subject. The system is stable or unstable with respect a perturbation mode, based on whether or not the growth rate is positive or negative. Symbolically, the linearized system can be written:

$$\frac{d}{dt}R_1(t) = MR_1(t) \tag{3.1}$$

where $R_1(t)$ is a vector of the perturbed functions, and M is a linear operator, that is a combination of many factors. Equation (3.1) can be written

$$MR_1^i = \lambda_i R_1^i \tag{3.2}$$

Where the λ_i are the eigenvalues of the system that provide the perturbation growth rate. Solutions of (3.1) then exist in the form

$$R_1^i(t) = e^{\lambda_i t} R_1^i \tag{3.3}$$

Physically, this corresponds to exponential growth or decay of the perturbation with respect to time. In a real physical system, an actual perturbation could be an arbitrary function of position but the linear O(ϵ) system has the property that the sum of any number of solutions to the differential equations is also a solution. Therefore, a "general" perturbation, may be decomposed as a sum of the eigenfunctions of M, and each eigenfunction component may be viewed as evolving independently of the other eigenfunction components. Thus, we speak of perturbation "eigenmodes", or just "modes", corresponding to the eigenfunctions of M and analyze their behavior separately. Equation (3.3) tells us how different perturbation modes grow, shrink, or oscillate based on the eigenvalue λ_i and eigenfunction R_1^i . In general λ_i may be complex. The real part of λ_i provides the perturbation growth rate, the imaginary part denotes oscillation in time that may denote an onset of instability with standing or traveling waves. In this work all eigenvalues are real. If the real part of λ_i is positive (negative), equation (3.3) shows that the perturbation mode $R_1(t)$ will grow (decay), corresponding to an unstable (stable) mode. The different shape modes of the R_1^i eigenfunctions show how the unstable form varies spatially. We may choose either a positive sign or negative sign perturbation in cases in which symmetry is not preserved. If all perturbation modes are stable, then no perturbation will cause the system to move away from steady state and we say that the steady state as a whole is stable. If any of the perturbation modes are unstable, then the steady state is unstable. A linear stability analysis may be performed either analytically or numerically. In the analytical case all perturbation functions as well as the linear operator M

have closed form expressions. In the numerical case, the perturbation functions are discretized numerically, and the linear operator M is discretized as a matrix. The eigenfunctions of M are approximated by the eigenvectors of the discretized matrix form of M , and the eigenvalues of M by the eigenvalues of the matrix form of M.

In this chapter, not only is a linear stability analysis performed on the steady states of the RESET process, but in the section titled "Saddle-node bifurcation", a direct solution of the time-dependent evolution is also performed for a spherically symmetric approximate model. The spherical model exhibits similar stability characteristics compared to the non-spherical device analysis, but can be integrated to provide full dynamical behavior and so is additionally helpful in case well away from the base states for example in the "cutoff" region described in Chapter 2.

3.1.1 Simplifications for linear stability analysis

The equations governing transport and phase change in PCM materials used for the stability analysis of the full (non-spherical) device model are identical to the model used in Chapter 2, except for several simplifications. In this chapter we approximate temperature independent conductivity values for the fcc crystalline GST phase by sampling the temperature-dependent values given in Chapter 2 at a temperature 573K, halfway between room temperature and GST melting temperature. We obtain the values k = 0.95 W/(m·K) and $\sigma = 1.44 \times 10^5\ \Omega^{-1}\text{m}^{-1}$. Another difference from Chapter 2 is that we set the liquid phase GST conductivities as equal to the solid phase values. We also leave out thermoelectric effects and thermal boundary resistance, detailed in Chapter 2, in this chapter. The stability characteristics of the solution are not qualitatively dependent on these additional properties, and setting these simplifications makes the interpretation of the physical effects governing system behavior more transparent, meanwhile facilitating the quantitative evaluation.

3.2 Expansion

We seek to determine the stability threshold of the steady state nucleus and steady state melting limit solution branches of the governing equations presented in Chapter 2 using linear perturbation theory. To test the linear stability of the steady solutions the unknown functions $R(\theta,t)$, $\phi^i(r,\theta,t)$ and $T^i(r,\theta,t)$ are expanded in asymptotic series in powers of a small parameter ϵ:

$$R(\theta,t) = R^{(0)}(\theta) + \epsilon R^{(1)}(\theta,t) + O(\epsilon^2) \tag{3.4}$$

$$\phi_i(r,\theta,t) = \phi_i^{(0)}(r,\theta) + \epsilon\phi_i^{(1)}(r,\theta,t) + O(\epsilon^2) \tag{3.5}$$

$$T_i(r,\theta,t) = T_i^{(0)}(r,\theta) + \epsilon T_i^{(1)}(r,\theta,t) + O(\epsilon^2). \tag{3.6}$$

where the superscript '0' refers to the steady state or base-state solutions and the superscript '1' refers to the perturbed solutions. The subscript 'i' distinguishes between the material regions/phases. Expanded functions (3.4), (3.5), and (3.6) are substituted into the governing bulk equations and into the conditions at all boundaries and interfaces. At the GST solid-liquid phase change boundary, expressions for the the normal vector, mean curvature and the normal growth speed become expanded about the base state shape:,

$$\hat{n}[R(\theta,t)] = \hat{n}[R^{(0)}(\theta) + \epsilon R^{(1)}(\theta,t)] = \hat{n}^{(0)}(\theta) + \epsilon\hat{n}^{(1)}(\theta,t) + O(\epsilon^2) \tag{3.7}$$

$$H[R(\theta,t)] = H[R^{(0)}(\theta) + \epsilon R^{(1)}(\theta,t)] = H^{(0)}(\theta) + \epsilon H^{(1)}(\theta,t) + O(\epsilon^2) \tag{3.8}$$

$$v_n[R(\theta,t)] = v_n[R^{(0)}(\theta) + \epsilon R^{(1)}(\theta,t)] = 0 + \epsilon v_n^{(1)}(\theta,t) + O(\epsilon^2) \tag{3.9}$$

where:

$$\hat{n}_0 = \left[\hat{e}_r - \left(\frac{R_\theta^{(0)}}{R^{(0)}}\right)\hat{e}_\theta\right](1 + (R_\theta^{(0)})^2/(R^{(0)})^2)^{-1/2}, \tag{3.10}$$

$$= \left[R^{(0)}\hat{e}_r - R_\theta^{(0)}\hat{e}_\theta\right]((R^{(0)})^2 + (R_\theta^{(0)})^2)^{-1/2}, \tag{3.11}$$

$$\hat{n}^{(1)} = R^{(1)}\left[\frac{\partial \hat{n}^{(0)}}{\partial R^{(0)}(\theta)}\right] + R_\theta^{(1)}\left[\frac{\partial \hat{n}^{(0)}}{\partial R_\theta^{(0)}(\theta)}\right] \tag{3.12}$$

$$= \left[R^{(1)}((R^{(0)})^2 + (R_\theta^{(0)})^2)^{-1/2} - (R^{(1)}(R^{(0)})^2 + R_\theta^{(1)}R_\theta^{(0)}R^{(0)})((R^{(0)})^2 + (R_\theta^{(0)})^2)^{-3/2}\right]\hat{e}_r \tag{3.13}$$

$$+ \left[-R_\theta^{(1)}((R^{(0)})^2 + (R_\theta^{(0)})^2)^{-1/2} + (R_\theta^{(1)}(R_\theta^{(0)})^2 + R^{(1)}R_\theta^{(0)}R^{(0)})((R^{(0)})^2 + (R_\theta^{(0)})^2)^{-3/2}\right]\hat{e}_\theta \tag{3.14}$$

$$H^{(0)} = H(R^{(0)}) = ((R^{(0)})^2 + (R_\theta^{(0)})^2)^{-1/2}(2 - \frac{R_\theta^{(0)}}{R^{(0)}}\cot(\theta)) + (-R^{(0)}R_{\theta\theta}^{(0)} + (R_\theta^{(0)})^2)((R^{(0)})^2 + (R_\theta^{(0)})^2)^{-3/2} \tag{3.15}$$

and

$$H^{(1)} = -(R^{(0)}R^{(1)} + R_\theta^{(0)}R_\theta^{(1)})((R^{(0)})^2 + (R_\theta^{(0)})^2)^{-3/2}(2 - \frac{R_\theta^{(0)}}{R^{(0)}}\cot(\theta)) \tag{3.16}$$

$$+((R^{(0)})^2 + (R_\theta^{(0)})^2)^{-1/2}(\frac{R_\theta^{(0)}R^{(1)}}{(R^{(0)})^2} - \frac{R_\theta^{(1)}}{R^{(0)}})\cot(\theta) \tag{3.17}$$

$$+(-R^{(1)}R_{\theta\theta}^{(0)} - R^{(0)}R_{\theta\theta}^{(1)} + 2R_\theta^{(0)}R_\theta^{(1)})((R^{(0)})^2 + (R_\theta^{(0)})^2)^{-3/2} \tag{3.18}$$

$$-3(-R^{(0)}R_{\theta\theta}^{(0)} + (R_\theta^{(0)})^2)(R^{(0)}R^{(1)} + R_\theta^{(0)}R_\theta^{(1)})((R^{(0)})^2 + (R_\theta^{(0)})^2)^{-5/2} \tag{3.19}$$

and $v_n^{(1)}$ is defined below. After all of the substitutions are made and the expansions are carried out, the result is a sequence of equations at $O(1)$ and $O(\epsilon)$.

3.2.1 $O(1)$ base state problem

Throughout the bulk phases the leading order electrical potential obeys:

$$0 = \nabla^2\phi_i^{(0)}. \tag{3.20}$$

The voltage is set to the constant value V at the top electrode and to 0 at the bottom electrode. The device walls are insulating, $\nabla\phi_0^{(i)} \cdot \hat{n}_0 = 0$. In all phases, the base state temperature obeys the heat

equation with Joule heating:

$$0 = \nabla \cdot (k_i \nabla T_i^{(0)}) + \sigma_i \nabla \phi_i^{(0)} \cdot \nabla \phi_i^{(0)}. \tag{3.21}$$

At the crystal-melt GST interface, the Gibbs-Thomson condition is obeyed:

$$T = T_m(1 + \frac{\gamma}{L} H^{(0)}) \tag{3.22}$$

and there is the conservation of energy:

$$0 = k_L \nabla T_L^{(0)} \cdot \hat{n}^{(0)} - k_S \nabla T_S^{(0)} \cdot \hat{n}^{(0)}. \tag{3.23}$$

At all internal immobile interfaces within the device, the normal components of the heat flux and current density are continuous and all other boundary conditions given in the model remain unchanged. The leading order problem is the steady state version of the model equations presented in the introductory section. The $O(1)$ set of governing equations provide the base state nucleus and melting limit solution branches.

The steady state base state solution branches are calculated using the iterative numerical solution method described in detail in Chapter 2.

3.2.2 $O(\epsilon)$ linear stability problem

The $O(\epsilon)$ perturbed governing bulk transport equations are:

$$\nabla^2 \phi_i^{(1)} = 0 \quad \text{and} \tag{3.24}$$

$$\nabla^2 T_i^{(1)} = 2\frac{\sigma_i}{k_i} \nabla \phi_i^{(0)} \cdot \nabla \phi_i^{(1)}. \tag{3.25}$$

Typically the thermal fields obey fully time-transient heat equations. However, near the onset of instability, the time scale associated with the diffusion of heat may be assumed rapid relative to

the time scale associated with the growth or decay of interface perturbations. Therefore, we can assume that the $O(\epsilon)$ thermal equations obey a quasi-static approximation, meaning that at any fixed time they satisfy steady state heat equations (Eq. (3.25)).

The boundary conditions are $\phi^{(1)} = 0$ at the top and bottom of the device, $\nabla\phi_i^{(1)} \cdot \hat{n} = 0$ and $T_i^{(1)} = 0$ at the outer device side boundaries, $\sigma_i \nabla\phi_i^{(1)} \cdot \hat{n} = \sigma_j \nabla\phi_j^{(1)} \cdot \hat{n}$ and $k_i \nabla T_i^{(1)} \cdot \hat{n} = k_j \nabla T_j^{(1)} \cdot \hat{n}$ at all interior immobile interfaces between material regions where $\hat{n}$ represents the normal to the particular boundary considered. At the solid-liquid GST interface, the O(ϵ) energy balance is:

$$\frac{L}{k_L} v_n^{(1)} + (\nabla T_L^{(1)} + R_1(\theta) \frac{\partial(\nabla T_L^{(0)})}{\partial r}) \cdot \hat{n}^{(0)} + \nabla T_L^{(0)} \cdot \hat{n}^{(1)} = \frac{k_S}{k_L} ((\nabla T_S^{(1)} + R_1(\theta) \frac{\partial(\nabla T_S^{(0)})}{\partial r}) \cdot \hat{n}^{(0)} + \nabla T_S^{(0)} \cdot \hat{n}^{(1)}) \tag{3.26}$$

where the S and L superscripts refer to the solid and liquid GST phases, respectively. The continuity of the normal component of the current (charge conservation) at the GST solid-liquid interface is:

$$\sigma_L ((\nabla\phi_L^{(1)} + R^{(1)}(\theta) \frac{\partial(\nabla\phi_L^{(0)})}{\partial r}) \cdot \hat{n}_0 + \nabla\phi_L^{(0)} \cdot \hat{n}^{(1)}) = \sigma_S ((\nabla\phi_S^{(1)} + R^{(1)}(\theta) \frac{\partial(\nabla\phi_S^{(0)})}{\partial r}) \cdot \hat{n}^{(0)} + \nabla\phi_S^{(0)} \cdot \hat{n}^{(1)}) \tag{3.27}$$

and the continuity of temperature is:

$$R^{(1)}(\theta) \frac{\partial T_L^{(0)}}{\partial r} + T_L^{(1)} = R^{(1)}(\theta) \frac{\partial T_S^{(0)}}{\partial r} + T_S^{(1)} = \frac{T_m \gamma}{L} H^{(1)}. \tag{3.28}$$

All perturbed temperatures and temperature gradients written in these perturbed equations are evaluated at the location of the unperturbed interface shape, $R^{(0)}(\theta)$. The right hand side of Eqn. (3.28) in the leading order temperature continuity equation is the $O(\epsilon)$ contribution from the Gibbs-Thomson equation. Finally, continuity of the solid-liquid interface gives:

$$v_n^{(1)} = \left[\frac{dR^{(1)}/dt}{(1 + (R_\theta^{(0)}/R^{(0)})^2)^{1/2}} \right]. \tag{3.29}$$

3.2.3 The boundary element method

Given a shape perturbation, characterized by $R^{(1)}(\theta)$, the first order thermal and electrical potentials $T_i^{(1)}$ and $\phi_i^{(1)}$ may be uniquely determined throughout the entire domain as the solution of a boundary value problem. The gradients of the perturbed thermal fields are substituted into the perturbed solid-liquid GST interfacial energy condition, to give the growth rates of the perturbations, $v_n^{(1)}$. Since the solution procedure is carried out numerically, discretization of the GST interfacial energy condition leads to a homogeneous linear system, the eigenvalues of which are the growth rates of the perturbations. If any eigenvalues are positive the base state solution is unstable, if all are negative, the base solution is stable.

Because the device geometry is characterized by rotational symmetry about the longitudinal coordinate axis, if there are non-uniform electric and thermal fields throughout the domain, the steady-state liquid GST base state region will not conform to any grid contour used to numerically solve the perturbed problem. In addition, numerical evaluation of the GST interfacial conditions (3.26) and (3.27) occurs at the arbitrarily shaped solid-liquid GST interface. Thus, we use a boundary integral formulation to more accurately solve the perturbed quasi-static heat equation (3.25). The boundary integral method maps the problem entirely to the 2D boundaries between PCM material regions/phases, reducing its spatial dimensionality. Numerical implementation is with a boundary element method (BEM), in which the Laplace equation for the temperature is expressed through boundary integral equations involving a Green's functions for each discrete boundary element. The result of the discretization is a stability matrix that is used to predict conditions for liquid pool stability.

The boundary integral equations used in this stability analysis are derived by following a method described in [62], valid for axisymmetric problems. Boundary integral equations are applied separately to each of the seven bounded material/phase regions in the PCM device (shown in Figure 2.1), with the boundary elements defined as follows. The 1D cross section of all rectangular boundaries, including boundaries between adjacent regions, are divided into discrete line segments with lengths equal to a constant factor, 2.0 or 4.0, times the FiPy cell spacing. Meanwhile, the GST

L-S boundary retains the previously-described discretization of $R^{(0)}(\theta)$. For each material/phase region there is a set of boundary integral equations of the form:

$$\frac{1}{2}T_{\alpha}^{(1)} = \Sigma_{\beta}\int_{\beta}(T_{\beta}^{(1)}\frac{\partial G_{\alpha}}{\partial n} - \frac{\partial T_{\beta}^{(1)}}{\partial n}G_{\alpha})dA \tag{3.30}$$

applied to each boundary element α in that region. The index β sums over each boundary element, the integral denoting surface integration over the rotated surface of the individual boundary element segment of area dA. $\frac{\partial}{\partial n}$ denotes differentiation along the normal to the interface. G^{α} is a Green's function for the Laplacian:

$$G_{\alpha}(x,y,z,x_0^{\alpha},y_0^{\alpha},z_0^{\alpha}) = -\frac{1}{4\pi\sqrt{(x-x_0^{\alpha})^2+(y-y_0^{\alpha})^2+(z-z_0^{\alpha})^2}} \tag{3.31}$$

where $x_0^{\alpha}, y_0^{\alpha}, z_0^{\alpha}$ is the center point of boundary element α in the $x-z$ cross-section and $y_0 = 0$. The factor of $1/2$ on the LHS of equation (3.30) is correct because the Green's function is centered directly on the boundary element surface.

The temperature is discretized by approximating $T^{(1)}$ and its spatial derivatives as uniform across each boundary element surface segment. Following [62], 2D boundary surface integrals are reduced to 1D integrals over the cross sections of the boundary segments, where the integrals of the Green's functions over the spherical azimuthal coordinate become complete elliptic integrals of the first and second kinds. Specifically, for given boundary segments α and β,

$$\int_{\beta}(T_{\beta}^{(1)}\frac{\partial G_{\alpha}}{\partial n} - \frac{\partial T_{\beta}^{(1)}}{\partial n}G_{\alpha})dA = \int_{\beta}(T_{\beta}^{(1)}\Psi(r,z,r_0,z_0;n_r,n_z) - \frac{\partial T_{\beta}^{(1)}}{\partial n}\Phi(r,z,r_0,z_0))dL \tag{3.32}$$

where r and z are the cylindrical coordinates along the 1D cross-sections of the boundary element β, and dL indicates 1D integration over the cross section line segment, r_0 and z_0 are the cylindrical coordinates of the Green's function center x_0, y_0, z_0., and

$$\Psi(r,z,r_0,z_0;n_r,n_z) \equiv \frac{-1}{\pi\sqrt{a}}(\frac{n_r}{2r}[\frac{a-2rr_0}{a-4rr_0}E(\frac{4rr_0}{a}) - K(\frac{4rr_0}{a})] + n_z\frac{z_0-z}{a-4rr_0}E(\frac{4rr_0}{a})) \tag{3.33}$$

$$\Phi(r, z, r_0, z_0) \equiv \frac{-1}{\pi\sqrt{a}} K(\frac{4rr_0}{a}) \tag{3.34}$$

$$a \equiv r^2 + r_0^2 + (z - z_0)^2 + 2rr_0 \tag{3.35}$$

where the functions K and E are elliptic integrals of the first and second kind, respectively. Here, elliptic integrals of the first and second kind are computed using implementations "ellipe" and "ellipk" available in the Python package "scipy". The resulting 1D integrals on the RHS of (3.32) are computed using the "quad" function in the scipy package. Green's functions have singularities at $x_0, 0, z_0$ for cases where the Green's function is centered around the boundary element being integrated over. The singularities are treated by first removing 0.1% of the total boundary segment, centered around the singularity, from the integrated domain. The Taylor expansion of the complete elliptic integral of the first kind is carried out around the standard elliptic integral parameter value m = 1 using the scipy function "ellipkm1" whenever m $>$ 0.99, which occurs near the singularity.

After factoring out the constant values of $T_\alpha^{(1)}$ and $\frac{\partial T_\alpha^{(1)}}{\partial n}$ for each boundary element α from the boundary integrals and then computing the integrals, the equations become a set of linear equations for the values of $T_\alpha^{(1)}$ and $\frac{\partial T_\alpha^{(1)}}{\partial n}$. A complete system of linear equations is formed by combining all of these equations for all five of the PCM regions, with all of the interior energy conservation boundary conditions of the form

$$k_i(\frac{\partial T_\alpha^{(1)}}{\partial n})^i = k_j(\frac{\partial T_\alpha^{(1)}}{\partial n})^j \tag{3.36}$$

where i and j are neighboring material regions, and α denotes each boundary element shared between the two regions. For the outer boundaries and solid-liquid interface, Dirichlet boundary conditions are operative, and so the $T_\alpha^{(1)}$ at these boundaries act as fixed values in the system of equations rather than variables. For the device outer boundaries, with the outer boundary condition $T^{(1)} = 0$, all terms containing these $T_\alpha^{(1)}$ vanish. For the solid-liquid interface, the Dirichlet boundary values for each boundary element are governed by (3.28) and are described by the vector of values

$$T^{(1)}_{\alpha(SL)} = A^{(1)}_{\alpha\beta} R^{(1)}_{\beta} \tag{3.37}$$

where $A^{(1)}_{\alpha\beta}$ is the discretized matrix form of the linear operation derived from (3.28), which takes a perturbation $R^{(1)}(\theta)$ and produces $\frac{T_m \gamma}{L} H^{(1)}(\theta) - R^{(1)}(\theta) \frac{\partial T^{(0)}_S}{\partial r}$, and $R^{(1)}_{\beta}$ is the vector discretized form of the perturbation $R^{(1)}(\theta)$. This matrix is constructed by using second-order finite difference matrices for the derivatives $R^{(1)}_{\theta}(\theta)$, $R^{(1)}_{\theta\theta}(\theta)$ in (3.16)-(3.19) and (3.28). The (SL) subscript denotes that only solid-liquid interface $T^{(1)}$ values are being ranged over.

Another matrix $B_{\alpha\beta}$ is then constructed which converts the Dirichlet $T^{(1)}_{\beta(SL)}$ data into the solid-liquid interface normal velocity:

$$v_{n\alpha} = B_{\alpha\beta} T^{(1)}_{\beta(SL)} \tag{3.38}$$

This is done by arranging the complete system of equations into the form Ax = b, and considering that x = A^{-1}b and calculating the inverse of A, then constructing the new matrix by keeping track of where the data corresponding to the solid-liquid interface $T^{(1)}_{\alpha}$ values are located, and computing the matrix that would correspond to implementing the expression for the normal velocity in (3.26). We then convert to a final matrix expression for $\frac{\partial}{\partial t} R^{(1)}(\theta, t)$ values by combining (3.37) and (3.38) and adding a factor of $((R^{(0)}(\theta))^2 + (R^{(0)}_{\theta}(\theta))^2)^{1/2} / R^{(0)}(\theta)$ derived from (3.29):

$$\frac{dR^{(1)}_{\alpha}}{dt} = \sum_{\beta=1,n} M_{\alpha\beta} R^{(1)}_{\beta} \tag{3.39}$$

allowing the relationship between the growth rate of the perturbation $R^{(1)}_{\beta}$ and the original perturbation to be expressed directly by the linear stability matrix $M_{\alpha\beta}$.

For perturbation vectors $R^{(1)}_{\alpha}$ which are eigenvectors of $M_{\alpha\beta}$ with eigenvalue σ, solving the differential equation produced by (3.39) gives:

$$R^{(1)}_{\alpha}(\theta, t) = e^{\sigma t} R^{(1)}_{\alpha}(\theta, 0) \tag{3.40}$$

For real σ, eigenvectors with $\sigma > 0$ grow exponentially and are linearly unstable modes, and eigenvectors with $\sigma < 0$ shrink exponentially and are linearly stable modes. The imaginary component of σ adds time oscillation to this growth pattern.

For each simulated case, the complete set of eigenvectors and eigenvalues of $M^{\alpha\beta}$ are computed using the "eig()" function from the "NumPy" Python package. (s^{-1})

3.3 Results of time-dependent analysis

3.3.1 Stability of base states: Eigenvectors, growth patterns, and interpreting the nucleus and melting limit states

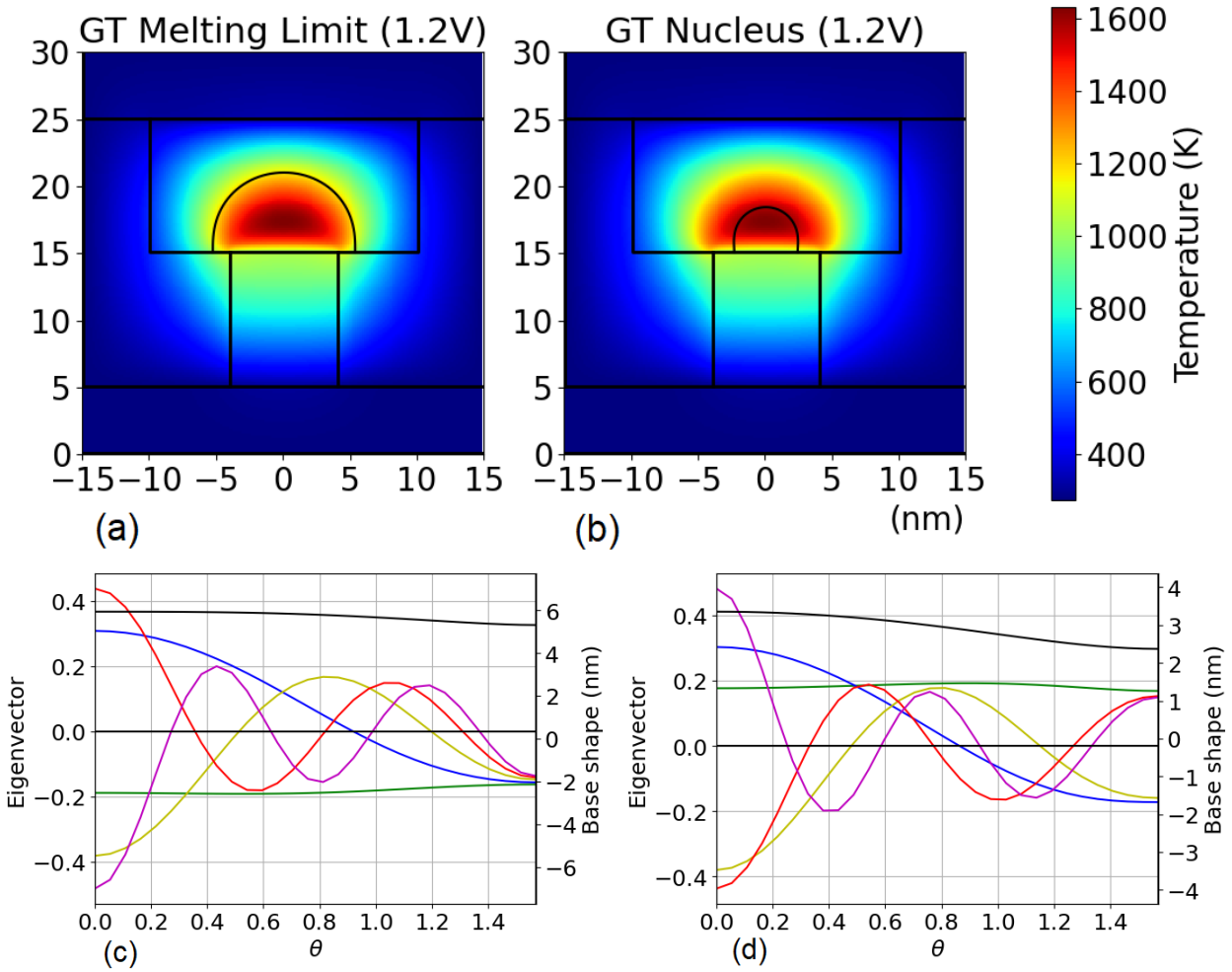

Figure 3.1: (a)-(b) Melting limit and nucleus steady states computed for a cell radius of 10nm and applied voltage of 1.2V. Black lines separate phase/material regions, corresponding to those in Figure 2.1. (c)-(d) Eigenvectors of matrix $M^{\alpha\beta}$ for melting limit (left) and nucleus (right) solutions. Shown as functions $R_1(\theta)$ in the range $0 \leq \theta \leq \pi/2$. For each solution the eigenvector colors green, blue, yellow, red and purple are ordered in decreasing magnitude of eigenvalue. For comparison the base state shapes $R_0(\theta)$ are also included as the black line. The only positive eigenvalue (unstable) mode is the green line in (d) (nucleus).

With the conventional device geometry, for both the melting limit and the nucleus solutions, all eigenvalues σ of $M^{\alpha\beta}$ are found to be real. When ordered, the eigenvalues form a sequence, decreasing in value, the maximum value of which is positive for the nucleus solution and negative for the melting limit solution. The positive eigenvalue mode is the sole unstable mode appearing in either the melting limit or nucleus solutions. As an example, we show the case of a device with a cell radius of 10 nm and with an applied voltage of 1.2V. The steady states for this case are shown in Figure 3.1. The melting limit solution has as its maximum five eigenvalues (-0.158, -472, -1910, -5100, -10800)10^{13} s^-1 and the nucleus solution has maximum eigenvalues (1.12, -1300, -9880, -31000, -69900)10^{13} s^-1. Given the signs of the eigenvalues, we see that the net result is that the melting limit solution is stable and the nucleus solution is unstable with respect to the growth of a perturbation.

Eigenvectors corresponding to the five maximum eigenvalues for the melting limit and nucleus solutions in the 10 nm, 1.2V case described above, are plotted in Figure 3.1. These are interpolated plots of the discretizations of the functions defined as $R^{(1)}(\theta)$ in Eqn. (9) and are plotted over the θ nodes in the range $0 \leq \theta \leq \pi/2$. The eigenvectors corresponding to the maximum eigenvalues of the two solutions are shown in green in Figure (3.1). For both solutions the eigenvector is comparatively flat, and is shown as a contraction of the liquid pool for the melting limit and an expansion in the nucleus pool depending on the sign assigned to the multiplicative factor associated with the eigenvector. Growth of the mode in these cases would correspond, within the linear approximation, to either outward growth of the liquid region (for a positive-sign perturbation) or inward shrinkage of the liquid region (for a negative sign perturbation).

In order of decreasing eigenvalue, the next eigenvector $R^{(1)}(\theta)$ (blue) changes sign once over the domain range shown, the next smaller eigenvalue (lime green) has an eigenvector that changes sign twice over the domain range and so on as shown in Figure (3.1). It is observed that the more times the eigenvector changes sign over the domain, corresponding to shorter effective wavelengths of the perturbation, the more negative is the eigenvalue. The more oscillating eigenvectors have more total surface area, and therefore surface energy, associated with the particular perturbation.

Considering that the negativity of the eigenvalue corresponds to the rate of exponential shrinkage of the perturbation, it is likely that the increasingly negative eigenvalues reflect the increasing interfacial energy cost for forming area-increasing oscillations. In addition, the increasing curvature of the oscillations modulates the local temperature via the Gibbs-Thomson effect, modifying the interfacial temperature gradients and therefore the heat flux at the solid-liquid interface resulting in further stabilization.

The nucleus maximum eigenvalue being positive ($1.12{\cdot}10^{13}\mathrm{s}^{-1}$) in addition to the relatively flat unstable eigenvector shows that within the linear approximation the unstable nucleus steady state is nearly identical to an unstable classical critical nucleus in terms of its kinetic evolution: a small increase in size results in further growth, roughly evenly across $0 < \theta < \pi/2$, and a small decrease in size results in further shrinkage of the pool. The unstable perturbation (green) indicates a net increase in liquid pool size in addition to an increase in total surface area. In order for the pool to be unstable, the energy benefit from the amount of solid that has transformed to liquid outweighs the energy penalty arising from the added surface area. This is analogous to the argument of classical nucleation theory. This connection with classical nucleation theory is further confirmed by taking the hypothetical limit as cell size approaches infinity. The size of the nucleus solution relative to the spatial variation in temperature approaches zero, and therefore the entire volume covering the nucleus is isothermal. Local interfacial equilibrium as expressed by the Gibbs-Thomson equation would cause it to be a sphere of radius $R_{nuc} = 2\gamma T_m/L(T_C - T_m)$, the value found in classical nucleation theory (CNT).

On the other hand, the melting limit solution is linearly stable, shown by having entirely negative eigenvalues, including the maximum eigenvalue. This means that at steady state, infinitesimal perturbations do not result in growth or decay of the pool size or of a change in pool shape. The melting limit liquid pool is a stable fixed point in the melting system. At the melting limit the continuous generation of Joule heat in the device is balanced by the conductive flow of heat out of the device leading to the steady state. The melting solution represents the maximum size that the liquid pool can attain given the inhomogeneous, steady-state thermal profile. In this manner it represents

the final state of the system in which liquid and solid GST coexist. Steady state is not equilibrium, but the melting limit is nonetheless analogous to the stable final state of equilibrium coexistence of solid-liquid phases at the isothermal transition temperature. Thus, the kinetic behavior of both melting limit and nucleus has an analog in classical thermodynamics.

The overall dynamical system behavior may be summarized as follows: If a liquid region forms which is smaller than the nucleus, it will shrink back down to zero size. If the region is larger than the nucleus, it will continue growing until settling into the melting limit. So, the nucleus represents the barrier which must be overcome for melting to occur until reaching the stable melting limit state.

3.3.2 Non-spherical (device) melting behavior as a function of voltage

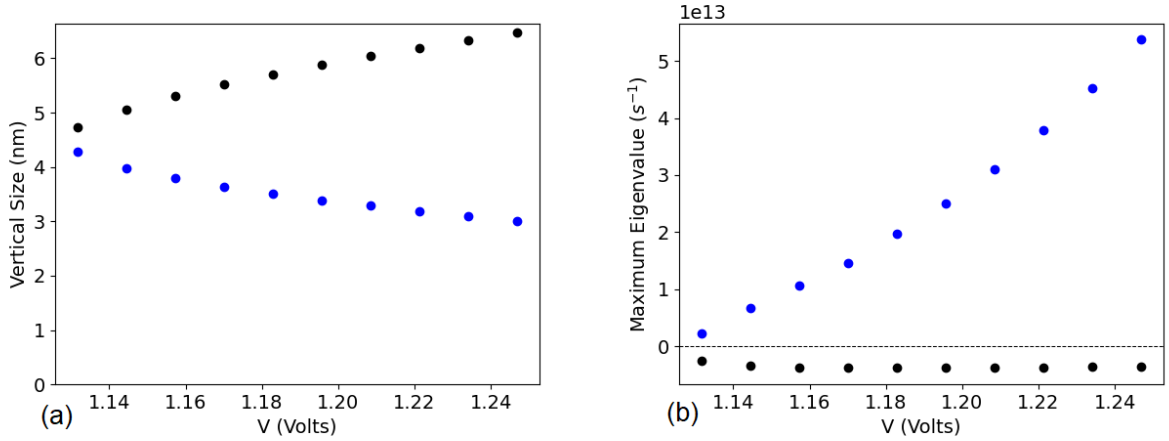

Figure 3.2: (a) Vertical sizes of melting limit (black) and nucleus (blue) solutions as measured from the center of the GST-heater interface to the center-top of the liquid dome. (b) Maximum eigenvalues of the linear stability matrix $M^{\alpha\beta}$, defined in the above section, for the melting limit (black dots) and nucleus (blue dots) steady states. The cell radius is 10nm and the voltage range is taken near the cutoff voltage, approximately 1.129V.

Varying the applied voltage, trajectories of the nucleus and melting solution branches are traced. In Figure (3.2) the vertical size, measured from the center of the GST-heater interface to the top of the liquid dome, and maximum eigenvalues of $M^{\alpha\beta}$ for the nucleus and melting limit solutions are plotted as a function of the applied voltage. As the critical value $\sim$1.129V is ap-

proached in the direction of decreasing voltage, the vertical size of the nucleus and melting limit approach each other and the full shapes (not shown) also converge at all points in θ. No steady state solutions are found numerically for voltages below $\sim$1.129V, denoted the cutoff voltage. For voltages above the cutoff voltage, the above analysis of the nucleus and melting limit predicts that the set of states for which growth is favored are those states whose size is in between the nucleus and melting limit states. As the cutoff voltage is approached, the space between the nucleus and melting limit becomes smaller and smaller, approaching zero until finally the collection of states for which growth is favored vanishes. The eigenvalue data as a function of voltage implies that the magnitude of the kinetic rate for melting to proceed from the nucleus to the melting limit, represented by the magnitude of the unstable nucleus eigenvalue (blue dots), approaches zero as the cutoff is approached. Below the cutoff voltage, we may conclude that melting is not favored and the liquid region does not appear.

3.4 Time-dependent analysis in the spherically symmetric approximation

For illustrative purposes we consider a simplified, spherically-symmetric approximation of the model of transport and interfacial dynamics in a PCM device given by Equations (2) through (8). The phase change material is a sphere of radius r_C. The cladding surrounding the PCM is a thermal reservoir at fixed temperature T_C. It is assumed that the electrical properties do not play a significant role in the dynamics, other than to allow Joule heating. The Joule heating per unit volume is uniform everywhere and denoted $\dot{q}$. The solid and liquid thermal conductivities are assumed equal, k_S. Since the temperature $T(r) = T_C$ at the spherical outer solid boundary $r = r_C$ the interface between the solid and liquid PCM material is assumed to be spherical in the base state. Here we investigate the stability of this spherical base state to only spherically-symmetric perturbations. This constraint on the perturbation eigenmode is justified by the numerical stability analysis of non-spherically symmetric base-state shapes shown in the next section in which the

unstable eigenmode is either a dilation or compression of the base state (by accretion, not strain).

The dimensional model is scaled according to:

$$r = R\left[\frac{\gamma}{L}\right],\ t = \tau\left[\frac{\gamma^2}{LT_m k_S}\right],\ \dot{q} = \dot{Q}\left[\frac{k_S T_m L^2}{\gamma^2}\right],\ T = U\left[T_m\right] + T_m, \tag{3.41}$$

$$T_C = U_C\left[T_m\right] + T_m,\ r_L = R_L\left[\frac{\gamma}{L}\right],\ h = H\left[\frac{L}{\gamma}\right],\ k = Kk_S \text{ and } v_n = V_N\left[\frac{T_m k_S}{\gamma}\right], \tag{3.42}$$

where the unscaled, dimensional variables are on the left hand sides of the equal signs, and U_C and R_L are the dimensionless outer boundary temperature and the dimensionless interface radius, respectively. The steady state spherically symmetric equations are solved to determine the base state. The result is a cubic equation for determination of the phase change material solid-liquid interface radius:

$$-R_L^3 + \left(R_C^2 + \frac{6U_C}{\dot{Q}}\right)R_L - \frac{12}{\dot{Q}} = 0. \tag{3.43}$$

The temperature field and the coefficient in the cubic equation above are written in terms of the control parameter U_C. Since the choice of U_C also fixes the temperature U_H at the center of the liquid PCM via the relationship,

$$U_C = -\frac{\dot{Q}}{6}R_C^2 + U_H \tag{3.44}$$

then, an equivalent cubic equation for the interface position may be written,

$$-R_L^3 + \left(\frac{6U_H}{\dot{Q}}\right)R_L - \frac{12}{\dot{Q}} = 0. \tag{3.45}$$

Further scaling $\tilde{R}_L = R_L U_H$ and $\alpha = \dot{Q}/(6U_H^3)$ leads to a one parameter base-state equation governing spherically symmetric solutions,

$$-\alpha\tilde{R}_L^3 + \tilde{R}_L - 2 = 0. \tag{3.46}$$

The discriminant of the LHS of (3.46) is $4(\frac{1}{\alpha^3} - \frac{27}{\alpha^2})$, and is positive for $\alpha < 1/27$ and negative

for $\alpha > 1/27$. No allowable solutions $\tilde{R}_L$ exist for $\alpha > 1/27$, showing that there are no liquid spheres of any radius which satisfy steady state in this range. For $\alpha < 1/27$, two real roots $\tilde{R}_L$ of (3.46) are found that represent physical liquid pools. These two roots are plotted as a function of α in Figure 3.3.

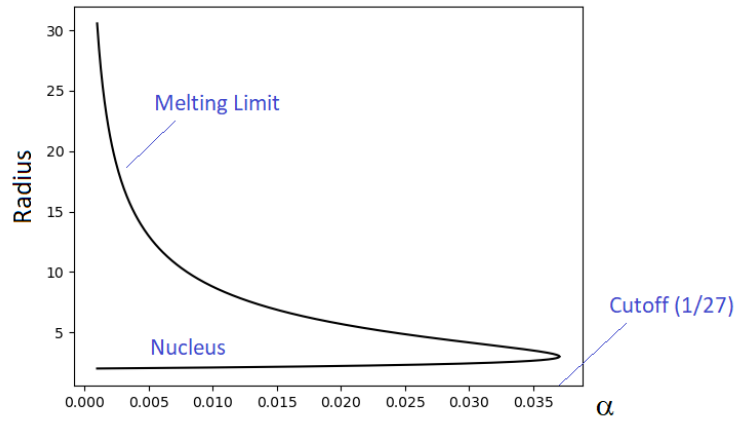

Figure 3.3: Scaled dimensionless radius $\tilde{R}_L$ (defined above) of nucleus and melting limit steady states in spherically symmetric PCM system as a function of dimensionless parameter α (defined above). The decimal value of $1/27$ is $0.\overline{037}$.

As $\alpha \to 0$ the system becomes isothermal at the temperature U_H. In this limit the smaller radial solution approaches the radius $\tilde{R} = 2$ whereas the larger solution approaches infinity. At $\alpha = 0$ the smaller solution appears to be that of a classical critical liquid nucleus forming in a superheated solid at scaled isothermal temperature U_H, since the Gibbs-Thomson condition (1.4) at the solid-liquid interface shows that the liquid radius is (unscaled) $R_{nuc} = 2\gamma/L(T_H - T_m)/T_m$, the value found in classical nucleation theory. As α increases, the system becomes increasingly non-isothermal due to the effect of the $-\alpha\tilde{R}^2$ term in the thermal field. For fixed α greater than zero the larger radial solution is finite and presumably corresponds to a larger melting limit pool. The nucleus and melting limit solutions approach each other and merge at $\alpha = 1/27$.

The two steady state solution branches are tested for stability. For both branches, the following procedure is applied. For a given α the temperature and the shape functions are expanded in series

about the base state,

$$\tilde{U}(\tilde{R},\tilde{\tau}) = 1 - \alpha\tilde{R}^2 + \epsilon\tilde{U}^{(1)}(\tilde{R},\tilde{\tau}) + O(\epsilon^2) \tag{3.47}$$

$$\tilde{R}_L(\tilde{\tau}) = \tilde{R}_L^{(0)} + \epsilon\tilde{R}_L^1(\tilde{\tau}), \tag{3.48}$$

where ϵ is a small parameter and the perturbed states are also spherically symmetric.

The expansion of the system of equations to first order in ϵ leads to the following solutions. The boundary condition at $\tilde{R}_L^{(0)}$ (solid-liquid base state interface) is

$$\tilde{U}^{(1)}(\tilde{R}_L^{(0)},\tilde{\tau}) = \beta\tilde{R}_L^{(1)}(\tilde{\tau}), \text{ where } \beta \equiv 2\alpha\tilde{R}_L^{(0)} - \frac{2}{(\tilde{R}_L^{(0)})^2}. \tag{3.49}$$

The heat equation is solved to give the $O(\epsilon)$ liquid temperature,

$$\tilde{U}_L^{(1)}(\tilde{R},\tilde{\tau}) = \beta\tilde{R}_L^{(1)}(\tilde{\tau}) \tag{3.50}$$

and solid temperature,

$$\tilde{U}_S^{(1)}(\tilde{R},\tilde{\tau}) = \frac{(\tilde{R}-\tilde{R}_C)\tilde{R}_L^{(0)}}{(\tilde{R}_L^{(0)}-\tilde{R}_C)\tilde{R}}\beta\tilde{R}_L^{(1)}(\tilde{\tau}) \tag{3.51}$$

Finally, the energy balance at the solid-liquid interface has perturbed normal velocity $\tilde{V}_n^{(1)}(\tilde{\tau})$ $= \tilde{R}_L^{(1)'}(\tilde{\tau})$ leading to the definition,

$$\tilde{R}_L^{(1)'}(\tilde{\tau}) = \sigma\tilde{R}_L^{(1)}(\tilde{\tau}) \tag{3.52}$$

where the eigenvalues σ are the growth rates. Since $\tilde{V}_n = \tilde{R}_L'(\tilde{\tau})$, $\tilde{V}_n^{(1)} = \tilde{R}_L^{(1)'}(\tilde{\tau})$ then the energy balance at the interface gives:

$$(\frac{1}{(\tilde{R}_L^{(0)}-\tilde{R}_C)} - \frac{1}{\tilde{R}_L^{(0)}})\beta\tilde{R}_L^{(1)}(\tilde{\tau}) = \sigma\tilde{R}_L^{(1)}(\tilde{\tau}) \tag{3.53}$$

leading to an expression for the eigenvalues:

$$\sigma = (\frac{1}{(\tilde{R}_L^{(0)} - \tilde{R}_C)} - \frac{1}{\tilde{R}_L^{(0)}})\beta. \tag{3.54}$$

The parenthetical factor in (3.54) always evaluates to a negative value because the outer cladding radius $\tilde{R}_C$ must be greater than the base state radius $\tilde{R}_L^{(0)}$. Therefore, the sign of σ is opposite the sign of β. Values of β as a function of α are plotted in Figure 3.4. It is seen that the nucleus

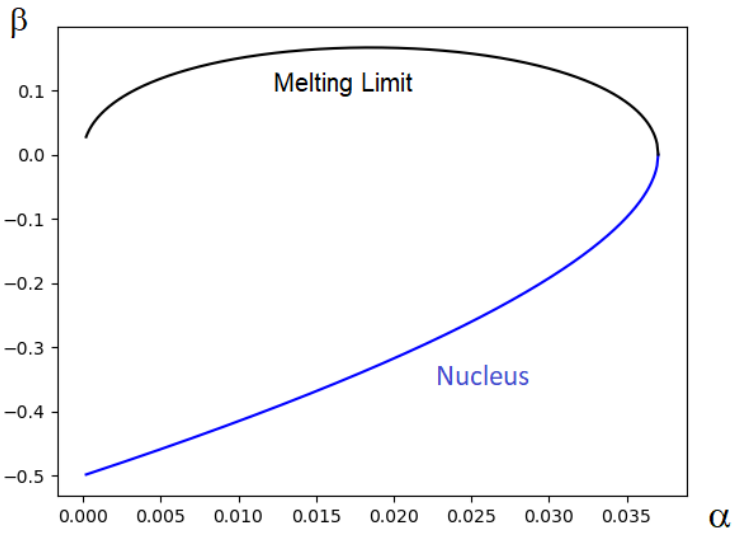

Figure 3.4: Value of β (defined above) as a function of α for melting limit and nucleus states in spherically symmetric PCM system. β has opposite sign to the eigenvalue σ determining the stability of the melting limit and nucleus states.

state values are less than zero and the melting limit values are greater than zero, corresponding to unstable and stable states, respectively, given that the sign of β is opposite the sign of the eigenvalue σ. This means that for the smaller nucleus solution, a small spherically symmetric increase in the liquid region size would result in further growth of the liquid sphere, whereas a small decrease in size would result in shrinkage and disappearance of the liquid pool. This behavior is similar to that of a classical critical nucleus. Spherically symmetric perturbations to the larger melting limit solution would disappear whether applied in either direction, returning back to the original steady state. Therefore the melting limit would act as a stable fixed point in a spherically symmetric

melting process. A liquid sphere larger than the nucleus size would be favored to continue growing until settling upon the melting limit. At the cutoff (α = 1/27 = 0.0370...) the β values of the nucleus and melting limit solutions approach each other as the radii approach each other (seen in Figure 3.3) and the solutions merge becoming identical at the cutoff.

Summing together previous results, we see that the spherically symmetric analysis reveals that the unstable states may be identified as nuclei because these (smaller) liquid pool solutions are continuously connected on a single solution branch, starting from the $\alpha = 0$ case of an isothermal superheated system that represents a classical liquid nucleus, and maintaining the same stability characteristics as α is increased, until, but not including, the cutoff value $\alpha = 1/27$. Therefore, all such unstable states will be denoted as nucleus states even in the systems having non-uniform thermal fields.

3.4.1 Saddle-node bifurcation

For the spherically symmetric case, in addition to the linear stability analysis, we may also perform a time-dependent growth analysis to see how the spherical liquid region evolves as a function of time. The governing equations, given in the "tilde" scaling, are as follows. First, the heat equation in both phases:

$$\frac{1}{\tilde{R}^2}\frac{d}{d\tilde{R}}(\tilde{R}^2\frac{d\tilde{U}(\tilde{R})}{d\tilde{R}}) = -6\alpha \tag{3.55}$$

where the quasi-static approximation is being used. The energy balance at the interface:

$$\tilde{V}_n = \frac{d}{d\tilde{R}}\tilde{U}_S - \frac{d}{d\tilde{R}}\tilde{U}_L \tag{3.56}$$

Denoting the radius of the spherical liquid region as $\tilde{R}^*$, for a given value of $\tilde{R}^*$ the temperature distributions in the liquid and solid phases are:

$$\tilde{U}_L(\tilde{R}) = -\alpha\tilde{R}^2 + (\frac{2}{\tilde{R}^*} + \alpha(\tilde{R}^*)^2) \tag{3.57}$$

$$\tilde{U}_S(\tilde{R}) = -\alpha\tilde{R}^2 - \frac{C}{\tilde{R}} + (\frac{2}{\tilde{R}^*} + \alpha(\tilde{R}^*)^2 + \frac{C}{\tilde{R}^*}) \tag{3.58}$$

$$C \equiv \frac{-\alpha(\tilde{R}^*)^3 + \tilde{R}^* - 2}{1 - \frac{\tilde{R}^*}{\tilde{R}_C}} \tag{3.59}$$

We obtain for the time derivative of the spherical liquid region radius:

$$\tilde{V}_n = \tilde{R}^{*'}(\tilde{\tau}) = \frac{-\alpha(\tilde{R}^*)^3 + \tilde{R}^* - 2}{(\tilde{R}^*)^2 - \frac{(\tilde{R}^*)^3}{\tilde{R}_C}} \tag{3.60}$$

It is noted that in the numerator of the RHS of (3.60) there is the same polynomial encountered earlier whose roots are the steady state nucleus and melting limit radii. The denominator is always positive for $0 < \tilde{R}^* < \tilde{R}_C$. Therefore the nucleus and melting limit are the fixed points in the system of the time evolution of $\tilde{R}^*$.

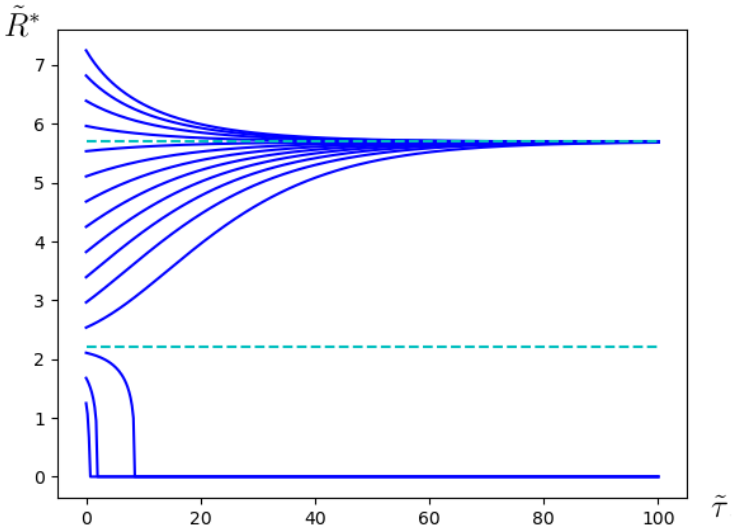

Figure 3.5: Time dependence of spherical liquid region scaled radius $\tilde{R}^*$ as a function of scaled time $\tilde{\tau}$ for $\alpha = 0.020$. Nucleus and melting limit radii are plotted as horizontal dotted lines. For the trajectories which reach zero radius, the remainder of the trajectory is plotted as a constant horizontal line at zero radius corresponding to the physical case in which the liquid has completely re-solidified.

The time evolution of $\tilde{R}^*$ for multiple different initial radii is plotted in Figure 3.5 for the case of $\alpha = 0.020$, integrated using the Python Scipy package function odeint(). The nucleus and melt-

ing limit radii are plotted as horizontal dotted lines. It is seen that initial radii above and below the nucleus radius are repelled away from the nucleus radius. For radii less than the nucleus, the liquid radius shrinks rapidly down to zero, corresponding to the disappearance of the liquid phase. For radii greater than the nucleus, growth proceeds towards the melting limit, approaching it asymptotically. These results are consistent with the findings of the stability analysis, the nucleus being an unstable fixed point and the melting limit being a stable fixed point in the system dynamics.

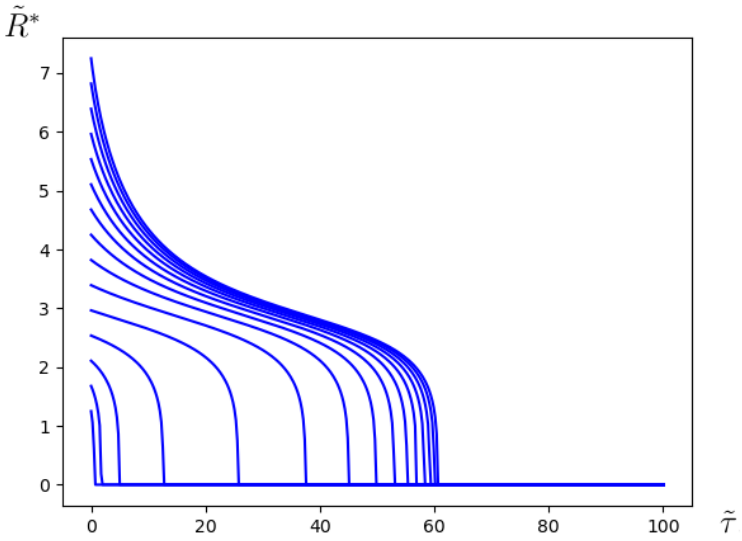

Figure 3.6: Time dependence of spherical liquid region scaled radius $\tilde{R}^*$ as a function of scaled time $\tilde{\tau}$ for $\alpha = 1.2/27$. For the trajectories which reach zero radius, the remainder of the trajectory is plotted as a constant horizontal line at zero radius corresponding to the physical case in which the liquid has completely re-solidified.

Using the same procedure, we may also investigate the behavior of the system in the regime beyond the cutoff, $\alpha > 1/27$. Results for $\alpha = 1.2/27$ are shown in Figure 3.6. It is seen that the time evolution of the liquid radius is uniformly in the negative direction for any starting point. This corresponds with the observation of melting not being favored for α beyond the cutoff.

Combining the results for α less than the cutoff value and α greater than the cutoff value, we see that the system as a whole may be described as a saddle-node bifurcation with respect to the parameter α. In bifurcation theory, a saddle node bifurcation is a type of local bifurcation in a continuous dynamical system in which for a given parameter, two solutions for some values of that

parameter and then at a certain critical parameter value the two solutions approach each other and merge, and there are no solutions beyond that critical parameter value. In a saddle node bifurcation, one of the solution branches is stable, referred to as the ”node”, and the other solution is unstable, referred to as the ”saddle-point”. In the case of the spherical PCM system studied here, the system dynamics are captured by the differential equation (3.60), which is what produces the saddle-node bifurcation. For $\alpha > 1/27$, there are no steady state solutions, and then at $\alpha = 1/27$ there is the sudden appearance of two steady state solution branches. One of these branches is unstable (”saddle point”), and the other is stable (”node”). The two branches merge at exactly $\alpha = 1/27$ which is the saddle-node bifurcation point.

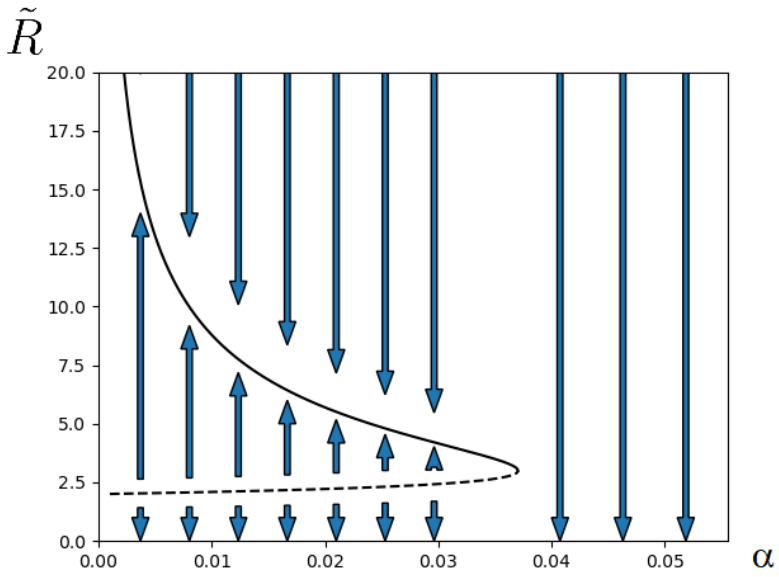

Figure 3.7: Equilibrium radii as a function of α, nucleus radii shown as dotted line and melting limit radii shown as solid line. Arrows indicate direction of dynamical evolution of the melting system. A saddle-node bifurcation occurs at $\alpha = 1/27 = 0.\overline{037}$.

We may plot a bifurcation diagram showing the dynamics of the system (Figure 3.7). Reviewing, this diagram has been generated by numerically integrating equation (3.60) to find the direction of the system dynamics with respect to the parameter α and the liquid radius, shown in Figures 3.5 and 3.6, and then schematically combining the results shown in those two figures. Arrows pointing away from nucleus indicate that it is unstable, arrows pointing towards melting limit indicate it is

stable. For α greater than the saddle-node bifurcation point $1/27$, the dynamics of the system favor completely negative growth (disappearance) of the liquid region. As α decreases below the saddle node bifurcation value, the melting limit and nucleus solution branches appear and a new region begins to develop in between the nucleus and melting limit in which positive growth is favored. At the saddle-node bifurcation point itself, the melting limit and nucleus solutions merge with a radius $\tilde{R} = 3$.

Comparing with the non-spherical device model, the linear stability characteristics of the maximum eigenvalue modes in the non-spherical model correspond to the characteristics seen in the spherical case for both the melting limit and nucleus. Given this comparison, the knowledge that in the spherical model the termination of the nucleus solution branch in the isothermal limit is the classical nucleation theory solution further confirms the direct connection to the classical nucleus in the non-spherical device model. The cutoff of the melting limit and nucleus states at a particular control parameter value also occurs in both models, with respect to voltage in the non-spherical device model and the dimensionless α parameter in the spherical model. In the non-spherical model the cutoff is approached via a decrease in voltage whereas in the spherical model it is approached with an *increasing* value of the parameter α. This is because voltage is the parameter which corresponds with the non-isothermal nature of the system caused by the Joule heating, which is what the α factor also represents, but with a different sign for directional variation of system outcomes. Given that we concluded that the system dynamics in the spherical model feature a saddle-node bifurcation at the cutoff point, we may also observe that the system dynamics in the non-spherical device model likely feature a saddle-node bifurcation as well. For voltages below the cutoff voltage 1.129V, it is likely that the system dynamics mirror the case of the spherically symmetric model for $\alpha > 1/27$, with liquid region evolution in the negative (shrinkage) direction. Then, at the saddle node bifurcation (cutoff point), the nucleus and melting limit branches emerge and positive liquid growth is favored for sizes between the nucleus and melting limit.

At this point it is useful to summarize and compare with the previously mentioned past literature dealing with phase transitions occurring in inhomogeneous driving force backgrounds [52][53]

[54] [55] [56] [57] [58] [59]. One thing that all of these studies have in common is that there is no mention of the equivalent of the melting limit in this research, i.e. the stable state of final evolution of the phase transition system. Instead, they only model a nucleus solution. Additionally, as mentioned previously, these studies all use the assumption of a global thermodynamic potential which is extremized to find the nucleus in the inhomogeneous background. This is in sharp contrast to the analysis performed here, in which results have been present as simply a time-dependent analysis of the dynamics of the systems, with no assumption made about a global thermodynamic potential. This combination of inclusion of the melting limit solution and using a kinetic analysis has allowed the fact of the saddle-node bifurcation emerging at the cutoff to be clarified and examined. It is conceivable that many of those systems studied in the past literature with inhomogeneous driving force backgrounds could have the equivalent of a "melting limit" solution, and that a saddle-node bifurcation would be found with the melting limit-equivalent solution merging with the nucleus solution at the bifurcation point.

3.5 Analysis of cylindrically symmetric PCM Model

In addition to the non-spherical conventional PCM device model and the spherically symmetric model presented above, similar research and analysis has also been performed on a cylindrically symmetric PCM model. This analysis is presented below. The cylindrical model is notable for the way that new phenomena appear in the different symmetry conditions. The nucleus state becomes elongated under certain conditions, leading to the question of whether or not a Rayleigh-type instability occurs in the nucleus state for those conditions. These questions are investigated in the analysis below.

3.5.1 Description of model system and problem

In this model system, a voltage is applied across electrodes at the top and bottom of a GST cylindrical cell, causing a uniform current density of magnitude $J = \sigma_S V/l_c$ to flow lengthwise

through the cell, where σ_S is the electrical conductivity of material S, V is the applied voltage, and l_c is the length of the cell. This current results in uniform Joule heating $\dot{q}_V = J^2/\sigma_S = \sigma_S V^2/l_c^2$ throughout the volume of the cell.

Surrounding the GST cell is a reservoir maintaining a temperature T_0. After the voltage is applied for a sufficient amount of time, the Joule heating will elevate the temperature distribution to some maximum steady state $\frac{\partial T}{\partial t} = 0$ at which point the total Joule heating in the cell is equal to the heat flux outward into the reservoir. Suppose the cell is long enough and the electrode Joule heating small enough that the temperature distribution away from the ends of the cell may be approximated as varying only in the radial direction. This is what is meant by "cylindrically symmetric" in this context. The steady heat equation in cylindrical coordinates (r, z, ϕ) inside the cell then has no z or ϕ derivatives, and has the form:

$$k_S \frac{1}{r}\frac{\partial}{\partial r}(r\frac{\partial T}{\partial r}) + \dot{q}_V = 0 \tag{3.61}$$

Where k_S is the thermal conductivity of the solid phase of GST. Solving (3.61) with the boundary condition $T(r = r_c) = T_0$, where r_c is the radius of the cylinder, gives the steady state temperature distribution (away from the ends of the cylinder):

$$T(r) = T_0 + \frac{\dot{q}_V}{4k_S}(r_c^2 - r^2) \tag{3.62}$$

The above solution shows that the temperature is maximal at the center line $r = 0$, and falls off radially. This can be expressed as:

$$T(r) = T_h - ar^2 \tag{3.63}$$

Where $a \equiv \dot{q}_V/4k_S = \sigma_S V^2/4k_S l_c^2$, and $T_h \equiv T_0 + ar_c^2$ is the maximal, center line temperature.

If T_h exceeds the melting temperature T_m of material M, i.e. $T_h > T_m$, then a driving force for melting is introduced. Suppose that the temperature near the top and bottom of the cell, where the approximation of no z-dependence does not hold, is much lower, due to heat flux outward into

the electrodes. It is natural to hypothesize that the liquid phase would nucleate homogeneously at the center, since superheating is at a maximum there, and not heterogeneously at the electrodes. Then, the Joule heating would drive the liquid region to grow outward radially and vertically, possibly reaching some limiting shape due to the temperature decreasing radially (and vertically at the ends).

3.5.2 Steady states

The state variables are the temperature distribution $T_i(\vec{x})$ throughout each phase and the configuration of the 2D solid-liquid interface. The conditions for steady state are then given by three conditions: steady state temperature distribution in the bulk, steady state interfacial configuration (zero interfacial motion), and local equilibrium at the interface.

The two conditions in the bulk are encapsulated in the the steady state heat equation, satisfied throughout the bulk of both the solid and liquid phases:

$$\nabla^2 T_i = -\frac{\dot{q}_V}{k_i} \tag{3.64}$$

where the subscript i denotes application to both the solid and liquid phases, which are individually specified throughout this analysis with subscripts S for solid and L for liquid, and k_i is the thermal conductivity of each phase. Equation (3.64) ensures steady state temperature in the bulk. The Joule heating term $\dot{q}_V$ appearing in (3.64) is a potentially nonuniform function of space that is solved for using the Laplace equation for the electric potential throughout both phases: $\nabla^2 \phi_i = 0$, $J_i = \sigma_i \nabla \phi_i$, $\dot{q}_V = \frac{J_i^2}{\sigma_i}$, Here, we approximate that the electrical conductivities of the two phases are equal, $\sigma_L = \sigma_S$. Then, the electric potential is not affected by the configuration of the liquid region, and the current density throughout both phases has the same uniform axial value that it does in the previously derived case of a pure solid cell, $J = \sigma_S V / l_c$, resulting in the same uniform Joule heating $\dot{q}_V = J^2/\sigma_S = \sigma_S V^2 / l_c^2$ throughout both phases. This approximation is useful for the purposes of this analysis because it decouples electrical effects from the thermal effects which

are the focus of this analysis.

The condition for a steady state interfacial configuration is simply that there is zero interfacial velocity. This means no latent heat is absorbed/emitted, so energy balance then requires that heat fluxes must balance:

$$k_L \nabla T_L \cdot \hat{n} = k_S \nabla T_S \cdot \hat{n} \tag{3.65}$$

Finally, the condition for local equilibrium at the interface is given by the Gibbs-Thomson condition:

$$T - T_m = T_m \frac{\gamma h}{L} \tag{3.66}$$

Where γ is the solid-liquid interfacial energy, h is the mean curvature of the solid-liquid interface, and L is the latent heat of fusion, i.e. the change in enthalpy per volume from solid to liquid. In the case of the nonuniform temperature system investigated in this analysis, a consequence of (3.66) is that the curvature of a steady-state solid-liquid interface must vary continuously with the temperature variance, introducing the possibility of non-spherical shapes in the cylindrical device.

The equations for the interface conditions (3.65) and (3.66) are simplified with the following dimensionless variable definitions and scalings.

The temperature T is replaced with the dimensionless superheating U:

$$U \equiv \frac{T - T_m}{T_m} \tag{3.67}$$

Using the length scale $x_0 \equiv \gamma / L$, the dimensionless length is:

$$X \equiv \frac{L}{\gamma} x = \frac{x}{x_0} \tag{3.68}$$

The dimensionless mean curvature is then:

$$H \equiv x_0 h \tag{3.69}$$

The dimensionless thermal conductivity is defined in terms of the thermal conductivity of the solid phase, k_S:

$$K \equiv \frac{k}{k_S} \tag{3.70}$$

With these definitions, the zero interface velocity condition (3.65) and the local interfacial equilibrium condition (3.66) have the following dimensionless forms, respectively:

$$K_L \nabla U_L \cdot \hat{n} = \nabla U_S \cdot \hat{n} \tag{3.71}$$

$$U = H \tag{3.72}$$

The steady state heat equation becomes:

$$\nabla^2 U_i = -\frac{\dot{Q}_V}{K_i} \tag{3.73}$$

Where the dimensionless Joule heating is:

$$\dot{Q}_V \equiv \frac{x_0^2}{k_S T_m} \dot{q}_V \tag{3.74}$$

The above equations can be used to solve for steady states, but more analysis is needed to characterize the behavior of a steady state within the melting process, i.e. whether it behaves more like a nucleus state or a melting limit. To answer this question, time-dependent linear stability analysis of the liquid region shape/size is done on steady states to obtain information about stability. Stability with respect to perturbations in the size of the liquid region, i.e. wave number = 0, is characteristic of a melting limit whereas instability is characteristic of a nucleus state. Testing stability under shape perturbations with wave number > 0 can reveal Rayleigh-like or other unknown instabilities of steady state liquid regions unique to nonisothermal cases.

In the next sections, steady states are calculated using the approximation that the thermal conductivities of the solid and liquid phases are equal. While differences in these thermal conductiv-

ities are significant in real systems, this approximation is useful for this analysis because, as with the other approximations used, it allows the effect of non-thermal equilibrium to be made most clear.

It follows that $K_L = 1$ and the zero interface velocity condition (3.71) has the simplified form:

$$\nabla U_L = \nabla U_S \tag{3.75}$$

Due to the simple nature of (3.75), the process of calculating steady states can now be done using a procedure where the temperature distribution is fixed and known, while different liquid region configurations are considered. The first step is to find the initial, pure solid steady state. This is simply the pure solid state with the previously calculated steady state temperature distribution $T(r) = T_h - ar^2$. (The interface conditions (3.71) and (3.72) are automatically satisfied because there is no solid-liquid interface). Now suppose there is some liquid region, but the temperature distributions remains the same in space, just split between the two phases. The simplified zero interfacial velocity condition (3.75) is automatically satisfied for any possible configuration of the liquid region, since the temperature gradient ∇U is continuous everywhere, including the interface. Therefore, the problem of finding a steady state is reduced to the problem of finding a liquid region configuration such that the local interfacial equilibrium condition $U = H$ is satisfied for the temperature distribution $T(\rho) = T_h - ar^2$. There is then a single dimensionless equation for the steady state that must be obeyed at every point on the interface:

$$U_h - AR^2 = H \tag{3.76}$$

where $A \equiv x_0^2 a/T_m = \dot{Q}_V/4$, $R \equiv \rho/x_0$, and $U_h = U_0 + A\rho_c^2$. As written above, the steady states would need to be solved across the space of all possible values of the two parameters, U_h and A for a complete analysis. However, as was the case in the spherically symmetric model, one parameter-dependence can be achieved with a second length scaling by the dimensionless factor

U_h:

$$\tilde{R} \equiv U_h R \tag{3.77}$$

$$\tilde{H} \equiv \frac{H}{U_h} \tag{3.78}$$

$$U_h - \frac{A}{U_h^2}\tilde{R}^2 = U_h \tilde{H} \tag{3.79}$$

$$1 - \frac{A}{U_h^3}\tilde{R}^2 = \tilde{H} \tag{3.80}$$

$$1 - \alpha\tilde{R}^2 = \tilde{H} \tag{3.81}$$

$$\alpha \equiv \frac{A}{U_h^3} \tag{3.82}$$

Where the tilde sign above the variables indicates that the scaling in terms of U_h is in use. In this scaling, analysis is much more compact due to there being only a single parameter α. However, note that the actual size of the steady state solutions is unknown unless the values U_h and A are specified. For a given value of α, an infinite number of combinations of U_h and A are possible, and the steady state solutions in these cases all have the same shape but different size, differing by the scaling factor U_h.

3.5.3 Liquid cylinder steady states

The temperature distribution has radial symmetry, so it is natural to first consider cylindrical liquid regions with some radius $\tilde{R}_L$ as candidates for steady states. These are regions for which the phase is liquid for $\tilde{R} < \tilde{R}_L$ and solid for $\tilde{R} > \tilde{R}_L$. The solid-liquid interface has uniform mean curvature $1/\tilde{R}_L$. The interfacial equilibrium condition (3.81) then becomes a cubic polynomial equation in $\tilde{R}_L$:

$$1 - \alpha\tilde{R}_L^2 = 1/\tilde{R}_L \tag{3.83}$$

$$\alpha\tilde{R}_L^3 - \tilde{R}_L + 1 = 0 \tag{3.84}$$

Real, positive solutions of (3.84) are the radii of liquid cylinder steady states. The discriminant

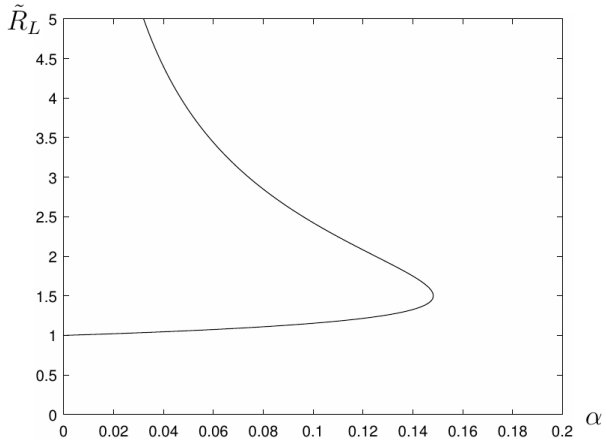

Figure 3.8: Radii $\tilde{R}_L$ of inner (upper portion of the curve) and outer (lower portion) steady state liquid cylinders as a function of α

of the LHS of (3.84) is negative for $\alpha > 4/27$, so positive real solutions for R_L only exist for $0 \leq \alpha \leq 4/27$. In this range, there are two positive real solutions for R_L. The smaller of the two solutions is equal to 1 at $\alpha = 0$ and monotonically increases with α, reaching the value $3/2$ at $\alpha = 4/27$. This solution is referred to as the "inner cylinder" throughout this analysis. The larger of the two solutions approaches infinity as α approaches zero, and decreases monotonically with α, reaching the same value $3/2$ at $\alpha = 4/27$. This solution is referred to as the "outer cylinder". The radii of the inner and outer cylinders as a function of α are plotted in Figure 3.8.

The stabilities of these liquid cylinder steady state solutions are tested by calculating the growth rate of a small axial perturbation:

$$\tilde{F}_L(\tilde{Z}, t) = \tilde{R}_L + \epsilon \tilde{F}_1(\tilde{Z}, t) + O(\epsilon^2) \tag{3.85}$$

where ϵ is a small constant and the 1 subscript stands for first order in ϵ (The zeroth order function is simply $\tilde{F}_0(\tilde{Z}, t) = \tilde{R}_L$). For calculating the perturbed temperature distribution, the quasistatic approximation is used, where the temperature distribution is approximated to relax to steady state on a time scale much faster than the variation of the liquid solid interface. The time-dependent temperature distribution is then given by the steady state heat equation, and its variation is a direct

function of the variation in the solid-liquid interface shape, which alters the boundary condition used in the heat equation. The perturbed temperature distribution is written as:

$$\tilde{U}(\tilde{R},\tilde{Z}) = 1 - \alpha\tilde{R}^2 + \epsilon\tilde{U}_1(\tilde{R},\tilde{Z}) + O(\epsilon^2) \tag{3.86}$$

Expanding the steady state equations gives the linear equations for the first order terms of the perturbed temperature and liquid region shape. The first order steady state heat equation is just the Laplace equation:

$$\nabla^2\tilde{U}_1 = 0 \tag{3.87}$$

With the boundary conditions being the first-order interfacial equilibrium condition at the solid-liquid interface:

$$\tilde{U}_1(\tilde{R}_L,\tilde{Z}) = (2\alpha\tilde{R}_L - \frac{1}{R_L^2})\tilde{F}_1 - \tilde{F}_1'' \tag{3.88}$$

and the first order $T = T_0$ condition at the cell wall radius $\tilde{R}_c$:

$$\tilde{U}_1(\tilde{R}_c,\tilde{Z}) = 0 \tag{3.89}$$

Finally, the non-zero normal velocity appearing in the energy balance of the interface must be considered to analyze the growth rate. To first order, the normal velocity is just the radial outward velocity, and the first order energy balance at the interface becomes:

$$\frac{\partial\tilde{U}_{1L}}{\partial\tilde{R}} - \frac{\partial\tilde{U}_{1S}}{\partial\tilde{R}} = \frac{\partial\tilde{F}_1}{\partial t} \tag{3.90}$$

Because these equation are linear, each perturbation mode $\tilde{F}_1(\tilde{Z}) = e^{\sigma t}e^{i\tilde{K}\tilde{Z}}$ can be tested separately to solve for the unknown growth rate σ.

$$\tilde{F}_L(\tilde{Z}) = \tilde{F}_0(\tilde{Z}) + \epsilon\tilde{F}_1(\tilde{Z}) + O(\epsilon^2) \tag{3.91}$$

$$\tilde{F}_L(\tilde{Z}) = \tilde{R}_L + \epsilon\tilde{F}_1(\tilde{Z}) + O(\epsilon^2) \tag{3.92}$$

$$\tilde{U}(\tilde{R},\tilde{Z}) = \tilde{U}_0(\tilde{R},\tilde{Z}) + \epsilon\tilde{U}_1(\tilde{R},\tilde{Z}) + O(\epsilon^2) \tag{3.93}$$

$$\tilde{U}(\tilde{R},\tilde{Z}) = 1 - \alpha\tilde{R}^2 + \epsilon\tilde{U}_1(\tilde{R},\tilde{Z}) + O(\epsilon^2) \tag{3.94}$$

The normal vector of the solid-liquid interface is:

$$\tilde{G}(\tilde{R},\tilde{Z}) \equiv \tilde{R} - \tilde{F}_L(\tilde{Z}) \tag{3.95}$$

$$\nabla\tilde{G} \equiv < 1, -\epsilon\tilde{F}_1', 0 > \tag{3.96}$$

$$\hat{n} = \frac{\nabla\tilde{G}}{|\nabla\tilde{G}|} = \frac{< 1, -\epsilon\tilde{F}_1', 0 >}{\sqrt{1+\epsilon^2\tilde{F}_1'^2}} \tag{3.97}$$

$$\hat{n} = < 1, -\epsilon\tilde{F}_1'(\tilde{Z}), 0 > \tag{3.98}$$

(The ϵ^2 term is dropped). The mean curvature of the interface is then

$$\tilde{H}(\tilde{Z}) = \nabla\cdot\hat{n} = \frac{1}{\tilde{F}_L} - \epsilon\tilde{F}_1'' \tag{3.99}$$

$$\tilde{H}(\tilde{Z}) = \frac{1}{\tilde{R}_L} - \epsilon(\frac{\tilde{F}_1}{\tilde{R}_L^2} + \tilde{F}_1'') \tag{3.100}$$

The temperature at the interface is:

$$\tilde{U}(\tilde{F}_L(\tilde{Z}),\tilde{Z}) = 1 - \alpha\tilde{F}_L(\tilde{Z})^2 + \epsilon\tilde{U}_1(\tilde{F}_L(\tilde{Z}),\tilde{Z}) \tag{3.101}$$

$$\tilde{U}(\tilde{F}_L(\tilde{Z}),\tilde{Z}) = 1 - \alpha\tilde{R}_L^2 + \epsilon(-2\tilde{R}_L\tilde{F}_1 + \tilde{U}_1(\tilde{R}_L,\tilde{Z})) \tag{3.102}$$

The local interfacial equilibrium equation is then:

$$\tilde{U}(\tilde{F}_L(\tilde{Z}),\tilde{Z}) = \tilde{H}(\tilde{Z}) \tag{3.103}$$

$$1 - \alpha\tilde{R}_L^2 + \epsilon(-2\alpha\tilde{R}_L\tilde{F}_1 + \tilde{U}_1(\tilde{R}_L, \tilde{Z})) = \frac{1}{\tilde{R}_L} - \epsilon(\frac{\tilde{F}_1}{\tilde{R}_L^2} + \tilde{F}_1'') \tag{3.104}$$

The first-order local equilibrium condition is then:

$$-2\alpha\tilde{R}_L\tilde{F}_1 + \tilde{U}_1(\tilde{R}_L, \tilde{Z}) = -\frac{\tilde{F}_1}{\tilde{R}_L^2} - \tilde{F}_1'' \tag{3.105}$$

$$\tilde{U}_1(\tilde{R}_L, \tilde{Z}) = (2\alpha\tilde{R}_L - \frac{1}{R_L^2})\tilde{F}_1 - \tilde{F}_1'' \tag{3.106}$$

As the perturbation evolves, the quasistatic approximation is used that the temperature relaxes to a steady state at each time instant. The expanded steady state heat equation is:

$$\frac{1}{\tilde{R}}\tilde{U}_{\tilde{R}} + \tilde{U}_{\tilde{R}\tilde{R}} + \tilde{U}_{\tilde{Z}\tilde{Z}} = -Q \tag{3.107}$$

$$\frac{1}{\tilde{R}}\tilde{U}_{0\tilde{R}} + \tilde{U}_{0\tilde{R}\tilde{R}} + \tilde{U}_{0\tilde{Z}\tilde{Z}} + \epsilon(\frac{1}{\tilde{R}}\tilde{U}_{1\tilde{R}} + \tilde{U}_{1\tilde{R}\tilde{R}} + \tilde{U}_{1\tilde{Z}\tilde{Z}}) = -Q \tag{3.108}$$

The first order equation is:

$$\frac{1}{\tilde{R}}\tilde{U}_{1\tilde{R}} + \tilde{U}_{1\tilde{R}\tilde{R}} + \tilde{U}_{1\tilde{Z}\tilde{Z}} = 0 \tag{3.109}$$

$$\nabla^2\tilde{U}_1(\tilde{R}, \tilde{Z}) = 0 \tag{3.110}$$

Suppose an axial perturbation has wavelength $\tilde{K}$: $\tilde{F}_1(\tilde{Z}) = e^{\sigma t}e^{i\tilde{K}\tilde{Z}}$. Then the interfacial equilibrium condition becomes:

$$\tilde{U}_1(\tilde{R}_L, \tilde{Z}) = (2\alpha\tilde{R}_L - \frac{1}{\tilde{R}_L^2} + \tilde{K}^2)e^{\sigma t}e^{i\tilde{K}\tilde{Z}} \tag{3.111}$$

$$\tilde{U}_1(\tilde{R}_L, \tilde{Z}) = \hat{\tilde{U}}e^{i\tilde{K}\tilde{Z}} \tag{3.112}$$

The solutions to the Laplace equation in the liquid and solid regions are cylindrical harmonics:

$$\tilde{U}_{1L}(\tilde{R}_L, \tilde{Z}) = (c_0 I_0(\tilde{K}\tilde{R}))\hat{\tilde{U}}e^{i\tilde{K}\tilde{Z}} \tag{3.113}$$

$$\tilde{U}_{1S}(\tilde{R}_L, \tilde{Z}) = (c_1 I_0(\tilde{K}\tilde{R}) + c_2 K_0(\tilde{K}\tilde{R}))\hat{\tilde{U}} e^{i\tilde{K}\tilde{Z}} \tag{3.114}$$

Where I_0 and K_0 are the zeroth modified Bessel functions of the first and second kind, respectively. The liquid region temperature has no K_0 term because that would diverge $\tilde{R} = 0$. The interfacial equilibrium condition applied to the liquid region temperature is:

$$c_0 I_0(\tilde{K}\tilde{R}_L) = 1 \tag{3.115}$$

$$c_0 = \frac{1}{I_0(\tilde{K}\tilde{R}_L)} \tag{3.116}$$

For the solid region, there is the boundary condition at $\tilde{R}_c$ along with the interfacial equilibrium condition:

$$c_1 I_0(\tilde{K}\tilde{R}_c) + c_2 K_0(\tilde{K}\tilde{R}_c) = 0 \tag{3.117}$$

$$c_2 = -c_1 \frac{I_0(\tilde{K}\tilde{R}_c)}{K_0(\tilde{K}\tilde{R}_c)} \tag{3.118}$$

$$c_1 I_0(\tilde{K}\tilde{R}_L) + c_2 K_0(\tilde{K}\tilde{R}_L) = 1 \tag{3.119}$$

$$c_1 = \frac{1}{I_0(\tilde{K}\tilde{R}_L) - I_0(\tilde{K}\tilde{R}_c)\frac{K_0(\tilde{K}\tilde{R}_L)}{K_0(\tilde{K}\tilde{R}_c)}} \tag{3.120}$$

The zeroth order term (base state) of the expanded normal growth velocity $\tilde{V}_n(\tilde{Z}) = \tilde{V}_{n0}(\tilde{Z}) + \epsilon\tilde{V}_{n1}(\tilde{Z})$ is zero. The first order term is:

$$-\tilde{V}_{n1} = \nabla\tilde{U}_{1L} \cdot \hat{n} - \nabla\tilde{U}_{1S} \cdot \hat{n} = (\nabla\tilde{U}_{1L} - \nabla\tilde{U}_{1S}) \cdot \hat{n} \tag{3.121}$$

$$=< \tilde{K}(c_0 I_0'(\tilde{K}\tilde{R}_L) - c_1 I_0'(\tilde{K}\tilde{R}_L) - c_2 K_0'(\tilde{K}\tilde{R}_L))\hat{\tilde{U}} e^{i\tilde{K}\tilde{Z}}, ..., 0 > \cdot < 1, -\epsilon\tilde{F}_1'(\tilde{Z}), 0 > \tag{3.122}$$

$$= \tilde{K}((c_0 - c_1) I_0'(\tilde{K}\tilde{R}_L) - c_2 K_0'(\tilde{K}\tilde{R}_L))\hat{\tilde{U}} e^{i\tilde{K}\tilde{Z}} \tag{3.123}$$

The normal velocity is also related to the perturbation:

$$-\tilde{V_{n1}} = -\tilde{F}_{1t}(\tilde{Z}, \tilde{t}) \tag{3.124}$$

Then, the perturbed temperature distribution $\tilde{U}_1$ is calculated, and the result is plugged into the energy balance equation. The growth rate is found to be:

$$\sigma = \tilde{K}((c_0 - c_1)I_0'(\tilde{K}\tilde{R}_L) - c_2 K_0'(\tilde{K}\tilde{R}_L))(\frac{1}{\tilde{R}_L^2} - 2\alpha\tilde{R}_L - \tilde{K}^2) \tag{3.125}$$

$$c_0 = \frac{1}{I_0(\tilde{K}\tilde{R}_L)} \tag{3.126}$$

$$c_1 = \frac{1}{I_0(\tilde{K}\tilde{R}_L) - I_0(\tilde{K}\tilde{R}_c)\frac{K_0(\tilde{K}\tilde{R}_L)}{K_0(\tilde{K}\tilde{R}_c)}} \tag{3.127}$$

$$c_2 = -c_1\frac{I_0(\tilde{K}\tilde{R}_c)}{K_0(\tilde{K}\tilde{R}_c)} \tag{3.128}$$

To physically exist, a liquid cylinder must satisfy $\tilde{R}_L < \tilde{R}_c$ because the material does not extend beyond $\tilde{R}_c$. Also, for $\tilde{K} > 0$, modified Bessel functions are all positive, with I_0 monotonically increasing and K_0 monotonically decreasing. Therefore, c_0 is positive, c_1 is negative, and I_0' is positive, so the first term is positive. c_2 is positive and K_0' is negative, so the second term is also positive. The condition for stability is then:

$$\tilde{K}^2 \geq \frac{1}{\tilde{R}_L^2} - 2\alpha\tilde{R}_L \tag{3.129}$$

The expression $\frac{1}{\tilde{R}_L^2} - 2\alpha\tilde{R}_L$ is calculated numerically for both the outer and inner cylinder solution branches for $0 < \alpha < 2/27$. It is found that for the outer cylinder solution branch, the expression is always negative, meaning the outer cylinder is stable for $K > 0$. For the inner cylinder, the expression is always positive, meaning that the inner cylinder is unstable for long wavelengths $K < \sqrt{\frac{1}{\tilde{R}_L^2} - 2\alpha\tilde{R}_L}$.

The above analysis is valid for $K > 0$, but must be modified for $K = 0$, because for $K = 0$ the radial dependence of the cylindrical harmonic instead has the form:

$$\tilde{U}_{1L}(\tilde{R}_L, \tilde{Z}) = c_0\hat{\tilde{U}}e^{i\tilde{K}\tilde{Z}} \tag{3.130}$$

$$\tilde{U}_{1S}(\tilde{R}_L, \tilde{Z}) = (c_1 + c_2 \ln(\tilde{R}))\hat{\tilde{U}} e^{i\tilde{K}\tilde{Z}} \tag{3.131}$$

The boundary conditions give:

$$c_0 = 1 \tag{3.132}$$

$$c_1 + c_2 \ln(\tilde{R}_L) = 1 \tag{3.133}$$

$$c_1 + c_2 \ln(\tilde{R}_c) = 0 \tag{3.134}$$

$$c_2 = -\frac{c_1}{\ln(\tilde{R}_c)} \tag{3.135}$$

$$c_1 = \frac{1}{1 - \frac{\ln(\tilde{R}_L)}{\ln(\tilde{R}_c)}} \tag{3.136}$$

$$c_2 = \frac{1}{\ln(\tilde{R}_L) - \ln(\tilde{R}_c)} \tag{3.137}$$

$$-\sigma = \tilde{K}(-c_2 \frac{1}{\tilde{R}})(2\alpha \tilde{R}_L - \frac{1}{\tilde{R}_L^2}) \tag{3.138}$$

It is seen that c_2 is again negative and also the final condition $\tilde{K}^2 \geq \frac{1}{\tilde{R}_L^2} - 2\alpha \tilde{R}_L$ still holds with $\tilde{K} = 0$ because the right hand side is negative for all $\alpha > 0$. Therefore, the outer cylinder is again stable for $K = 0$ and the inner cylinder is unstable.

The outer cylinder is interpreted as the final stable state in which melting is complete. However, this is only for cases in which the outer cylinder has a radius smaller than the cell. Otherwise, complete melting of the cell is the melting limit. Physically, the outer cylinder melting limit is explained as a combination of decreasing temperature with increasing radius, i.e. melting cannot occur beyond the radius at which $T = T_m$, and the negative driving force of the solid-liquid interfacial energy which increases with radius. Also, in the limit of zero Joule heating/uniform temperature, the interpretation of the outer cylinder as the melting limit is consistent with the isothermal model of melting in which the entire cell is melted. As α approaches zero, the outer cylinder radius approaches infinity, so it is always larger than the cell radius no matter how large the cell radius is, and the melting limit is complete melting of the cell.

Unlike the outer cylinder, the inner cylinder is unstable in a similar manner to a critical nucleus state, and can be interpreted as the critical nucleus state if there were the constraint that the liquid region must be cylindrical. However, the inner cylinder is not interpreted as an effective nucleus state, because it is infinitely large and a finite sized nucleus would be much less of a nucleation barrier.

These stability analysis results suggest that the inner and outer liquid cylinder solutions together may be two solution branches in a saddle-node bifurcation, analogous to the case of the spherically symmetric PCM system which had an inner and an outer spherical solution that together formed a saddle-node bifurcation. This is supported by the fact that the inner cylinder is unstable while the outer cylinder is stable. Both solutions disappear at the saddle-node bifurcation point at $\alpha = 4/27$.

It is noted that the top and bottom ends of the PCM cell, where the approximation that the temperature distribution is independent of z no longer holds, have not been included in the above analysis. However, in order to be steady state solutions, the liquid cylinders must have end caps with some shape which satisfies $U = H$. Intuitively, since the temperature distribution is smooth, one would expect rounded ends, giving a "hot dog" shaped steady state. Because the temperature decreases axially near the ends of the cell, the curvature of these rounded ends is less than the curvature of a round-shape steady state solution, i.e. a critical nucleus, in the middle of the cell. Only a cylinder which is wider than the critical nucleus could have end caps with roughly larger radii of curvature, i.e. smaller curvature, than the critical nucleus. Therefore, only the outer cylinder, not the inner cylinder, can have valid end caps. This suggests that the inner cylinder is not a physical steady state and is instead a mathematical artifact of ignoring the finite length of the cell.

3.5.4 Closed liquid region steady states

In this section, finite-sized liquid regions are considered as candidates for steady states. Applying the assumption that steady states have radial symmetry, a finite-sized liquid region candidate for a steady state can be described by a one-dimensional function in spherical coordinates $\tilde{S}, \theta, \phi$

giving the solid-liquid interface:

$$\tilde{S} = \tilde{G}(\theta) \tag{3.139}$$

$$0 \leq \theta \leq \pi/2 \tag{3.140}$$

The complete liquid region boundary is generated by rotating this curve around the z-axis and mirroring it across the xy plane. In order to ensure finite mean curvature at the points of symmetry, e.g. no cusps, the curve must satisfy $\tilde{G}'(0) = 0$ and $\tilde{G}'(\pi/2) = 0$. The expression for the mean curvature is:

$$\tilde{H} = \nabla \cdot \hat{n} = (\tilde{G}^2 + \tilde{G}'^2)^{-1/2}(2 - \frac{\tilde{G}'}{\tilde{G}}\cot(\theta)) + (-\tilde{G}\tilde{G}'' + \tilde{G}'^2)(\tilde{G}^2 + \tilde{G}'^2)^{-3/2} \tag{3.141}$$

The temperature at the interface in spherical coordinates is:

$$\tilde{U} = 1 - \alpha\tilde{R}^2 = 1 - \alpha\tilde{G}^2 sin^2(\theta) \tag{3.142}$$

The local interfacial equilibrium condition is:

$$1 - \alpha\tilde{G}^2 sin^2(\theta) = (\tilde{G}^2 + \tilde{G}'^2)^{-1/2}(2 - \frac{\tilde{G}'}{\tilde{G}}\cot(\theta)) + (-\tilde{G}\tilde{G}'' + \tilde{G}'^2)(\tilde{G}^2 + \tilde{G}'^2)^{-3/2} \tag{3.143}$$

The nonlinear ordinary differential equation (3.143) is solved numerically using a shooting method, with the boundary conditions $\tilde{G}'(0) = 0$ and $\tilde{G}'(\pi/2) = 0$. 10000 nodes are used, spaced evenly between $\theta = 0$ and $\theta = \pi/2$ and the relative error tolerance is 10^{-6}. These values allow accurate results across a certain range of α values, which will explained below. A minor problem with this formulation in spherical coordinates is that the expression $\tilde{G}'\cot(\theta)$ evaluates to the indeterminate $0/0$ at $\theta = 0$. This issue is resolved by using the fact that the limit of this expression as θ approaches zero is $\tilde{G}''(\theta)$, and using that value for the $\theta = 0$ node.

The axisymmetric cross sections of the resulting liquid region shapes, for increasing values of α, are plotted in Figure 3.10 . The cross section of the outer cylinder is also plotted for comparison.

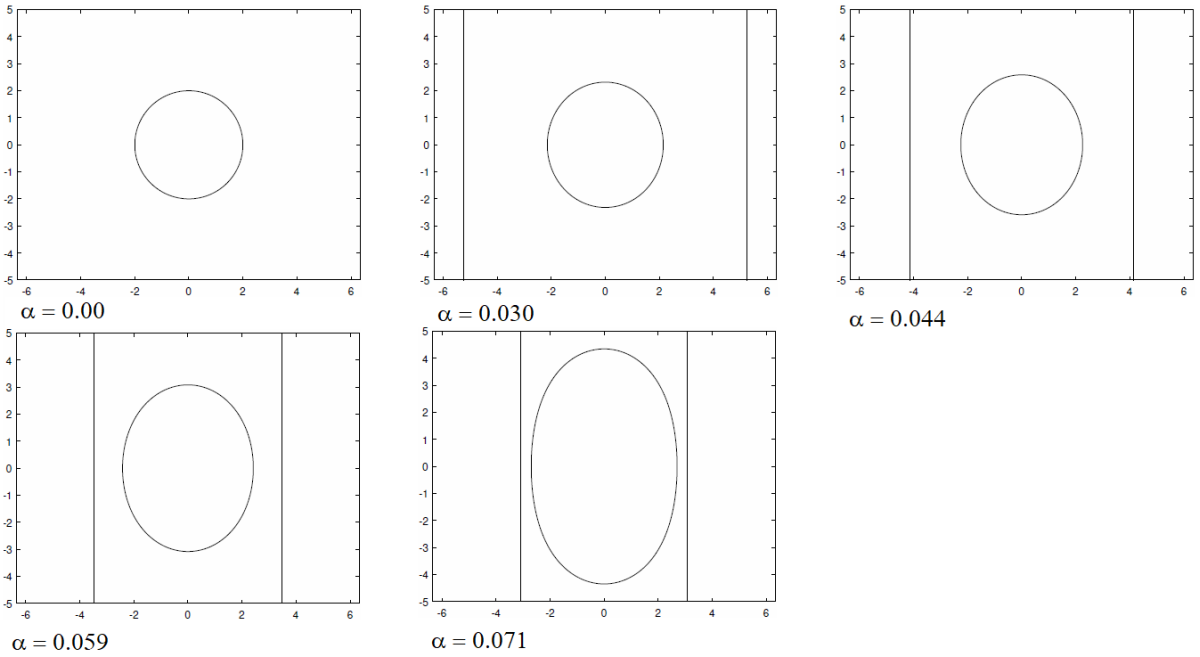

Figure 3.9: Axisymmetric cross sections of steady state finite, closed liquid regions (ellipsoidal shape), along with the outer cylinder (vertical lines), for $\alpha = 0, 0.030, 0.044, 0.059, 0.071$. Horizontal and vertical axes are the scaled, dimensionless $\tilde{R}$ and $\tilde{Z}$ directions, respectively.

For $\alpha = 0$, the uniform temperature case, the solution is the sphere $\tilde{G}(\theta) = 2$. Redimensionalizing, this radius is $\frac{2\gamma}{L}\frac{T_m}{T_0 - T_m}$ which is the critical nucleus radius predicted by classical nucleation theory at temperature T_0. As α increases, the liquid region shape begins to elongate in the $\tilde{Z}$ direction. This is because the condition $\tilde{U} = \tilde{H}$ demands that the mean curvature must be maximum at the poles ($\theta = 0$, $\tilde{R} = 0$) where superheating is greatest, and must decrease with increasing θ and $\tilde{R}$ and reach a a minimum at the equator ($\theta = \pi/2$, $\tilde{R} > 0$) where superheating is lowest. These solutions are interpreted as nucleus states, since they are a smooth continuation of the classical critical nucleus state as α becomes greater than zero.

Starting from $\alpha = 0$, the elongation of the nucleus becomes greater with increasing α, at an accelerating rate. Eventually, a critical value of α is reached beyond which no solutions are found. The numerical value of this critical cut-off is found to a precision of several decimal values by systematically solving (3.143) near the cut off, and incrementing α by decreasing amounts. This method reveals that the critical value is $\alpha = 0.07407 = 2/27$. Examining solutions barely

below $\alpha = 2/27$ shows that degree of elongation rapidly approaches infinity as α approaches $2/27$. The nucleus length approaches infinity, while the nucleus width approaches the finite value 3. Of course, the cell is finite sized and the approximation that the temperature distribution is independent of z would break down with enough length. However, this cut-off value is not an artifact of neglecting the finite size of the cell. In the next section, this cut-off effect is examined and a physical explanation is given.

3.5.5 Melting cut-off

This critical cut-off effect occurring at $\alpha = 2/27$ is distinct from the disappearance of the cylinders at $\alpha = 4/27$, and can in this case be explained in terms of Gibbs free energy. While the definition of steady state used here does not refer to Gibbs free energy or any thermodynamic potential, it happens to be the case that when the thermal conductivities of the two phases are equal, the Gibbs free energy of liquid regions with zero interfacial velocity is extremized by those which satisfy the local interfacial equilibrium condition. Consider a growing region of liquid which grows with the path of least Gibbs free energy. The elongated critical nucleus is the maximum of that path, after which further growth will continue until the liquid region has stretched out to fill the outer liquid cylinder melting limit, which is a minimum in Gibbs free energy. In order for this melting limit to be a minimum that exists beyond the nucleus maximum, the change in Gibbs free energy per unit length of the outer cylinder must be negative as the liquid region continues to increase in length as it fills the outer cylinder. However, as α increases, the Gibbs free energy per unit length of the outer cylinder increases, eventually reaching zero at the critical value $\alpha = 2/27$. This is calculated as follows. First, the total change in Gibbs free energy of the outer cylinder is expressed as the sum of the volume and surface terms (the previous scaling has simplified the expression), and set to zero:

$$\Delta\tilde{G} = \int_0^{\tilde{R_L}} \int_0^{2\pi} (-1 + \alpha\tilde{R}_L^2)\tilde{R}d\phi d\tilde{R} + 2\pi\tilde{R}_L = 0 \tag{3.144}$$

$$\frac{\Delta\tilde{G}}{2\pi} = \int_0^{\tilde{R}_L} (-\tilde{R} + \alpha\tilde{R}_L^3) d\tilde{R} + \tilde{R}_L = 0 \tag{3.145}$$

$$-\frac{\tilde{R}_L^2}{2} + \alpha\frac{\tilde{R}_L^4}{4} + \tilde{R}_L = 0 \tag{3.146}$$

$$-\frac{\tilde{R}_L}{2} + \alpha\frac{\tilde{R}_L^3}{4} + 1 = 0 \tag{3.147}$$

We already know that in order to be a steady state liquid cylinder, $\tilde{R}_L$ is a solution of $\alpha\tilde{R}_L^3 - \tilde{R}_L + 1 = 0$. Subtracting this expression from (3.146) gives:

$$\frac{\tilde{R}_L}{2} - \alpha\frac{3\tilde{R}_L^3}{4} = 0 \tag{3.148}$$

$$2 = 3\alpha R_L^2 \tag{3.149}$$

$$\tilde{R}_L = \sqrt{\frac{2}{3\alpha}} \tag{3.150}$$

Plugging (3.150) into (3.145) gives:

$$\frac{1}{9\alpha} + \sqrt{\frac{2}{3\alpha}} = 0 \tag{3.151}$$

$$\alpha = 2/27 \tag{3.152}$$

$$\tilde{R}_L = 3 \tag{3.153}$$

Not only does the above derivation explain why there is no closed liquid region nucleus state for $\alpha > 2/27$, it also indicates that transitioning from the initial pure solid state to the final melted state is not favored for $\alpha > 2/27$. For $2/27 < \alpha < 4/27$, the change in Gibbs free energy suggests that the outer cylinder state is metastable and the pure solid state is stable. It is easily shown using the above equations that the change in Gibbs Free energy of formation the outer cylinder is negative for $\alpha < 2/27$, but positive for $\alpha > 2/27$. This suggests that the interpretation of the outer cylinder as the "melting limit" may not be valid for $\alpha > 2/27$. Instead, it may be that not only is there no longer a critical nucleus state, but that the entire melting process is simply not favored for

$\alpha > 2/27$. This interpretation makes sense if the assumption is made that the more elongated the nuclei get as they approach $2/27$, the higher the nucleation barrier becomes, and the less likelihood that the final melted state will be reached. At $\alpha = 2/27$, the nucleation energy barrier becomes infinite, so there is "zero" chance of melting. It would then be a natural continuation to assume that there continues to be "zero" chance of melting for $\alpha > 2/27$. The existence of a melting cut off follows naturally from the definition α: it increases with a greater radial temperature fall-off A and increases with lower central superheating U_h, both of which are changes which decrease the total amount of superheating in the cell, which is the driving force for melting. At the critical $\alpha = 2/27$ value, the superheating is low enough that the cost of formation of the interface is too high for melting to be favorable.

It is noted, however, that this analysis above is not perfectly rigorous, because it does not include the effect of fluctuations, and only ideal steady states are being considered for physical interpretation. Therefore, more precise statements about melting probability or nucleation barriers cannot be made here, and the above remarks are only approximate in that sense.

3.5.6 Linear stability analysis of closed liquid region nucleus states

Even without stability analysis, the above results strongly support interpretation of the finite liquid regions as nucleus states. However, linear stability analysis of these states nonetheless provides additional important information, for two main reasons. First, the stability of these states under change in size can be compared to the classical nucleus behavior, which is to be unstable to small increases or decreases in size. Second, for values of α approaching the critical $2/27$, the highly elongated nucleus states have the potential to have a Rayleigh instability appear for perturbations leading to break up of the nucleus into smaller pieces. This instability is present for the inner cylinder, but not the outer cylinder, so it is not immediately obvious whether it occurs for elongated nuclei. Linear stability analysis is needed to resolve this question.

A first order perturbation to the critical nucleus state is written as:

$$\tilde{G}(\theta) = \tilde{G}_0(\theta) + \epsilon\tilde{G}_1(\theta) + O(\epsilon^2) \tag{3.154}$$

Using the quasistatic approximation, the new temperature distribution which satisfies the steady heat equation has the form of the original temperature distribution with an additional perturbation term

$$\tilde{U}(\tilde{S},\theta) = \tilde{U}_0(\tilde{S},\theta) + \epsilon\tilde{U}_1(\tilde{S},\theta) + O(\epsilon^2) \tag{3.155}$$

$$\tilde{U}(\tilde{S},\theta) = 1 - \alpha\tilde{S}^2\sin^2(\theta) + \epsilon\tilde{U}_1(\tilde{S},\theta) + O(\epsilon^2) \tag{3.156}$$

Just the same as in the cylindrical case, the first order steady state heat equation is simply the Laplace equation

$$\nabla^2\tilde{U}_1 = 0 \tag{3.157}$$

With two boundary conditions: The condition $\tilde{U}_1 = 0$ at the cell wall $\tilde{R} = \tilde{R}_c$, and the first order expansion of the local interfacial equilibrium condition. The local interfacial equilibrium condition is expanded:

$$\tilde{U}(\tilde{G}(\theta),\theta) = \tilde{H}(\tilde{G}(\theta)) \tag{3.158}$$

$$\tilde{U}_0(\tilde{G}_0(\theta) + \epsilon\tilde{G}_1(\theta),\theta) + \epsilon\tilde{U}_1(\tilde{G}_0(\theta) + \epsilon\tilde{G}_1(\theta),\theta) = \tilde{H}(\tilde{G}_0(\theta) + \epsilon\tilde{G}_1(\theta)) \tag{3.159}$$

$$1 - \alpha\tilde{G}_0^2 sin^2(\theta) + \epsilon(-2\alpha\tilde{G}_0\tilde{G}_1 sin^2(\theta) + \tilde{U}_1(\tilde{G}_0(\theta),\theta)) = \tilde{H}_0 + \epsilon\tilde{H}_1 \tag{3.160}$$

where the terms in

$$\tilde{H}_0 = (\tilde{G}_0^2 + \tilde{G}_0'^2)^{-1/2}(2 - \frac{\tilde{G}_0'}{\tilde{G}_0}\cot(\theta)) + (-\tilde{G}_0\tilde{G}_0'' + \tilde{G}_0'^2)(\tilde{G}_0^2 + \tilde{G}_0'^2)^{-3/2} \tag{3.161}$$

are expanded to give the expression for $\tilde{H}_1$:

$$(\tilde{G}^2 + \tilde{G}'^2)^{-3/2} = (\tilde{G}_0^2 + \tilde{G}_0'^2)^{-3/2} - \epsilon 3(\tilde{G}_0\tilde{G}_1 + \tilde{G}_0'\tilde{G}_1')(\tilde{G}_0^2 + \tilde{G}_0'^2)^{-5/2} \tag{3.162}$$

$$\tilde{H}_1 = -(\tilde{G}_0\tilde{G}_1 + \tilde{G}'_0\tilde{G}'_1)(\tilde{G}_0^2 + \tilde{G}_0'^2)^{-3/2}(2 - \frac{\tilde{G}'_0}{\tilde{G}_0}\cot(\theta)) \tag{3.163}$$

$$+(\tilde{G}_0^2 + \tilde{G}_0'^2)^{-1/2}(\frac{\tilde{G}'_0\tilde{G}_1}{\tilde{G}_0^2} - \frac{\tilde{G}'_1}{\tilde{G}_0})\cot(\theta) \tag{3.164}$$

$$+(-\tilde{G}_1\tilde{G}''_0 - \tilde{G}_0\tilde{G}''_1 + 2\tilde{G}'_0\tilde{G}'_1)(\tilde{G}_0^2 + \tilde{G}_0'^2)^{-3/2} \tag{3.165}$$

$$-3(-\tilde{G}_0\tilde{G}''_0 + \tilde{G}_0'^2)(\tilde{G}_0\tilde{G}_1 + \tilde{G}'_0\tilde{G}'_1)(\tilde{G}_0^2 + \tilde{G}_0'^2)^{-5/2} \tag{3.166}$$

The first order Dirichlet boundary condition at the interface is then:

$$\tilde{U}_1(\tilde{G}_0(\theta), \theta) = 2\alpha\tilde{G}_0\tilde{G}_1 sin^2(\theta) + \tilde{H}_1 \tag{3.167}$$

In solving the Laplace equation to find the first order perturbed temperature distribution, the interface across which the boundary condition is applied is the zeroth order nucleus surface. Because this surface has an unusual shape, fully solving for the temperature throughout the bulk volume of the liquid phase and throughout the solid phase out to infinity would require a complex numerical scheme. However, only knowledge of the temperature gradient at the solid-liquid interface is required for stability analysis. It is natural in this case to instead to write the Laplace equation in the form a boundary integral equation, and reduce the problem to that of solving for the unknown temperature normal gradients on the solid-liquid interface using a boundary element method.

The boundary integral equations are derived for both the liquid region and surrounding solid region. Only the top half of the nucleus/surrounding solid is used in this analysis, since the bottom half can be obtained by symmetry. The liquid region for which the boundary integral equation is applied, denoted L, is given by the top half of the nucleus. The boundary of this region, denoted ∂L, is given by the combination of 1.The curve $\tilde{S} = \tilde{G}_0(\theta)$ rotated around the z axis by 2π. This is the solid-liquid interface denoted I. 2. The bottom circle at $z = 0$ resulting from cutting the nucleus in half, denoted C. The surrounding solid region is given by all of the solid which lies above $z = 0$. The boundary of this region, denoted ∂S, is given by the combination of the

solid-liquid interface I, and the upper half of the cell wall, denoted W.

The 3D fundamental solution to the Laplace equation is

$$\Phi(\tilde{X},\tilde{Y},\tilde{Z},\tilde{X}_0,\tilde{Y}_0,\tilde{Z}_0) = -\frac{1}{4\pi}\frac{1}{\sqrt{(\tilde{X}-\tilde{X}_0)^2+(\tilde{Y}-\tilde{Y}_0)^2+(\tilde{Z}-\tilde{Z}_0)^2}} \tag{3.168}$$

After converting to spherical coordinates, it is written as $\Phi(\tilde{S},\theta,\phi,\tilde{S}_0,\theta_0,\phi_0)$. For a fundamental solution centered at a point $< \tilde{S}_0 = \tilde{G}_0(\theta_0),\theta_0,\phi_0 >$ on the solid liquid interface, the boundary integral equations become:

$$\frac{1}{2}\tilde{U}_{1I}(\tilde{S}_0,\theta_0) = \int_{\partial L} \tilde{U}_{1L}(\tilde{S},\theta)\frac{\partial}{\partial n}\Phi(\tilde{S},\theta,\phi,\tilde{S}_0,\theta_0,\phi_0) - \frac{\partial}{\partial n}\tilde{U}_{1L}(\tilde{S},\theta)\Phi(\tilde{S},\theta,\phi,\tilde{S}_0,\theta_0,\phi_0) \tag{3.169}$$

$$\frac{1}{2}\tilde{U}_{1I}(\tilde{S}_0,\theta_0) = \int_{\partial S} -\tilde{U}_{1S}(\tilde{S},\theta)\frac{\partial}{\partial n}\Phi(\tilde{S},\theta,\phi,\tilde{S}_0,\theta_0,\phi_0) + \frac{\partial}{\partial n}\tilde{U}_{1S}(\tilde{S},\theta)\Phi(\tilde{S},\theta,\phi,\tilde{S}_0,\theta_0,\phi_0) \tag{3.170}$$

$$\tilde{U}_{1I}(\tilde{S}_0,\theta_0) = \tilde{U}_{1L}(\tilde{S}_0,\theta_0) = \tilde{U}_{1S}(\tilde{S}_0,\theta_0) \tag{3.171}$$

Where the normal derivative direction is defined as outward from the liquid region to the solid region. It is desired to eliminate all surface integrals except for those over the solid-liquid interface I. The approximation is made that the fundamental solutions and perturbed temperature functions approach zero at infinity, so if the cell wall is far enough away from the nucleus the approximation is made that the integral over the cell wall is zero. While there may be cases in which the cell wall is in fact closer, the goal of this analysis is to focus on how the nucleus elongation affects stability. Then, the boundary of the solid region, ∂S, is effectively just I, the interface. However, the bottom circle of the liquid region cannot be eliminated with this approximation, since it is always close. Instead, it is first noted that due to smoothness and symmetry the normal derivative of the perturbed temperature $\frac{\partial}{\partial n}\tilde{U}_1$ on the circle is zero, eliminating one of the two terms in the integral. The other term is eliminated by modifying the fundamental solution such that its normal derivative $\frac{\partial}{\partial n}\Phi$ is zero at $z = 0$. This is done by adding on another fundamental solution term with its source point

mirrored across the $z = 0$ plane (method of images).

$$\Phi^*(\tilde{X}, \tilde{Y}, \tilde{Z}, \tilde{X}_0, \tilde{Y}_0, \tilde{Z}_0) = \Phi(\tilde{X}, \tilde{Y}, \tilde{Z}, \tilde{X}_0, \tilde{Y}_0, \tilde{Z}_0) + \Phi(\tilde{X}, \tilde{Y}, \tilde{Z}, \tilde{X}_0, \tilde{Y}_0, -\tilde{Z}_0) \tag{3.172}$$

The boundary integral equations now become:

$$\frac{1}{2}\tilde{U}_{1I}(\tilde{S}_0, \theta_0) = \int_I \tilde{U}_{1I}(\tilde{G}(\theta), \theta)\frac{\partial}{\partial n}\Phi^*(\tilde{G}(\theta), \theta, \phi, \tilde{S}_0, \theta_0, \phi_0) - \frac{\partial}{\partial n}\tilde{U}_{1L}(\tilde{G}(\theta), \theta)\Phi^*(\tilde{G}(\theta), \theta, \phi, \tilde{S}_0, \theta_0, \phi_0) \tag{3.173}$$

$$\frac{1}{2}\tilde{U}_{1I}(\tilde{S}_0, \theta_0) = \int_I -\tilde{U}_{1I}(\tilde{G}(\theta), \theta)\frac{\partial}{\partial n}\Phi^*(\tilde{G}(\theta), \theta, \phi, \tilde{S}_0, \theta_0, \phi_0) + \frac{\partial}{\partial n}\tilde{U}_{1S}(\tilde{G}(\theta), \theta)\Phi^*(\tilde{G}(\theta), \theta, \phi, \tilde{S}_0, \theta_0, \phi_0) \tag{3.174}$$

Adding them together gives:

$$\tilde{U}_{1I}(\tilde{S}_0, \theta_0) = \int_I v_n(\theta)\Phi^*(\tilde{G}(\theta), \theta, \phi, \tilde{S}_0, \theta_0, \phi_0) \tag{3.175}$$

where

$$v_n(\theta) \equiv \frac{\partial}{\partial n}\tilde{U}_{1S}(\tilde{G}(\theta), \theta) - \frac{\partial}{\partial n}\tilde{U}_{1L}(\tilde{G}(\theta), \theta) \tag{3.176}$$

is a quantity proportional to the normal velocity of the solid-liquid interface, according the energy balance condition. A boundary element method is implemented as follows. The solid-liquid interface curve is divided into n discrete sections, each being a linear function $\tilde{S}^i(\theta)$ in the spherical radial coordinate which interpolates between the numerical values at the nodes. Each section is centered at each node, with the two ends points lying halfway between the adjacent nodes. For the first and last nodes at $\theta = 0$ and $\theta = \pi/2$, the sections are half the size, terminating at the end points. For each section, an equation is generated by placing the source point for the fundamental solution at the center point of that section's curve and taking $\phi = 0$ (a point on the $y = 0$ plane). It is approximated that the value of $\frac{\partial}{\partial n}\tilde{U}_1$ is constant across each section as θ varies slightly (as ϕ varies in each section, these values are exactly constant due to axisymmetry). Then, the value of v_n is also constant across each section. Then, there is a vector of n unknown values v_n^i which must

be solved for with the n equations generated from each placement of the fundamental solution source point. The perturbation $\tilde{G}_1(\theta)$ is represented as a vector of n values g_1. The n values of the interface temperature $\tilde{U}_1(\theta)$ are obtained by applying a discretized matrix form of the linear operator that is the RHS of (3.167). This matrix is here denoted $\tilde{U}_1$. For a section with index i, the discretized boundary integral equation (3.175) then becomes:

$$\tilde{U}_{1ij}g_{1j} = \sum_{j=1,n} v_{nj} \int_{\theta^j_{min}}^{\theta^j_{max}} \int_0^{2\pi} \Phi^*(\tilde{S}^j(\theta), \theta, \phi, \tilde{S}^i_0, \theta^i_0, 0)\tilde{S}^j(\theta)\sin(\theta)\sqrt{(\tilde{S}^j(\theta))^2 + (\tilde{S}^{j'}(\theta))^2}d\phi d\theta \tag{3.177}$$

$$\tilde{U}_{1ij}g_{1j} = \sum_{j=1,n} B_{ij}v_{nj} \tag{3.178}$$

where B is the matrix containing the values of each integration for fundamental source location i and integrated boundary section j. The integrations are performed numerically. For sections where the integrand has a singularity due to the source point lying on the integrated region, the numerical integration still gives the correct result, since the singularities are weak and convergence of the integral exists regardless of the manner in which the limit is taken. The normal velocity is then solved for as:

$$v_{ni} = \sum_{j=1,n}\sum_{k=1,n} (B^{-1})_{ij}\tilde{U}_{1jk}g_{1k} \tag{3.179}$$

$$v_{ni} = \sum_{j=1,n} M_{ij}g_{1j} \tag{3.180}$$

where B^{-1} is the inverse matrix of B and M is the matrix multiplication $B^{-1}U_1$. The normal velocity is related to the time dependence of the perturbation as (taking $\phi = 0$, which is arbitrary since v_n is axisymmetric):

$$v_n = (\frac{\partial}{\partial t}G_1(\theta, t))\frac{\tilde{G}_0(\theta)}{((\tilde{G}_0(\theta))^2 + (\tilde{G}'_0(\theta))^2)^{-1/2}} \tag{3.181}$$

After the inverse of the additional factor in the RHS of (3.181) is factored in the matrix M, the relationship between the growth rate of the perturbation and the perturbation itself can be expressed

directly:

$$\frac{\partial}{\partial t} g_{1i} = \sum_{j=1,n} M_{ij} g_{1j} \tag{3.182}$$

For perturbations which are eigenvectors of M, the growth rate of that perturbation is proportional to the perturbation function by a factor of the eigenvalue σ and will grow exponentially as

$$\tilde{G}_1(\theta, t) = e^{\sigma t} \tilde{G}_1(\theta, 0) \tag{3.183}$$

Therefore, eigenvectors with positive eigenvalues represent unstable modes, and eigenvectors with negative eigenvalues represent stable modes. For the results presented here, 100 nodes are used for computing both the base nucleus shape $\tilde{G}_0(\theta)$ and the perturbation function M.

The eigenvalues and eigenvectors are computed across values of α ranging from 0 to the critical $\alpha = 2/27$. 100 nodes are spaced evenly between $\theta = 0$ and $\theta = \pi/2$ used for the discretization (less than the number used for solving for the nucleus shape, because of the increase in computational complexity). The values of the base nucleus shape g_0 are obtained by interpolating the previously solved nucleus shape values.

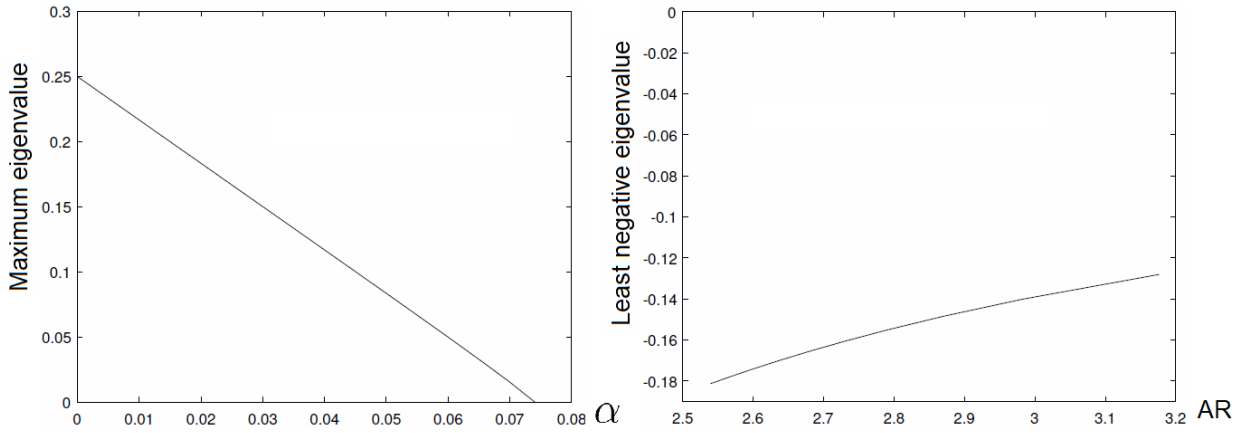

Figure 3.10: (Left) The magnitude of the only positive eigenvalue of M as a function of α. (Right) Least negative eigenvalue of M as a function of nucleus aspect ratio (AR) for highly elongated critical nucleus states.

For $\alpha = 0$, the case of uniform temperature, the expected result is found: There is only one eigenvector with a positive eigenvalue, and that eigenvector is a uniform function, corresponding to

an increase or decrease in the spherical nucleus radius. This matches the expected behavior of the critical nucleus being unstable to changes in size. All other eigenvectors are nonuniform wave-like perturbations, and have negative eigenvalues of magnitude which increases with increasing wave number. These modes are stable because of the resistance to the increase in interfacial surface area, and therefore interfacial energy, caused by the oscillations. For all values of α tested here in the range $0 < \alpha < 2/27$, the eigenvectors and eigenvalues follow a similar pattern to the uniform temperature case, even when the nucleus is highly elongated. There continues to be only one unstable mode, corresponding to further growth or shrinkage of the liquid region. Unlike the uniform temperature case, the unstable mode is greater in magnitude at $\theta = 0$ then at $\theta = \pi/2$, because it is favored for the nucleus to increase its elongation when it grows, or decrease its elongation when it shrinks, rather than have uniform scaling. The magnitude of the unstable eigenvalue approaches zero as α approaches $2/27$, as is shown in Figure 3.10. This is consistent with the fact that the nucleus shape is in a rough sense (although not at the end caps) approaching the outer cylinder, and the outer cylinder is completely stable. The other stable eigenmodes again correspond to oscillations of higher wavenumber. The least negative eigenvalue, the one most likely to correspond to an instability, does not appear to become positive with high aspect ratios. Instead, the magnitude of the eigenvalue gradually approaches zero at a decreasing rate as aspect ratio increases. This trend is shown in Figure 3.10. Also, the second to least negative eigenvalue (not shown) follows the same trend.

The fact that none of these negative eigenvalues become positive at higher aspect ratios shows that there is no evidence from this linear stability analysis of a Rayleigh-like instability of the elongated nuclei. A Rayleigh instability is when a cylindrical region of material is favored to decay into a series of spheres, due to the collection of spheres having lower total surface area than the initial cylinder. When a stability analysis is performed on the cylinder, perturbation modes with wavelengths which correspond to the radius of the spheres are found to be unstable, and it is these modes which drive the process of the initial decay of the cylinder. In the case of the linear stability analysis performed here, despite the fact that some of the eigenvectors have wavelengths

which could correspond to break up of the elongated nucleus into spheres, these eigenvectors have negative eigenvalues and are therefore stable. However, it is noted that a higher order stability analysis could possibly reveal other nonlinear effects not seen here, so the possibility of a Rayleigh-like instability is not fully ruled out. If it is the case that there is no instability, a likely explanation is that these highly elongated nuclei are protected from the Rayleigh instability for the same reason as the outer cylinder: the effect of the nonuniform temperature distribution outweighs the decreases in surface energy that would result from the elongated nucleus breaking into spheres.

Finally, it is noted that it is interesting to compare whether or not the closed liquid region solutions exist as part of a saddle-node bifurcation, as was the case in the spherically symmetric PCM model. Earlier, we noted that the inner and outer liquid cylinder solutions together seem to behave in a manner similar to a saddle-node bifurcation. Is it the case that pairing the closed liquid region solutions with the outer cylinder solution could also be viewed as a saddle-node bifurcation? At the critical value $\alpha = 2/27$, the inner closed liquid region solution elongates and approximately "merges" with the outer cylinder solution class. Additionally, the closed liquid region solution is unstable whereas the outer cylinder solution is stable, another feature in common with a saddle-node bifurcation solution branch pair. However, although the closed liquid region solutions disappear at the critical point $\alpha = 2/27$, the outer liquid region solution does not disappear, instead disappearing at $\alpha = 4/27$. In a true saddle-node bifurcation, both solution branches should merge and then disappear at the same time. Therefore, we can conclude that the closed liquid region solution does not form part of a saddle-node bifurcation.

Chapter 4

Impact of solid-liquid interfacial thermodynamics on RESET scaling

4.1 Comparisons of device scaling behavior

In this chapter, RESET performance is explored as a function of device scale. The models used in this analysis are the complete GT (Gibbs-Thomson) and BM (bulk-melting) models from Chapter 2, each with TBR-absent and TBR-present (thermal boundary resistance included) versions for further comparison. As was the case in Chapter 2, thermoelectric effects and temperature and phase dependent GST thermal and electrical conductivities are included for all model versions in this chapter. For the scaling analysis we scale the device isotropically (equally in all directions). We estimate a condition for a successful RESET step that the quenched amorphous region completely covers the heater. Given that it has been shown in previous chapters that the melting limit liquid region size is the maximum for any given voltage, and its size increases monotonically with increasing voltage, the minimum voltage required for RESET is the minimum voltage at which the melting limit liquid region completely covers the heater. This voltage is computed numerically by iteratively approaching the voltage at which the melting limit covers the heater. The iterative approach is as follows: first, a large voltage is guessed and the melting limit is computed. Then, if the melting limit extends farther than the heater width by at least 0.2 discretized FiPy cell units (described in Chapter 2), the voltage is incremented down by a certain large factor. Then, the melting limit is recomputed. If the melting limit width is less than the heater width, the voltage increment factor is decreased in half and the voltage is incremented downward from the last voltage by the new increment factor. If the melting limit width is between the heater width and the heater width plus 0.2 * the cell spacing, then the iterative procedure is successful and the given voltage is the minimum required RESET voltage. In the GT model, there is additionally the condition that the cutoff voltage is found to be the minimum required RESET voltage if the cutoff melting limit width $\geq$ the heater width. This is using the fact, shown in Chapter 3, that the cutoff voltage in the GT model is the cutoff for melting to occur, so the point at which the cutoff occurs is the minimum voltage at which melting will be favored in the system. The cutoff voltage is computed with a similar iterative procedure, replacing the condition of the melting limit width being greater

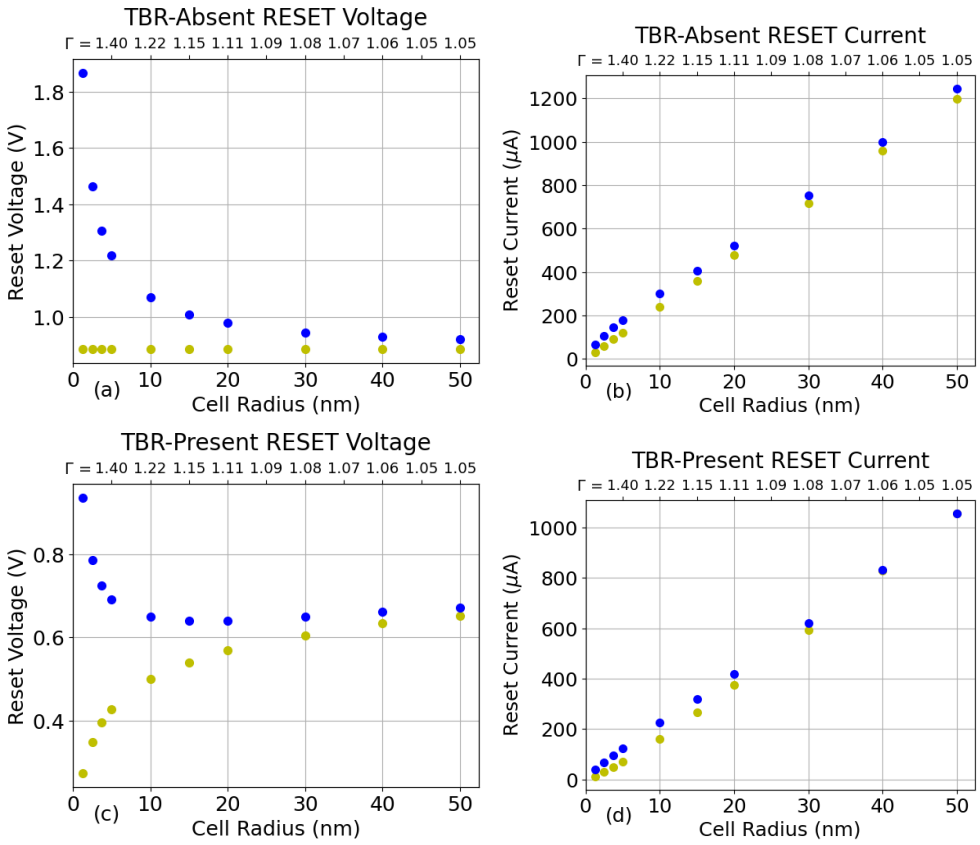

Figure 4.1: Minimum required RESET voltage and corresponding RESET current in TBR-absent and TBR-present cases as a function of device size specified by GST cell radius (CR) (lower x axis) and the dimensionless parameter Γ (defined below) (upper x axis), determined by computing melting limits in the Gibbs-Thomson (GT) model (blue) and in the bulk melting (BM) model (yellow). a. TBR-absent voltage. b. TBR-absent current. c. TBR-present voltage. d. TBR-present current.

than the heater width with the condition of whether or not a melting limit solution is found. As the cutoff voltage is iteratively approached and the voltage increment decreases, the cutoff voltage is found when the voltage increment becomes smaller than 0.003 * the voltage. We also give a RESET current comparison by computing the current present at the minimum voltage state.

The minimum required RESET voltage and corresponding current in the BM and GT models are plotted as functions of GST cell radius (CR) in Figure 4.1, for both the TBR-present and TBR-absent cases. Dimensionless ratios of values in both the GT and BM models to those in the BM model are plotted in Figure 4.2. Minimum RESET voltage in the TBR-absent bulk model is independent of size, a consequence of the lack of length scale present in the model. In the

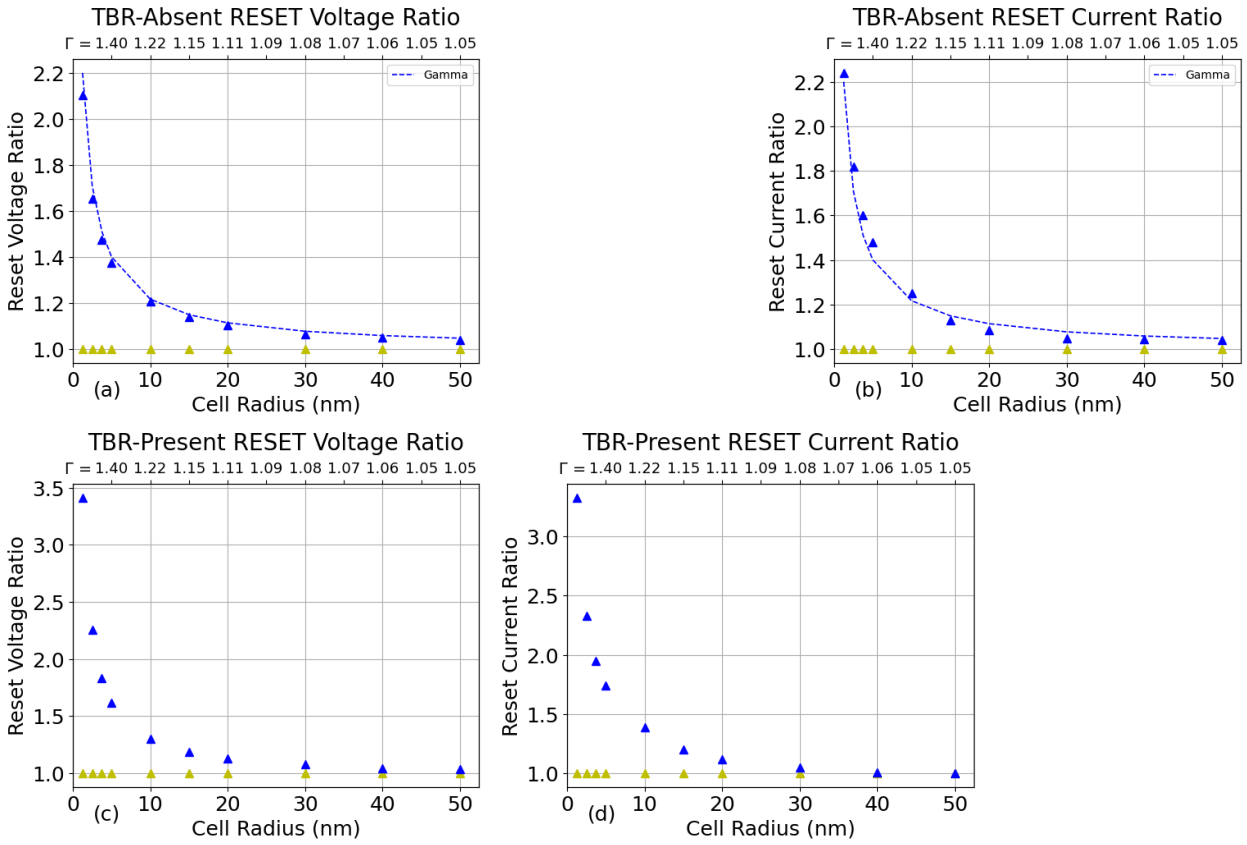

Figure 4.2: Dimensionless ratios of minimum required RESET voltages and corresponding currents of Gibbs-Thomson (GT) (blue) and bulk (BM) (yellow) models to those in the BM model. (BM model ratio values are naturally 1.0). a. TBR-absent voltage. b. TBR-absent current. c. TBR-present voltage. d. TBR-present current.

TBR-absent GT model, minimum required RESET voltage begins to increase significantly (>10%) relative to the BM model as the cell radius decreases below $\approx$ 20 nm. Divergence accelerates with decreasing size and the voltage tends to ∞ as the cell size approaches zero. This result can be understood using geometric analysis. The average radius of the approximately spherical amorphous region needed for RESET is AR (amorphous radius) = 0.40·CR. The Gibbs-Thomson condition becomes: $T \approx T_m(1 + 2(\gamma/L)\text{AR}^{-1}) = T_m(1 + 2\kappa)$ where $\kappa \equiv (\gamma/L)/\text{AR}$, i.e. the ratio of the capillary length scale (γ/L) = 0.96nm to the amorphous radius. For the BM model (and the large scale limit $\kappa = 0$) $T = T_{BM} \equiv T_m$. Volumetric Joule heating density is proportional to V^2, causing temperature in the TBR-absent case to be roughly proportional to V^2, implying $T/T_{BM} \approx V^2/V_{BM}^2$. Combining gives $V^2/V_{BM}^2 \approx 1 + 2\kappa$, $V/V_{BM} \approx (1 + 2\kappa)^{1/2} \equiv \Gamma$. In Figure

4.2 (a), $\Gamma = (1 + 2\kappa)^{1/2}$ is plotted (blue dashed line) in the TBR-absent V/V_{BM} plot and shown to be a close predictor of the ratio. It is seen that the unbounded RESET voltage is a consequence of unbounded κ and Γ.

In Figure 4.1 the TBR-absent BM model RESET current is shown to scale linearly with cell radius, a consequence of the fact that device resistance Σ scales as $\sim$1/CR, while in Figure 4.2 the ratio of GT current to BM current is shown to obey a similar diverging trend as with voltage. Assuming the device electrical resistance Σ is approximately the same between the BM and GT models, inserting V = IΣ into the expression V/V_{BM} gives $V/V_{BM} = I/I_{BM} = \Gamma$. Γ is plotted (blue dashed line) in the TBR-absent I/I_{BM} plot and again shown to be a close predictor of the ratios.

TBR-present results show the added effect of relative reduction of voltage/current increasing with downscaling, seen isolated in the BM TBR-present model. This trend is counteracted in the GT model resulting in increasing voltage required for CR $<=$ 10nm. Dimensionless voltage and current GT/BM ratios are greater in the TBR-present case than the TBR-absent case, so Γ under-predicts for the TBR-present case. This may be due to the geometric impact of TBR on the temperature distribution, as well as $1/T$ temperature dependence of TBR coefficient values. (Other effects not included in the Γ simplification include temperature dependence of bulk properties and thermoelectric effects.)

4.1.1 The limits of superheating

The trends predicted by the Gibbs-Thomson model in this research have used magnitudes of GST temperature that are arbitrarily high, going up to 100% of the bulk melting temperature or higher. However, it was noted in the previously mentioned review of superheating in crystals [24] that there are theoretical temperature limits beyond which the stability of the superheated crystal is expected to become broken. In a paper by Tallon [63] multiple of these ”catastrophic limits” are described in a theoretical model of aluminum. (Figure 4.3) First, raising temperature beyond the point of equal entropies of the liquid and crystal phase would create a ”paradox” in

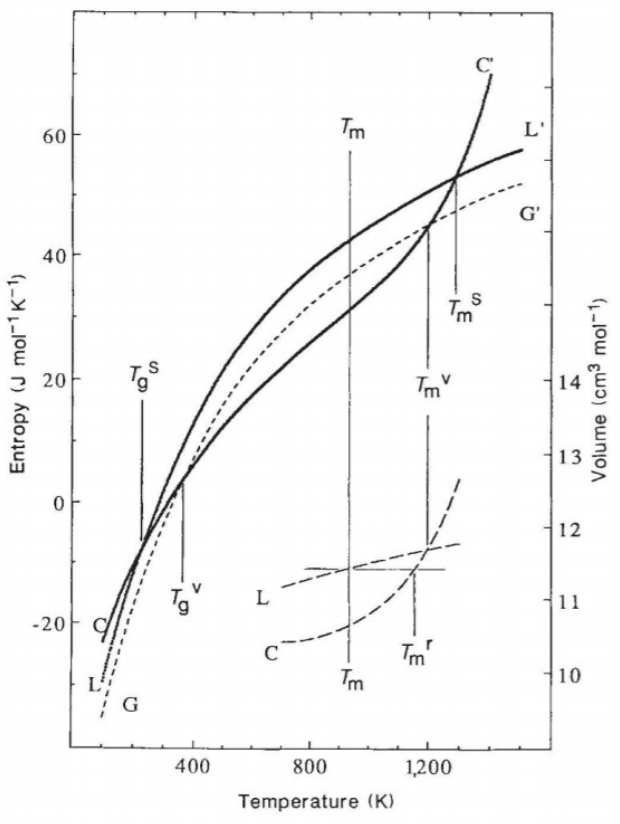

Figure 4.3: Theoretical temperatures of instabilities of crystalline aluminum, taken from [63]. The 'S' superscript refers to the point of equal entropies of the liquid and crystalline phases, the 'V' superscript the point of equal volumes, and the 'r' superscript the point of vanishing shear modulus (rigidity).

which the entropy of the disordered liquid phase is less than the crystalline phase. At a lower temperature, the point of equal volumes of the phases has also been predicted as an instability. And additionally, there is the temperature of vanishing shear modulus of the crystalline phase which causes a mechanical instability. If equivalent limits for the GST crystal are anything similar to this case, then the additional temperature due to the Gibbs-Thomson condition would possibly be limited to around 35% of the bulk melting temperature or lower.

At first glance, this would seem to imply that the Gibbs-Thomson model scaling trends seen in Figure 4.1 would be "cut off" at a certain point once "automatic melting at the catastrophic limits" is factored into the model. However, there are uncertain factors here which require more research. First, time-dependence: how long would these instabilities take to actually initiate, propagate, and

destroy the crystalline order? This is relevant given that the voltage pulses in PCM devices have durations on the scale of nanoseconds, so the melting must occur fast enough to be within that time frame. Also, a solid-liquid interface would nonetheless be present in the inhomogeneous-temperature PCM device even if the central region was melted via these instabilities. What role would it play then, and would a Gibbs-Thomson criterion still apply?

4.2 Impact on device design

For the conventional PCM design, the mathematical trend of linear required current as a function of size predicted by the TBR-absent BM model, and by all models in the large-scale limit, is consistent with existing trends at larger size scales (>20 nm), as described in the reviews of Fong et al.[2] and Kim et. al. [1]. TBR-absent and TBR-present current/voltage GT/BM ratios show a scaling impact due to the GT effect which becomes highly unfavorable at sufficiently small sizes. RESET energy cost (not computed here) is the time-integral of current · voltage. Multiplying current and voltage GT/BM ratios gives 51% and 20% increases in the TBR-absent case and 81% and 26% increases in the TBR-present case at CR = 10nm and CR = 20nm, respectively, showing a substantial potential impact on RESET energy at small scales.

From a design standpoint, GT/BM ratios give the multiplicative impact on performance which could be made from optimizations which reduce or reverse the GT effect. The use of wider heaters to generate regions of nearly one-dimensional temperature profiles and nearly flat solid-liquid interfaces could reduce the relative impact of the GT effect. However, wider heaters are less energy-efficient, which is why conventional designs limit the heater size to a small fraction of the total width of the device. Another potential design would melt the entire GST region during RESET, the final melted state having no solid-liquid interface at all. In ”confined” designs [2] the entire GST is melted, typically with a thin heater the same width as the GST region. However, an interface would still be present during the intermediate melting process. And, this class of design is also less energy efficient when the *entire* GST region is melted. For both of these design classes, ideal-

ized designs would balance the higher energy requirement for the melting of a larger sized liquid pool against the expense of an increased interface curvature and thus higher melting temperature associated with a smaller liquid pool.

Possibly the most effective design for reducing the performance impact due to the GT effect would invert the target configurations of the crystalline and amorphous regions, as is the case in the CNT-electrode design in [11] by Xiong et. al. (shown in Fig. 1 and 2 in [11]), where the RESET state is fully amorphized and the SET state is partially crystallized, resulting in a melting process in which a roughly-cylindrical region of crystal GST is melted from the outside in, and the solid-liquid interface has *negative* curvature. Then the solid-liquid interfacial equilibrium temperature would be *lower* than the bulk melting point. While this type of design has not been simulated here, it is reasonable to guess that this design avoids the negative performance impact, and possibly creates a positive impact by reducing the required RESET current and voltage increasingly as the size scale diminishes.

Chapter 5

Conclusion

A model of phase change memory (PCM) RESET melting in a conventional PCM design is developed in which local interfacial equilibrium is imposed at the solid-liquid GST interface by application of the Gibbs-Thomson equation. The model with the Gibbs-Thomson effect ("GT") is compared to a "bulk" model ("BM") in which the bulk equilibrium melting temperature T_m defines the solid-melt interface and no capillary effects included.

At constant voltage, with the Gibbs-Thomson effect included, two classes of steady state solutions are discovered. The steady states having largest liquid volume are denoted the "melting limit" solutions and represent final liquid regions achieved after the voltage has been turned on and held indefinitely. The steady state solutions having smaller liquid volumes represent a minimum threshold size for the stable co-existence of solid and liquid GST phases and are called the "nucleus" solutions. There is also a critical voltage at which the size of the nucleus liquid region coincides with the size of the melting limit solution. Below this voltage all steady state solutions cease to exist.

A linear stability analysis is performed on the steady state solution branches calculated from the nonlinear model of a PCM device valid during the RESET operation melting process. The analysis is carried out under the assumption that the thermal and the electrical conductivities of the solid and liquid phases are equal and uniform, and ignoring thermoelectric effects and thermal boundary resistance. The analysis shows that the melting limit state is linearly stable under all conditions. The nucleus solution branch is unstable for any set of conditions in which the liquid pool forms. The unstable eigenmode corresponds to the mode that is approximately evenly shaped along the surface of the liquid pool and therefore has relatively less liquid-solid interface area than the other eigenmodes. The least stable (but still stable) eigenmode in the melting limit solution is also the one with the minimum surface area. Other eigenmodes in both solution branches have increasingly more oscillations and hence increasingly more negative eigenvalues reflecting an increasing amount of surface energy effect associated with the perturbation. The unstable eigenfunction represents a liquid region dilated to a size slightly larger or smaller than the nucleus steady state shape and which will then continue to grow larger for a positive signed eigenfunction or shrink for a

negative eigenfunction. Since the numerical results show that the melting limit is the only other steady state solution, the unstable liquid pool will continue to grow until the shape of the liquid pool reaches the melting limit. Thus, the melting limit is a local stable fixed point. On the other hand, the shrinking pool of the nucleus solution branch will continue to shrink until it disappears. In this way the unstable nucleus branch exhibits dynamics entirely similarly to an unstable critical nucleus as given by classical nucleation theory. This conclusion is supported by the fact that in a spherically symmetric approximation model of the PCM device, the termination point of the nucleus solution branch as the system becomes isothermal is the actual classical nucleation solution of a spherical liquid pool in an isothermal superheated solid. A stability analysis is also performed in this spherically symmetric model, showing that the stability characteristics of the nucleus and melting limit states are identical to the numerical device model for the maximum eigenvalue mode. A time-dependent numerical solution of the melting process in the spherically symmetric model is also computed, showing the radius of the liquid region evolving from the nucleus to the melting limit, confirming the dynamical properties implied by the stability analysis. Finally, for the linear stability analysis in both the non-spherical device model and the spherically symmetric model the cutoff voltage is calculated, below which there are no steady state solution branches. At the critical voltage the maximum eigenvalues of the melting solution and the nucleus solution converge to zero and the sizes and shapes of the two solution branches meet at the cutoff point. In the quasi-static regime, we can conclude that the cutoff voltage is a cutoff for melting to occur in the system. The cutoff point is concluded to be an example of a saddle-node bifurcation for both the spherically symmetric model and the non-spherical device model. A similar analysis is also performed on a cylindrically symmetrical PCM model system, showing a nucleus state which becomes increasingly elongated with increasing non-isothermality as the cutoff point is approached. However, the nucleus state does not exhibit a Rayleigh-like instability, likely due to the stabilizing influence of the non-uniform temperature field.

Returning to the realistic device model case, the melting limit solution class is the only steady state exhibited by the BM model. For both BM and GT models, the melting limit solution is used to

compute the minimum required RESET voltage and corresponding current as a function of device size, scaled isotropically. Numerical results show that for the conventional device configuration, the impact of the Gibbs-Thomson effect is to increase minimum voltage and current requirements by an amount that increases significantly as device size decreases, accelerating as device size approaches zero. This behavior is represented by the scaling relation $V_{GT}/V_{BM} \approx (1 + 2\kappa)^{1/2} \equiv \Gamma$, where V_{GT} and V_{BM} are the required RESET voltages (or currents) and κ is the ratio of the capillary length to the required amorphous radius. Both the cases with and without thermal boundary resistance (TBR) have been investigated and it was observed that the ratios of the reset currents and voltages in the two models have similar scaling behaviors.

These results show that the Gibbs-Thomson model has negative consequences for the downscaling of a conventional PCM design. However, a modified design in which the SET state is partially crystallized and surrounded by amorphous GST may result in a lower, rather than higher, interfacial melting point and thus could avoid or even reverse the above trend. As this model correctly includes interfacial conditions existing at a crystal-melt (phase-change) interface, results gained from this approach are a baseline for comparison with future modeling efforts of the time-dependent liquid phase formation that include influences of defects and/or the time-dependent nucleation process.

Bibliography

[1] T. Kim and S. Lee. “Evolution of Phase-Change Memory for the Storage-Class Memory and Beyond”. In: *IEEE Transactions on Electron Devices* 67.4 (2020), pp. 1394–1406.

[2] S.W. Fong, C.M. Neumann, and H.-S.P. Wong. “Phase-change memory-towards a storage-class memory”. English. In: *IEEE Transactions on Electron Devices* 64.11 (2017/11/), pp. 4374 –85.

[3] Stanford R. Ovshinsky. “Reversible Electrical Switching Phenomena in Disordered Structures”. In: *Phys. Rev. Lett.* 21 (20 1968), pp. 1450–1453.

[4] Manuel Le Gallo and Abu Sebastian. “An overview of phase-change memory device physics”. In: *Journal of Physics D: Applied Physics* 53.21 (2020), p. 213002.

[5] T. Tuma et al. “Stochastic phase-change neurons”. English. In: *Nature Nanotechnology* 11.8 (2016/08/), pp. 693 –9.

[6] S.R. Nandakumar et al. “A phase-change memory model for neuromorphic computing”. English. In: *Journal of Applied Physics* 124.15 (2018).

[7] Ning Li et al. “Optimization of Projected Phase Change Memory for Analog In-Memory Computing Inference”. English. In: *Advanced Electronic Materials* 9.6 (2023).

[8] Luchang He et al. “In-memory computing based on phase change memory for high energy efficiency”. English. In: *Science China Information Sciences* 66.10 (2023).

[9] A. Pirovano et al. “Scaling analysis of phase-change memory technology”. In: *IEEE International Electron Devices Meeting 2003*. 2003, pp. 29.6.1–29.6.4.

[10] Jaemin Park et al. “Sb2Te3/TiTe2-Heterostructure-Based Phase Change Memory for Fast Set Speed and Low Reset Energy”. In: *physica status solidi (RRL) – Rapid Research Letters* 17.8 (2023), p. 2200451. eprint: https://onlinelibrary.wiley.com/doi/pdf/10.1002/pssr.202200451.

[11] Feng Xiong, A.D. Liao, and D. Estrada. “Low-power Switching of Phase-change Materials with Carbon Nanotube Electrodes”. English. In: *Science* 331.6029 (2011/04/29), pp. 568 –70.

[12] Panni Wang et al. “Low Power Phase Change Memory with Vertical Carbon Nanotube Electrode”. English. In: *IEEE Journal of the Electron Devices Society* 5.5 (2017), pp. 362 –366.

[13] H. Hayat, K. Kohary, and C.D. Wright. “Can conventional phase-change memory devices be scaled down to single-nanometre dimensions?” English. In: *Nanotechnology* 28.3 (2017/01/20), 035202 (8 pp.) –.

[14] John S. Wettlaufer and M. Grae Worster. “Premelting dynamics”. English. In: *Annual Review of Fluid Mechanics* 38 (2006), pp. 427 –452.

[15] J Wettlaufer and M G. Worster. “Dynamics of premelted films: Frost heave in a capillary”. In: *Physical review. E, Statistical physics, plasmas, fluids, and related interdisciplinary topics* 51 (June 1995), pp. 4679–4689.

[16] Jacob Israelachvili. *Intermolecular and Surface Forces*. English. 2011.

[17] K. Shportko et al. “Resonant bonding in crystalline phase-change materials”. English. In: *Nature Materials* 7.8 (2008/08/), pp. 653 –8.

[18] A. Schlegel et al. “Optical properties of TiN and ZrN”. English. In: *Journal of Physics C (Solid State Physics)* 10.23 (1977/12/14), pp. 4889 –96.

[19] *Matlab file ”fitting.m” from Electromagnetic Template Library*. http://fdtd.kintechlab.com/en/fitting.

[20] Bin Zhang et al. “Vacancy Structures and Melting Behavior in Rock-Salt GeSbTe”. In: 6 (May 2016), p. 25453.

[21] Jinlong Feng et al. “Gold fillings unravel the vacancy role in the phase transition of GeTe”. English. In: *Applied Physics Letters* 112.7 (2018).

[22] Sung-Wook Nam et al. “Electrical wind force-driven and dislocation-templated amorphization in phase-change nanowires”. English. In: *Science* 336.6088 (2012/06/22), pp. 1561 – 6.

[23] J. Scoggin et al. “Modeling heterogeneous melting in phase change memory devices”. English. In: *Applied Physics Letters* 114.4 (2019/01/28), 043502 (5 pp.) –.

[24] Q.S. Mei and K. Lu. “Melting and superheating of crystalline solids: From bulk to nanocrystals”. In: *Progress in Materials Science* 52.8 (2007), pp. 1175 –1262.

[25] Z. Woods et al. “Modeling of phase-change memory: nucleation, growth, and amorphization dynamics during set and reset: Part II - discrete grains”. English. In: *IEEE Transactions on Electron Devices* 64.11 (2017/11/), pp. 4472 –8.

[26] C. Mihai and A. Velea. “Phase change cellular automata modeling of GeTe, GaSb and SnSe stacked chalcogenide films”. English. In: *Modelling and Simulation in Materials Science and Engineering* 26.4 (2018).

[27] P. Ashwin, B.S.V. Patnaik, and C.D. Wright. “Fast simulation of phase-change processes in chalcogenide alloys using a Gillespie-type cellular automata approach”. English. In: *Journal of Applied Physics* 104.8 (2008/10/15), 084901 (8 pp.) –.

[28] Md Tashfiq Bin Kashem et al. “Modeling Reset, Set, and Read Operations in Nanoscale Ge2Sb2Te5 Phase-Change Memory Devices Using Electric Field- and Temperature-Dependent Material Properties”. English. In: *Physica Status Solidi - Rapid Research Letters* 17.8 (2023).

[29] R. Miquel et al. “A Fully Coupled Multi-Physics Model to Simulate Phase Change Memory Operations in Ge-rich Ge2Sb2Te5 Alloys”. English. In: Kobe, Japan, 2023, pp. 317 –320.

[30] Scott W. Fong et al. “Dual-Layer Dielectric Stack for Thermally Isolated Low-Energy Phase-Change Memory”. English. In: *IEEE Transactions on Electron Devices* 64.11 (2017), pp. 4496 –4502.

[31] Panni Wang et al. “Low Power Phase Change Memory with Vertical Carbon Nanotube Electrode”. English. In: *IEEE Journal of the Electron Devices Society* 5.5 (Sept. 2017), pp. 362 –6.

[32] Kun Ren et al. “Carbon layer application in phase change memory to reduce power consumption and atomic migration”. English. In: *Materials Letters* 206 (2017/11/01), pp. 52 –5.

[33] J.H. Park et al. “Scalable CGeSbTe-based phase change memory devices employing U-shaped cells”. English. In: *Thin Solid Films* 634 (2017/07/31), pp. 141 –6.

[34] Liangliang Chen et al. “Programming power reduction in confined phase change memory cells with titanium dioxide clad layer”. English. In: *Applied Physics Letters* 110.2 (2017/01/09), 023103 (5 pp.) –.

[35] A. Pathak and S.K. Pandey. “Electrothermal modeling of Phase change memory with interfacial oxide layer during RESET operation”. English. In: Piscataway, NJ, USA, 2023//, pp. 1 –4.

[36] Amiya Kumar Mishra, Anushmita Pathak, and Shivendra Kumar Pandey. “Electro-thermal analysis of Phase Change Memory Devices for Synaptic Applications”. English. In: Hyderabad, India, 2023, pp. 621 –625.

[37] Azer Faraclas et al. “Modeling of Thermoelectric Effects in Phase Change Memory Cells”. In: *IEEE Transactions on Electron Devices* 61.2 (2014), pp. 372–378.

[38] F. Xiong et al. “Towards ultimate scaling limits of phase-change memory”. English. In: San Francisco, CA, United states, 2016, pp. 4.1.1 –4.1.4.

[39] J.P. Reifenberg, D.L. Kencke, and K.E. Goodson. “The impact of thermal boundary resistance in phase-change memory devices”. English. In: *IEEE Electron Device Letters* 29.10 (2008/10/), pp. 1112 –14.

[40] Suresh Durai, Srinivasan Raj, and Anbarasu Manivannan. “Impact of Thermal Boundary Resistance on the Performance and Scaling of Phase-Change Memory Device”. In: *IEEE Transactions on Computer-Aided Design of Integrated Circuits and Systems* 39.9 (2020), pp. 1834–1840.

[41] Jonathan E. Guyer, Daniel Wheeler, and James A. Warren. “FiPy: Partial Differential Equations with Python”. In: *Computing in Science Engineering* 11.3 (2009), pp. 6–15.

[42] Rie Endo et al. “Electric Resistivity Measurements of Sb2Te3and Ge2Sb2Te5Melts Using Four-Terminal Method”. In: *Japanese Journal of Applied Physics* 49.6 (2010), p. 065802.

[43] Zachary Woods and Ali Gokirmak. “Modeling of Phase-Change Memory: Nucleation, Growth, and Amorphization Dynamics during Set and Reset: Part I-Effective Media Approximation”. English. In: *IEEE Transactions on Electron Devices* 64.11 (2017), pp. 4466 –4471.

[44] Jaeho Lee, Mehdi Asheghi, and Kenneth E Goodson. “Impact of thermoelectric phenomena on phase-change memory performance metrics and scaling”. In: *Nanotechnology* 23.20 (2012), p. 205201.

[45] Ho-Ki Lyeo et al. “Thermal conductivity of phase-change material Ge2Sb2Te5”. In: *Applied Physics Letters* 89.15 (2006), p. 151904. eprint: https://doi.org/10.1063/1.2359354.

[46] John P. Reifenberg et al. “Thermal Boundary Resistance Measurements for Phase-Change Memory Devices”. In: *IEEE Electron Device Letters* 31.1 (2010), pp. 56–58.

[47] J.-L. Battaglia et al. “Thermal characterization of the SiO2-Ge2Sb2Te5 interface from room temperature up to 400°C”. In: *Journal of Applied Physics* 107.4 (2010), p. 044314. eprint: https://doi.org/10.1063/1.3284084.

[48] P. Fiflis et al. “Seebeck coefficient measurements on Li, Sn, Ta, Mo, and W”. In: *Journal of Nuclear Materials* 438.1 (2013), pp. 224–227.

[49] A. Redaelli et al. “Threshold switching and phase transition numerical models for phase change memory simulations”. English. In: *Journal of Applied Physics* 103.11 (2008).

[50] Jie Liu. “Multiscale Simulation of Phase Change Memory”. PhD thesis. Universty of Washington, 2013.

[51] J. Orava and A.L. Greer. “Classical-nucleation-theory analysis of priming in chalcogenide phase-change memory”. English. In: *Acta Materialia* 139 (2017/10/15), pp. 226 –35.

[52] J.J. Hoyt and L.N. Brush. “On the nucleation of an intermediate phase at an interface in the presence of a concentration gradient”. English. In: *Journal of Applied Physics* 78.3 (1995/08/01), pp. 1589 –94.

[53] HangJin Jo et al. “Heterogeneous bubble nucleation on ideally-smooth horizontal heated surface”. English. In: *International Journal of Heat and Mass Transfer* 71 (2014/04/), pp. 149 –57.

[54] Xiaojun Quan, Gang Chen, and Ping Cheng. “A thermodynamic analysis for heterogeneous boiling nucleation on a superheated wall”. English. In: *International Journal of Heat and Mass Transfer* 54.21-22 (2011/10/), pp. 4762 –9.

[55] Di Wu, Yuan-Yuan Duan, and Zhen Yang. “Thermodynamic model for heterogeneous bubble nucleation in a temperature gradient”. English. In: *Applied Physics Letters* 97.8 (2010/08/23), 081911 (2 pp.) –.

[56] Li-Ping Wang et al. “Suppression of ice nucleation in supercooled water under temperature gradients”. In: *Chinese Physics B* 30.6 (2021), p. 068203.

[57] Peng Yi et al. “Predicting the Rate of Homogeneous Intermetallic Nucleation within Steep Composition Gradients”. In: *The Journal of Physical Chemistry C* 124.43 (2020), pp. 23807–23814. eprint: `https://doi.org/10.1021/acs.jpcc.0c08591`.

[58] P. J. Desré and A. R. Yavari. “Suppression of crystal nucleation in amorphous layers with sharp concentration gradients”. In: *Phys. Rev. Lett.* 64 (13 1990), pp. 1533–1536.

[59] Andriy M. Gusak and Fiqiri Hodaj. “Nucleation in a Concentration Gradient”. In: *Nucleation Theory and Applications*. John Wiley & Sons, Ltd, 2005. Chap. 10, pp. 375–417. ISBN: 9783527604791. eprint: https://onlinelibrary.wiley.com/doi/pdf/10.1002/3527604790.ch10.

[60] John W. Cahn and John E. Hilliard. “Free Energy of a Nonuniform System. I. Interfacial Free Energy”. In: *The Journal of Chemical Physics* 28.2 (Aug. 2004), pp. 258–267. eprint: https://pubs.aip.org/aip/jcp/article-pdf/28/2/258/11106115/258_1_online.pdf.

[61] John W. Cahn and John E. Hilliard. “Free Energy of a Nonuniform System. III. Nucleation in a Two-Component Incompressible Fluid”. In: *The Journal of Chemical Physics* 31.3 (Aug. 2004), pp. 688–699. eprint: https://pubs.aip.org/aip/jcp/article-pdf/31/3/688/10945650/688_1_online.pdf.

[62] W. T. Ang. “Boundary Integral Equation for Axisymmetric Potential Problem”. In: 11.3 (2009), pp. 6–15.

[63] J.L. Tallon. “A hierarchy of catastrophes as a succession of stability limits for the crystalline state”. English. In: *Nature* 342.6250 (1989/12/07), pp. 658 –60.